FEDERAL UNIVERSITY OF SANTA CATARINA

DEPARTMENT OF CHEMICAL ENGINEERING AND FOOD ENGINEERING

GRADUATE PROGRAM IN CHEMICAL ENGINEERING

Leticya Lais Coelho

DEVELOPMENT OF PHOTOCATALYTIC CERAMIC MEMBRANES WITH ANTIFOULING PROPERTIES APPLIED TO EFFLUENT TREATMENT

Florianópolis

2022

Leticya Lais Coelho

DEVELOPMENT OF PHOTOCATALYTIC CERAMIC MEMBRANES WITH ANTIFOULING PROPERTIES APPLIED TO EFFLUENT TREATMENT

Thesis subjected to the Graduate Program in Chemical Engineering from the Federal University of Santa Catarina as a requirement to obtain the degree Doctor (Dr.) in Chemical Engineering.

Advisor: Prof. Dr. Regina de Fátima Peralta Muniz Moreira

Co-advisors: Dr. Michaela Wilhelm

Prof. Dr. Dachamir Hotza

Florianópolis

2022

The present work at Doctoral level was evaluated and approved by an examining board composed of the following members:

Prof. Dr. Rosangela Bergamasco
The State University of Maringá

Prof. Dr. Camila Costa de Amorim Amaral
Federal University of Minas Gerais

Prof. Dr. Marco Di Luccio
Federal University of Santa Catarina

Prof. Dr. Agenor De Noni Júnior
Federal University of Santa Catarina

We certify that this is the original and final version of the final work that was considered suitable for obtaining the title of Doctor in Chemical Engineering by the Graduate Program in Chemical Engineering (PósENQ) from the Federal University of Santa Catarina.

_____

Prof. Dr. Débora de Oliveira
Coordinator of PósENQ

_____

Prof. Dr. Regina de Fátima Peralta Muniz Moreira
Advisor

Florianópolis, 2022.

EN: To those who believe in science.

To those who took care of themselves and the most vulnerable during the pandemic.

And especially, to those who do science to directly save lifes or make the world a better place to live.

PT: Àqueles que acreditam na ciência.

Àqueles que se cuidaram por si e pelos mais vulneráveis durante à pandemia.

E principalmente, àqueles que fazem ciência para salvar vidas diretamente ou fazer do mundo um lugar melhor para viver.

ACKNOWLEDGMENTS

RESUMO

O tratamento de águas residuais é uma grande e crescente preocupação ambiental e de saúde. Grande parte dos efluentes produzidos não é tratada ou é tratada por processos convencionais que frequentemente não atingem a eficiência desejada. Os processos de separação por membranas surgiram como uma importante tecnologia para aumentar a eficiência destes tratamentos. Contudo, a incrustação (*fouling*) das membranas é um problema nesses processos. A viabilidade econômica das membranas cerâmicas pode ser aumentada combinando engenharia da morfologia da membrana com propriedades de superfície aprimoradas, resultando em alta permeabilidade e propriedades anti-incrustantes. Assim, este estudo foi dividido em duas etapas principais para este fim. Primeiro, um processo combinado de *tape casting* e inversão de fases foi utilizado para produzir membranas de alumina altamente permeáveis para microfiltração utilizando uma única etapa de sinterização. Caracterização morfológica, mecânica e textural foi realizada. Poros superficiais grandes (0.30–0.42 μm), fluxo de água pura de 52,4 e 26,60 $m^3\ m^{-2}\ h^{-1}$ a 1 bar, e resistência à flexão máxima de 27,60 e 41,11 MPa foram alcançados para membranas produzidas a partir de pastas contendo 45 e 50% (m/m) de alumina, respectivamente. Simulações de permeabilidade realizadas a partir de imagens de microtomografia computadorizada comprovaram que a permeabilidade é influenciada principalmente pela morfologia da camada superior e inferior. Na segunda etapa, a deposição de TiO_2 foi investigada a fim de produzir membranas fotocatalíticas com propriedades anti-incrustantes para tratamento de efluentes. As membranas fotocatalíticas produzidas foram caracterizadas por MEV/EDS, DRX, Raman, além de avaliação de atividade fotocatalítica, filtração e propriedades *antifouling*. *Magnetron sputtering* foi utilizado para produzir membranas fotocatalíticas de TiO_2/Al_2O_3 com camadas de revestimento de 50 a 400 nm. O aumento da espessura do revestimento melhorou a seletividade da membrana durante a filtração da remoção do azul de metileno (MB) e 86% de remoção de MB foi obtida. Sob irradiação ultravioleta, o revestimento foi capaz de restaurar o fluxo de membrana degradando a incrustação formada sobre o filme de 200 e 400 nm. Separadamente, membranas foram funcionalizadas por sol-gel *dip-coating* sem modificar a morfologia da superfície original das membranas. A atividade fotocatalítica foi comprovada através da decomposição do MB em sistema de batelada, enquanto as

propriedades anti-incrustantes foram investigadas usando acetaminofeno como poluente alvo. O processo de filtração fotocatalítica utilizando a membrana com TiO_2 para filtrar o fármaco sob luz UV ($\lambda = $ 365 nm, 10 W) resultou em um aumento de 3,7 vezes no volume do permeado para um mesmo período de filtração em comparação com a membrana de Al_2O_3 sem irradiação. Além disso, a modelagem de incrustação provou uma redução na constante de incrustação, enquanto seus mecanismos não foram modificados. Ambas as técnicas de revestimento foram capazes de produzir revestimento com 100% de fase anatase. Remoção de até 87% de TOC para filtração de efluentes oleosos foi alcançada, porém as capacidades anti-incrustantes para este tipo de efluente não foram observadas devido à incrustação dentro dos poros e à atenuação da luz pela espessa camada de óleo formada na superfície da membrana.

Palavras-chave: Membrana cerâmica fotocatalítica. Microfiltração. TiO_2. Efluente oleoso. *Tape casting*. Inversão de fases.

RESUMO EXPANDIDO

Introdução

A geração de águas residuais, na cidade ou na indústria, está aumentando em quantidade e complexidade. Seu tratamento é uma grande e crescente preocupação ambiental e de saúde. Grande parte dos efluentes produzidos não é tratada ou é tratada por processos convencionais como oxidação química, coagulação e floculação, e tratamentos biológicos muitas vezes falham na remoção eficiente de vários compostos recalcitrantes ou presentes em baixas concetrações. Esses efluentes são produzidos por diversos setores industriais e, se não tratados adequadamente, podem gerar danos substanciais ao meio ambiente. Nesse sentido, há a necessidade do desenvolvimento de tecnologias de tratamento de água e efluentes mais eficientes e econômicas, e várias diretrizes têm sugerido o uso de conceitos de química verde. Neste cenário, a tecnologia de membranas e os processos oxidativos avançados, como a fotocatálise, tem surgido como importantes estratégias para o tratamento de efluentes. Além de sua alta eficiência e a não necessidade de adição de químicos, os processos de separação por membrana têm alta especificidade, ocupam espaço reduzido, tem simplicidade de operação e baixo consumo de energia. Por sua vez, a fotocatálise pode destruir, em condições brandas de operação, substâncias tóxicas e recalcitrantes, mesmo em baixas concentrações.

Os processos de membrana são semelhantes aos processos de filtração convencionais, mas com diâmetros de poros reduzidos, podendo separar de macromoléculas a íons dissolvidos. As propriedades de permeação da membrana são extremamente dependentes de suas características morfológicas, e a seletividade está relacionada à relação entre o tamanho do poro da membrana e o tamanho do composto a ser retido durante a filtração. A técnica de inversão de fases permitiu recentemente a obtenção de membranas cerâmicas assimétrias com uma única etapa térmica. Estas membranas apresentam uma camada superior altamente seletiva e uma camada suporte com alta permeabilidade, o que seria o ideal. Esta técnica pode ser combinada com tape casting para produzir membranas planas. Por outro lado, a incrustação é ainda uma importante limitação do uso de membranas. A incrustação (*fouling*), ou seja, o bloqueio ou estreitamento dos poros pelo material retido, ocorre devido a fatores de adsorção ou deposição de compostos filtrados na superfície da membrana ou no interior dos poros, reduzindo o fluxo do permeado sob pressão transmembrana constante. Portanto, o desempenho da filtração também depende do material da membrana.

O desenvolvimento de membranas cerâmicas é recente, mas este tipo de membrana apresenta características superiores às poliméricas no que diz respeito à seletividade (devido à distribuição de poros estreita e bem definida), permeabilidade, durabilidade e resistência térmica, química e à incrustração. Contudo, seu custo ainda é relativamente elevado. Com isso, estratégias visando aumentar a viabilidade econômica de membranas cerâmicas têm sido buscadas. Entre elas, o uso de membranas fotocatalíticas (PM). PMs com fotocatalisador imobilizado na superfície das membranas podem ser usadas como estratégia antifouling devido à capacidade de degradar incrustantes na superfície da membrana sob irradiação, normalmente UV, e induzir hidrofilicidade pela luz, além de da capacidade de degradar compostos recalcitrantes. Assim, seu uso pode aumentar a eficiência dos processos de filtração, estender o tempo de operação do processo, ou

mesmo reduzir a necessidade do uso de químicos para limpezas, aumento o tempo de vida útil da membrana e sua viabilidade econômica.

Neste trabalho, foram desenvolvidas membranas cerâmicas de alumina pelo método de inversão de fases combinado com *tape casting*. O efeito da composição da suspensão cerâmica, tempo de agitação, condições de colagem e temperatura de calcinação nas propriedades mecânicas e morfológicas das membranas foi estudado. Membranas selecionadas foram recobertas com TiO$_2$ utilizando *magnetron sputtering* ou sol-gel dip coating como técnicas de deposição para produzir membranas fotocatalíticas aplicadas ao tratamento de efluentes. As propriedades morfológicas, mecânicas, química e fotocatalítcas das membranas foram estudadas, além do desempenho na filtração de efluentes oleosos, acetaminofeno e azul de metileno.

Objetivos

Este trabalho teve por objetivo desenvolver membranas cerâmicas fotocatalíticas com estruturas adequadas para microfiltração, elevada permeabilidade e propriedade *antifouling* para posterior aplicação em tratamento de efluentes.

Metodologia

Este trabalho foi dividido em três partes. Primeiramente, membranas de alumina foram produzidas usando com *tape casting* como método de conformação, combinado com inversão de fase seguida de calcinação como método de formação de poros. Para isso, além de alumina, N-metilpirrolidona, polietilenoglicol e polietersulfona foram utilizados na formulação de diferentes suspensões cerâmicas. As membranas de alumina foram calcinadas a 1400 ou 1500 °C após a etapa de solidificação por inversão de fase. Esta técnica resulta em membranas assimétricas com alta porosidade. Contudo, camadas densas indesejadas podem ser formadas na superfície inferior da membrana. Para evitar que isto aconteça, uma estratégia de co-casting com uma suspensão de grafite na parte inferior da suspensão de alumina foi testada, onde o grafite serve de agente de sacrifício para produzir membranas sem a camada densa inferior, aumentando a permeabilidade da mesmo. A caracterização morfológica, mecânica e textural foi realizada por microscopia eletrônica de varredura (MEV), medição de resistência à flexão, porosimetria de mercúrio e microtomografia computadorizada de raios X, além de permeação de água. Na segunda e terceira parte, membranas foram selecionadas para funcionalização com TiO$_2$ por *magnetron sputtering* ou sol-gel *dip-coating*.

Para as membranas produzidas por *magnetron sputtering*, camadas de TiO$_2$ com 50, 200 ou 400 nm de espessura foram adicionadas. As membranas foram caracterizadas por espectroscopia Raman, difração de raios-X (DRX), microscopia eletrônica de varredura (MEV), espectroscopia de raios-X (EDS), atividade fotocatalítica por degradação de azul de metileno em batelada, filtração de MB e emulsão oleosa de óleo de soja. As propriedades fotocatalíticas foram avaliadas para recuperação do fluxo da membrana sob UV ($\lambda = 365$ nm LED, 3W).

Isopropanol, acetil acetona, butóxido de titânio (IV) e ácido acético foram utilizados para produzir a solução-sol gel usada para o processo de sol-gel *dip-coating*. As membranas foram calcinadas a 550 °C com uma taxa de aquecimento de 2 °C min^{-1}. O processo foi realizado 1, 2 ou 3 vezes para produzir membranas com 1, 2 ou 3 camadas de TiO$_2$. O efeito do número de camadas foi avaliado. O resíduo seco do sol-gel foi caracterizado por análise termogravimétrica e DRX. As membranas foram caracterizadas por MEV e

espectroscopia Raman, além de filtração de emulsões de óleo lubrificante e acetaminofeno. A atividade fotocatalítica foi demonstrada pela degradação de azul de metileno em batelada. O efeito antifouling foi investigado pela filtração de acetaminofeno sob luz UV (365nm, 10 W). Além disso, os mecanismos de *fouling* foram investigados por modelagem matemática utilizando-se os modelos de Hermia.

Resultados e Discussão

As membranas produzidas a partir de uma suspensão contendo 45/7 e 50/6,2 alumina/PES% em massa foram consideradas como apresentando o melhor conjunto de propriedades em termos de resistência à flexão e permeabilidade. Poros superficiais grandes (0,30–0,42 μm), fluxo de água pura de 52,4 e 26,60 m^3 m^{-2} h^{-1} a 1 bar, e resistência à flexão máxima de 27,60 e 41,11 MPa foram alcançados para membranas produzidas a partir de pastas contendo 45 e 50% de alumina em massa, respectivamente. Maiores cargas de alumina levaram a uma maior resistência à flexão e menor fluxo à medida que a morfologia da membrana foi modificada. Os tamanhos dos poros da superfície não foram modificados pela composição da suspensão. A estratégia de *co-casting* usando pasta de grafite permitiu que as membranas fossem produzidas sem as camadas densas na parte inferior, embora ajustes adicionais no procedimento de *co-casting* da pasta precisem ser investigados. Simulações de permeabilidade realizadas a partir de imagens de microtomografia computadorizada comprovaram que a permeabilidade é influenciada principalmente pela morfologia da camada superior e inferior.

A modificação da espessura do revestimento de TiO_2 por *magnetron sputtering* melhorou a seletividade da membrana durante a filtração da remoção do azul de metileno (MB) e 86% de remoção de MB foi obtida. A atividade fotocatalítica sofreu pouca influência da espessura do filme entre 50 e 400 nm, e sob irradiação ultravioleta, o revestimento foi capaz de restaurar o fluxo de membrana degradando a incrustação formada sobre o filme de 200 e 400 nm. A deposição resultou em filmes densos (200 e 400 nm) e o tamanho médio de poro foi reduzido a 0,13-0,11 μm para estas membranas, aumentando a seletividade e provendo caráter autolimpante, embora reduzindo o fluxo.

Por sua vez, as PM produzidas por sol-gel *dip-coating* não modificaram a morfologia da superfície original das membranas. A atividade fotocatalítica foi comprovada pela decomposição do azul de metileno em sistema de batelada, enquanto as propriedades anti-incrustantes foram investigadas usando acetaminofeno como poluente alvo. O processo de filtração fotocatalítica utilizando a membrana de TiO_2 para filtrar o fármaco sob luz UV (λ = 365 nm, 10 W) resultou em um aumento de 3,7 vezes no volume do permeado para um mesmo período de filtração em comparação com a membrana de Al_2O_3 sem irradiação. Além disso, a modelagem de incrustação provou uma redução na constante de incrustação, enquanto os mecanismos de incrustação não foram modificados. Ambas as técnicas de revestimento foram capazes de produzir revestimento com 100% de fase anatase. Remoção de até 87% de carbono orgânico total (TOC) para filtração de efluentes oleosos foram alcançadas, porém as capacidades anti-incrustantes para este tipo de efluente não foram observadas devido à incrustação dentro dos poros e à atenuação da luz pela espessa camada de óleo formada na superfície da membrana.

Considerações finais

Membranas cerâmicas fotocatalíticas com capacidade anti-incrustante foram produzidas e caracterizadas. A técnica de *tape casting* combinada com inversão de fases foi usada com sucesso para produzir membranas de microfiltração assimétricas de alumina com alevada permeabilidade e parece ser uma rota alternativa promissora para produzir membranas cerâmicas assimétricas com uma única etapa de sinterização. Ambas as técnicas de revestimento resultaram na deposição de TiO_2 na forma anatase com atividade fotocatalítica. Densas camadas de TiO_2 formadas por *magnetron sputtering* na superfície da membrana levaram a uma alta diminuição do tamanho de poros. Pela curva de calibração utilizada para deposição de TiO_2, a seletividade da membrana poderia ser ajustada pela espessura do filme adicionado. Por sua vez, o dip-coating sol-gel investigado neste trabalho resultou na deposição de TiO_2 na superfície da membrana sem formar uma nova camada separada ou modificar a morfologia da superfície da membrana significativamente. Isso pode ser benéfico para aumentar a eficência de membranas que possuam tamanho de poros adequados. Com aplicações diferentes, ambas as membranas resultaram em capacidades anti-incrustantes. As membranas revestidas com camadas de TiO_2 de 400 nm com pulverização de magnetron foram capazes de remover até 86% de MB e recuperar totalmente seu fluxo após irradiação UV. Para membanas funcionalizadas por sol-gel, um aumento de volume de permeado de 3,7 vezes foi observado durante a permeação de acetaminofeno sob UV em comparação com a membrana original na ausencia de luz. A modelagem de incrustação provou que a constante de bloqueio diminuiu, enquanto os mecanismos de incrustação não foram modificados. As membranas fotocatalíticas produzidas não foram capazes de fornecer desempenho anti-incrustante para filtração efluentes oleosos, devido à deposição de óleo no interior dos poros e da desativação do catalisador pela espessa camada de óleo formada na superfície da membrana. Assim, mais pesquisas são necessárias para produzir uma membrana fotocatalítica com melhor desempenho para este tipo de efluente.

Palavras-chave: Membrana cerâmica fotocatalítica. Microfiltração. TiO_2. Efluente oleoso. Tape casting. Inversão de fases.

ABSTRACT

The treatment of wastewater is a major and growing environmental and health concern. Much of the produced effluent is not treated or is treated using conventional processes that frequently fail to achieve the desired efficiency. Membrane separation processes have emerged as an important technology to treat wastewater. However, fouling is a significant issue in the membrane process, clocking membrane pores and reducing membrane performance. Ceramic membranes' economic viability could be increased by combining membrane morphology engineering with improved surface properties, resulting in high permeability and antifouling properties. This study was divided into two main objectives for this purpose. First, the goal of this research was to combine tape casting and phase inversion techniques to create highly permeable alumina membranes suitable for microfiltration in a single sintering step. Morphological, mechanical, and textural characterization was carried out. Ceramic membranes with large pore sizes of the skin layer (0.30–0.42 μm) were produced. Pure water flux of 52.4 and 26.60 m^3 m^{-2} h^{-1} at 1 bar, and 27.60 and 41.11 MPa maximum flexural strength were achieved for membranes produced from slurries containing 45 and 50 wt% alumina, respectively. Simulations of permeability carried out from X-ray micro-computed tomography images in three axes proved that permeability is mainly influenced by the top skin and bottom layer morphology, which is in agreement with the experimental results. Secondly, membrane surface functionalization with TiO_2 was investigated to produce photocatalytic membranes with antifouling properties for effluent treatment. SEM, TG/DTA, XRD, Raman, photocatalytic activity, and filtration experiments were performed. Magnetron sputtering was used to produce photocatalytic TiO_2/Al_2O_3 membranes with coating layers from 50 to 400 nm. Dense films were produced and coating thickness modification improved membrane selectivity during filtration of MB removal. Under ultraviolet irradiation, the coating was able to restore membrane flux by degrading the fouling formed by MB, with selectivity reaching up to 86% of MB removal for the thickest TiO_2 thin film. In turn, sol-gel dip-coating was used to produce photocatalytic membranes without modifying the original surface morphology of the Al_2O_3 membranes. The photocatalytic activity was proved through methylene blue decomposition in a batch system, while photocatalytic antifouling properties were investigated using acetaminophen as the target pollutant. The photocatalytic filtration process using the TiO_2

membrane to filtrate the drug under UV light ($\lambda = 365$ nm LED, 10W) resulted in a 3.7-fold increase in permeate volume for the same filtration period compared to the bare membrane without irradiation. Furthermore, fouling modeling proved a reduction in fouling constant, while fouling mechanisms were not modified. Both coating techniques were able to produce a coating with a 100% anatase phase. Although membranes were capable of removing up to 87% TOC for oily wastewater filtration, antifouling capabilities for this type of effluent were not observed for the photocatalytic membranes mainly due to fouling inside the pores and light attenuation due to the thick fouling layer on the membrane surface.

LIST OF FIGURES

LIST OF TABLES

LIST OF ABBREVIATIONS

ads	Adsorbed
APS	Average Pore Size
BOD	Biological Oxygen Demand
CA	Cellulose Acetate
CB	Conduction Band
CF	Cross-Flow
CFV	Cross-Flow Velocity
COD	Chemical Oxygen Demand
CTAB	Cetyltrimethylammonium bromide
DI	Deionized
DTA	Differential Thermal Analysis
EDS	Energy-Dispersive X-ray Spectroscopy
EU	European Union
F127	Poly(ethyleneglycol)$_{106}$-block-poly(propyleneglycol)$_{70}$-block-poly(ethyleneglycol)$_{106}$
FDR	Flux Decline Ratio
FOG	Fat Oil and Grease
FRR	Flux Recovery Ratio
GC-MS	Gas Chromatography – Mass Spectroscopy
GCN	Graphitic Carbon Nitride
GO	Graphene Oxide
HF	Hollow Fiber
HFP	Hexafluoropropylene
LSM	Lanthanum-Strontium Manganite
MAH	Monoaromatic Hydrocarbons
MB	Methylene Blue
MCE	Methylcellulose Ester
MCU	Melamine-Cyanuric Acid-Urea
MF	MicroFiltration
MO	Methyl Orange
MPS	Mean Pore Size
MS	Magnetron Sputtering
MSP	Membrane Separation Processes
MW	Molecular Weight
NF	Nanofiber
NMP	N-methyl-2-pyrrolidone
ns	Nano Sheet
P123	Poly(ethyleneglycol)$_{20}$-block-poly(propylene–glycol)$_{68}$-block-poly(ethylene glycol)$_{20}$
PAN	Polyacrylonitrile

PDA	Polydopamine
PEG	Polyethyleneglycol
PEI	Polyetherimide
PES	Polyethersulfone
PM	Photocatalytic Membrane
PMR	Photocatalytic Membrane Reactor
PNIPA	Poly-N-isopropolyacrylamide
POME	Palm Oil Mill Effluent
PR	Photocatalytic Reactor
PVC	Polyvinyl chloride
PVDF	Polyvinylidene fluoride
PVP	Polyvinylpyrrolidone
PW	Produced Water
RGO	Reduced Graphene Oxide
RhB	Rhodamine B
RO	Reverse Osmosis
SDS	Sodium Dodecyl Sulfate
SEM	Scanning Electronic Microscopy
SG	Sol-Gel
SPAN	Stabilized Polyacrylonitrile
TCDD	2,3,7,8-Tetrachlorodibenzodioxin
TGA	ThermoGravimetric analysis
TMP	TransMembrane Pressure
TOC	Total Organic Carbon
TSS	Total Suspended Solids
TTIP	Titanium Tetraisopropoxide
UF	UltraFiltration
UV	UltraViolet
UVA	UltraViolet-A
VB	Valence Band
Vis	Visible
W/O	Water in Oil
XRD	X-Ray Diffractometry
YSZ	Yttria-Stabilized Zirconia
ZIF	Zeolitic Imidazolate Framework
ZSM	Zeolite ZSM-5

LIST OF SYMBOLS

Symbol	Meaning
A	Geometric surface area
c	Speed of light in vacuum (2.998×10^8 m·s^{-1})
C_0	Initial concentration
C_p	Concentration in the permeate
D_{pore}	Pore diameter
e^-	Electron
EG	Band-gap energy
h^+	Positive hole
hv	Light energy
J	Flux
J_0	Initial flux
J_f	Water flux for fouled membrane
J_{w1}	Initial water flux
J_{w2}	Water flux after membrane cleaning
K	Hermia's plugging constant
k_{app}	Apparent rate constant
n	Hermia's mechanism index
R	Rejection coefficient
R_c	Flux resistance due to cake
R_f	Flux resistance due to fouling
R_{irr}	Flux resistance due to irreversible fouling
R_m	Intrinsic membrane resistance
R_p	Flux resistance due to fouling inside the pores
R_r	Reversible fouling resistance
R_t	Total flux resistance
t	Time
V	Permeate volume
γ	Interfacial tension
ΔP	Transmembrane pressure

ΔP_c	Critical pressure
θ	Contact angle
λ	Planck's constant (6.626×10^{-34} J·s)
μ	Fluid viscosity
Φ	Radiant flux

SUMMARY

1 INTRODUCTION AND OBJECTIVES

1.1   INTRODUCTION

Wastewater generation, in the city or industry, is increasing in quantity and complexity. At the same time, conventional water and wastewater treatment techniques, such as chemical oxidation, coagulation and flocculation, and biological treatments often fail in the efficient removal of various compounds by being recalcitrant or being present in low quantities. These methods also have the disadvantage of producing large quantities of sludge and having complex operations. If not properly treated, produced effluents can generate substantial damages to the environment. In this view, there is a need for the development of more efficient and economic water and wastewater treatment technologies. Thus, various directives have suggested using green chemistry concepts. This is the scenario where membrane technology and advanced oxidative process, such as photocatalysis, take place. They already show more efficiency when compared to conventional techniques. In addition to its high efficiency and non-chemical requirements, membrane separation processes have high specificity, a small footprint, simplicity of operation, and have low energy consumption. In turn, photocatalysis can destroy, under mild conditions, toxic and recalcitrant substances, even at low concentrations.

Membrane processes are similar to conventional filtration processes, but the filtration surface has reduced pore diameter, which can separate from macromolecules to dissolved ions. Ultra- and microfiltration are membrane separation processes applicable to removal of compiunds suchs as protein, bacterias, emulsified oil, some dyes and pharmaceutical compounds from effluents. These processes use membranes with a pore diameter between 1 nm and 5 μm. The driving force in these cases is a pressure gradient. The membrane permeation properties are extremely dependent on their morphological characteristics since the selectivity is related to the pore size of the membrane and the size of the compound to be retained during the filtration. The main problem related to membrane processes is called fouling, that is, blocking or narrowing of pores by the retained material, due to factors adsorption or deposition of filtrated compounds onto membrane surface or inside the pores, reducing permeate flux under constant transmembrane pressure. In this sense, filtration performance also depends on the membrane material.

Ceramic membranes present advantages over their polymeric equivalent, presenting a lower fouling rate, besides having greater thermal and chemical stability. However, its high cost still makes it difficult to be used on large scale. Strategies aiming at increasing the economic viability of these membranes have been pursued. Among them is the development of membranes with better performance and durability.

In this regard, the phase inversion technique has recently allowed the production of porous ceramic membranes that, with a single thermal step, present a highly selective upper layer and a lower layer with high permeability, which would be ideal. This technique can be combined with different forming techniques, including tape casting. Combining these two techniques, high permeability flat membranes can be produced. Nevertheless, fouling is still a concern.

Hybrid systems, combining membrane process and photocatalysis have been studied. Specifically, photocatalytic membranes (PM) with immobilized photocatalyst onto membrane could improve permeate flux during filtration under proper irradiation by degrading foulants onto membrane surface, as well as improve recalcitrant compounds degradation compared to batch systems with immobilized photocatalysts without permeation. Besides, light-induced hydrophilicity and self-cleaning ability are antifouling characteristics attributed to photocatalytic membranes. Membrane coating with photocatalysts is preferred for ceramic photocatalytic membranes. Flux resistances added by these coatings due to pore blocking are a concern, though.

Thus, the goal of this work was to produce photocatalytic ceramic membranes with structures suitable for microfiltration. For this purpose, alumina membranes were produced using phase inversion as the pore-forming method combined with tape casting as a conformation method. Alumina is the most used advanced ceramic material, presenting high hardness, thermal and chemical resistance, and high availability. The morphological, mechanical, and textural characterization was performed using SEM, flexural strength measurement, mercury porosimetry, and X-ray micro-computed tomography. Alumina membranes were produced using different slurry formulations and sintered at 1400 or 1500 °C after the solidifying phase inversion step. Additionally, a co-casting strategy was tested and water permeation was evaluated for all the produced membranes. Next, photocatalytic membranes were produced by depositing TiO_2 layers onto selected Al_2O_3 produced membranes by magnetron sputtering or sol-gel dip-coating. TiO_2 is known for its high stability, Earth

abundance, and activity (although it is active only under UV light), being the most investigated photocatalyst and used as a benchmark. SEM, XRD, TG/DTA, Raman analyses were executed. The photocatalytic activity was proved by methylene blue degradation in the batch system, while filtration performance and antifouling photocatalytic properties were investigated for filtration of acetaminophen, methylene blue, and synthetic oily wastewater.

1.2   OBJECTIVES

This study aimed at producing photocatalytic ceramic membranes with high antifouling capabilities for the microfiltration process applied to the treatment of effluents.

The specific objectives are presented below according to each chapter of this thesis:

Chapter 3

Synthesize alumina ceramic membranes by phase inversion combined with tape casting, which presents mechanical and morphological characteristics suitable for microfiltration processes.

Chapter 4 To develop and characterize stable photocatalytic microfiltration membranes with tailored surface porosity, functionalized by the addition of TiO_2 layers by magnetron sputtering method.

Chapter 5

Investigate the use of a sol-gel dip-coating strategy to produce TiO_2 coated photocatalytic membranes and antifouling capabilities for the treatment of organic effluents.

2 THEORETICAL BACKGROUND

This chapter presents the theoretical background and literature review for the thesis. It is part of a review paper entitled *"Development of photocatalytic membranes applied to the treatment of oily wastewater: a review*", which was submitted to a scientific journal and is currently under review. Here, the main theoretical aspects related to the membrane separation process, photocatalysis reactors, and photocatalytic membranes are presented. The understanding of these process concepts, advantages, and limitations opens new opportunities for the development of membranes with improved performance, enhancing their economic viability.

2.1   MEMBRANE SEPARATION PROCESSES

Membrane separation processes (MSP) are physical processes analogous to conventional filtration, but progressively smaller in pore size. MF and UF membranes generally have mean pore sizes (MPS) in a range of 0.05 to 5 µm and 1 to 500 nm, respectively and use a pressure gradient as the driving force. They have been used for beer and wine classification (MF), as well as separation of oily wastewater (MF/UF) and pigments (UF) [1,2,3,4]. Other nanofiltration and reverse osmosis membranes, as well as membrane distillation, have been successfully applied for treating saline oily wastewaters [5].

Membranes are produced as flat, tubular, or as hollow fibers (HF). They have been mainly fabricated from polymers and ceramic materials, but materials such as metal, glass, and textile are also used [3,6]. Ceramic membranes present superior characteristics in terms of selectivity, permeability, durability, stability, and fouling resistance compared to traditional polymeric ones [7,8].

2.2   TRANSPORT PROPERTIES AND OPERATION PARAMETERS

Permeability and selectivity are transport properties of interest. To characterize the permeability, water or effluent flux J (L m^2 h^{-1}) are calculated according to Equation (1):

$$J = \frac{1}{A} \cdot \frac{dV}{dt} \qquad (1)$$

To characterize the selectivity, the rejection coefficient (R), defined by the relation between species concentration in permeate and its concentration in the feed, according to Equation 2, is normally used.

$$R = 1 - \frac{C_p}{C_0} \qquad (2)$$

where C_p is the concentration in the permeate and C_0 is the concentration in the feed.

There is a trade-off between pore size and selectivity. The smaller the pore size, the higher the selectivity, but also the lower the flux. Nevertheless, the whole membrane morphology affects flux resistance and thus, permeation flux (Fig. 2.1) [9]. Thus, asymmetric membranes with larger pores supporting a thin surface skin layer with smaller pores sizes have been preferred.
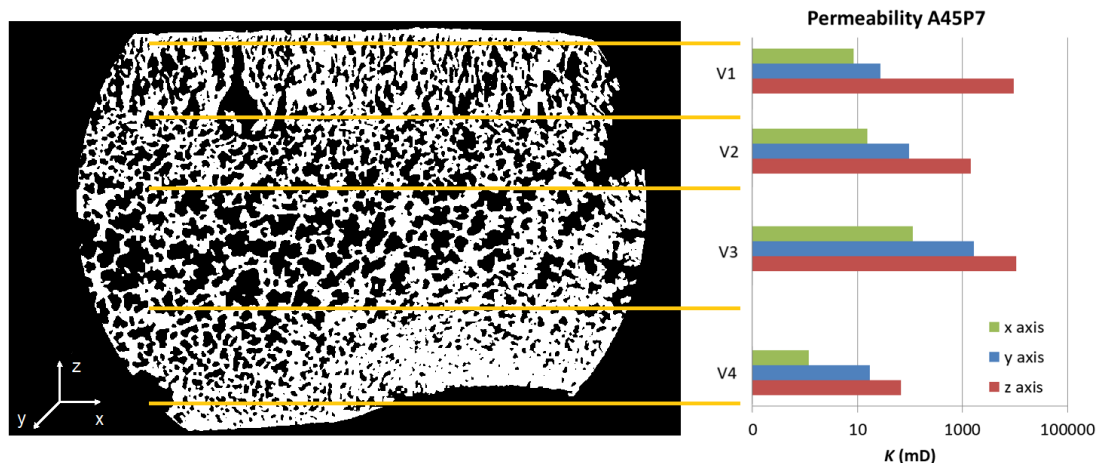
Figure 2.1 Micro-CT images (left) and results of the permeability (k) simulations (right) at different depths (V1, V2, V3, and V4) of the z-axis of an alumina membrane [9].

The membrane separation process can be operated in two different configurations: crossflow or conventional (dead-end) filtration mode (Fig. 2.2), with constant transmembrane pressure (TMP) or constant cross-flow velocity (CFV). A higher TMP can lead to higher fluxes up to a certain value, a higher value can reduce selectivity as the deformation of the oil droplets facilitates their penetration into the pores of the membrane. The same effect can be observed

for increased effluent temperature. Higher TMP can also decrease the flux by compressing the accumulated oil layer on the membrane surface [8].
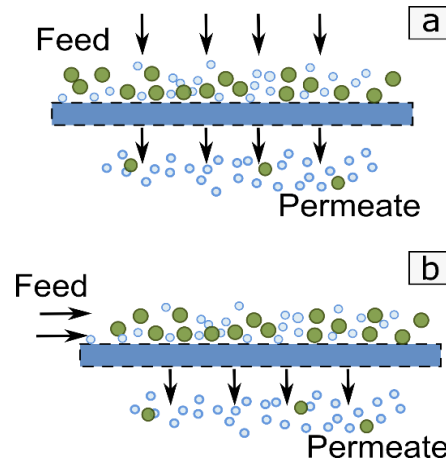
Figure 2.2 Dead-end and cross-flow filtration modes. Source: the author.

2.3 FOULING

During filtration processes, retained particles tend to accumulate on the membrane surface, inside the pores, or both, causing pore blockage or pore size narrowing. (Fig. 2.3) This phenomenon is called fouling. In practice, fouling leads to a decrease in the flux resulting in higher energy consumption and frequent pauses in operation for membrane cleaning, which reduces productivity and shortens membrane lifespan, leading to higher replacement costs [1,6].

The different fouling mechanisms (Fig. 2.3), also known as Hermia's blocking laws can be described as [10-12]:

(i)   Complete pore-blocking happens when the size of the solute particle is larger than the pore size of the membrane. Consequently, pore-blocking occurs across the surface of the membrane and not within the membrane pores.

(ii)   Standard pore-blocking assumes that the molecules penetrate the pores of the membrane and deposit on the pore walls due to anomalies in the pore passages. Generally, standard pore-blocking arises when the sizes of the solute particles are smaller than membrane pore size and thereby, pore blocking happens inside the

membrane pores. In this manner, the pore volume of the membrane decreases proportionally to the volume of the filtered permeate.

(iii)   Intermediate blocking arises when both the solute particles and the membrane pores are similar in size. For such a scenario, it is expected that the solute molecules do not essentially block the membrane pore and few particles may settle over others. Hence, the non-blocked membrane surface area decreases with time and a few molecules prevent the passage of the membrane pores without completely obstructing the pore.

(iv)   Cake filtration relates to a situation where particles bigger than the normal pore size aggregate on the membrane surface and thus facilitate the development of a ''cake''. The cake develops with time and acts as an additional porous barrier (and subsequently hydraulic resistance) for the permeating liquid.

The mathematical model for Hermia's mechanisms was developed for dead-end unstirred filtration, although modified models were developed for crossflow or stirred filtration. Governing equations can be conveniently written in a common mathematical form [13]:

$$\frac{d^2t}{dV^2} = K\left(\frac{dt}{dV}\right)^n \tag{3}$$

or

$$\frac{dJ}{dt} = -K(JA)^{2-n} \tag{4}$$

where

$$J = \frac{1}{A}\frac{dV}{dt} \tag{5}$$

$$J_0 = \frac{\Delta P}{\mu(R_t)} \tag{6}$$

where V = permeate volume, t = time, J = flux, ΔP = pressure drop, Rt = total flux   resistance, A = membrane surface area, μ = dynamic viscosity, K = plugging constant.

The exponent n characterizes the filtration model, with:

$n = 0$	Cake filtration
$n = 1$	Intermediary blocking
$n = 3/2$	Pore constriction (Standard blocking)
$n = 2$	Complete pore blocking

For each model, a different fouling severity parameter, K (plugging constant) in the Hermia's, is obtained. The best model fitting (R^2) and K values can be calculated by plotting experimental filtration data in terms of $J, t,$ and V, according to the equations derived from each fouling model. For the same model with good fitting, the value of K gives physical significance as it influences the fouling of the membranes [10].
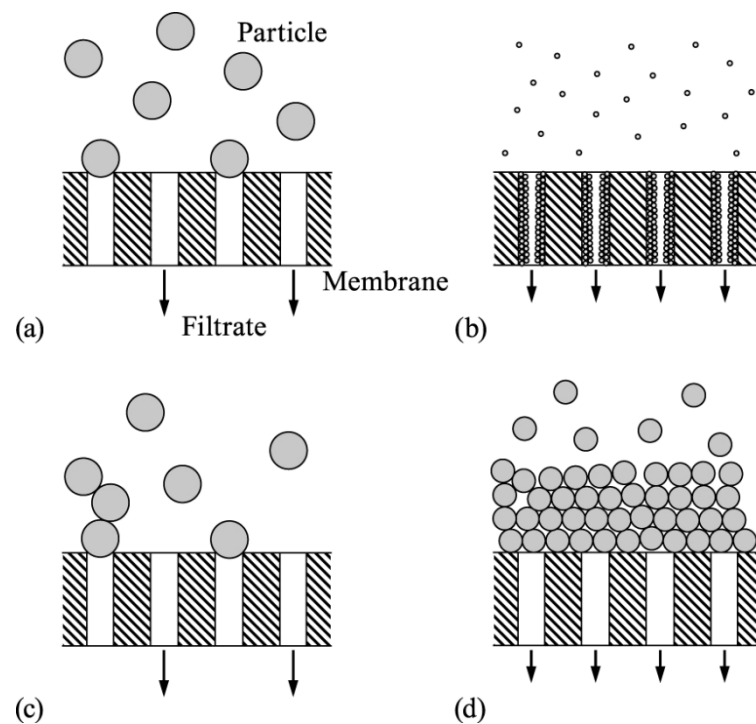
Figure 2.3 Membrane fouling mechanisms [12].

The occurrence of fouling inside the pores depends mainly on the ratio between membrane surface pore size and pollutant particle size. Operation at higher TMP may result in denser fouling layers. In the case of oily wastewater, deposition of oil inside the pores happens

due to dropping deformation. Temperature also facilitates oil droplets to deform and enter the pores, due reduction of oil viscosity. Additionally, the dead-end filtration mode tends to present more serious problems with fouling due to the accumulation of the total amount of foulants on the membrane surface and by compressing it. Nevertheless, fouling formation is related to a set of parameters that also includes the membrane surface chemistry, structure, and charge as well as effluent properties that strongly influence the fouling formation. The higher the feed concentration, the thicker the fouling layers formed on the membrane, resulting in a higher dropping of the flux [1,3,6,13–18].

Considerable efforts have been made in process intensification to improve MSP performance in wastewater treatment by developing membranes and processes with different fouling mitigation strategies [6,7,19–22]. Among them, hydrophilic materials or hydrophilic surface functionalization, hybrid or combined processes, and reactive or catalytic membranes should be mentioned [3,6,23–25].

2.4   HETEROGENEOUS PHOTOCATALYSIS

Photocatalysis stands out for advantages such as operation under mild conditions (ambient temperature and pressure), the absence of chemical additives, and principally the possibility of degrading refractory, toxic, and non-biodegradable compounds, even in low concentrations [26]. It is an Advanced Oxidative Process based on the activation of a solid photocatalyst when it is irradiated by a light source with adequate energy, i.e. with energy equal to or greater than its bandgap, E_{BG} (Equation 7). In general, the photocatalyst is a semiconductor, with TiO_2 being the most studied. However, other materials such as ZnO, ZnS, semiconductor-graphene composites, perovskites, MoS_2, and WO_3 have been investigated [27].

$$E_g = \frac{h.c}{\lambda} \quad\quad\quad (7)$$

where E_g is the bandgap energy, h is the Planck's constant (6.626×10^{-34} J s), c is the speed of light in vacuum (2.998×10^8 m s^{-1}) and λ is the light peak emission wavelength (nm). Numerous researches in the area of photocatalysis seek to overcome its main limitations: (i) the high recombination of the electron-gap pairs of conventional photocatalysts and (ii) the low absorption in the visible compared to the absorption of UV radiation, which results in high

energy consumption with artificial lighting. Metal [28,29] and non-metal [30,31] doping of different photocatalysts have been used to improve photocatalytic activity under UV and/or visible light [27]. Specifically, TiO$_2$ can only be activated by UV light due to its bandgap energy (E$_{BG}$ = 2.8 eV)

The formation of reactive oxygen species on the TiO$_2$ surface under UV light irradiation is shown in Equations 8-13 and schematized in Fig. 2.4. When a photocatalyst is irradiated by an energy (*hv*) source with a suitable wavelength, electrons are shifted from the valence band (VB) to the conducting band (CB) of the material, forming an electron-hole pair. Immediately afterward, electron (e$^-$) and hole (h$^+$) migrate to the catalyst surface and can react with electron acceptors and donor molecules, respectively [32,33].

$$TiO_2 + hv \quad \leftrightarrow \quad TiO_2(e^-, h^+) \tag{8}$$

$$h^+ + RX_{ads} \rightarrow RX_{ads}{}^+ \bullet \tag{9}$$

$$h^+ + H_2O_{ads} \rightarrow HO_{ads} \bullet + H^+ \tag{10}$$

$$h^+ + OH^-{}_{ads} \rightarrow OH_{ads} \bullet \tag{11}$$

$$e^- + O_{2\,ads} \rightarrow O_2^- \bullet \tag{12}$$

$$e^- + H_2O_{2\,ads} \rightarrow OH^- + OH_{ads} \bullet \tag{13}$$
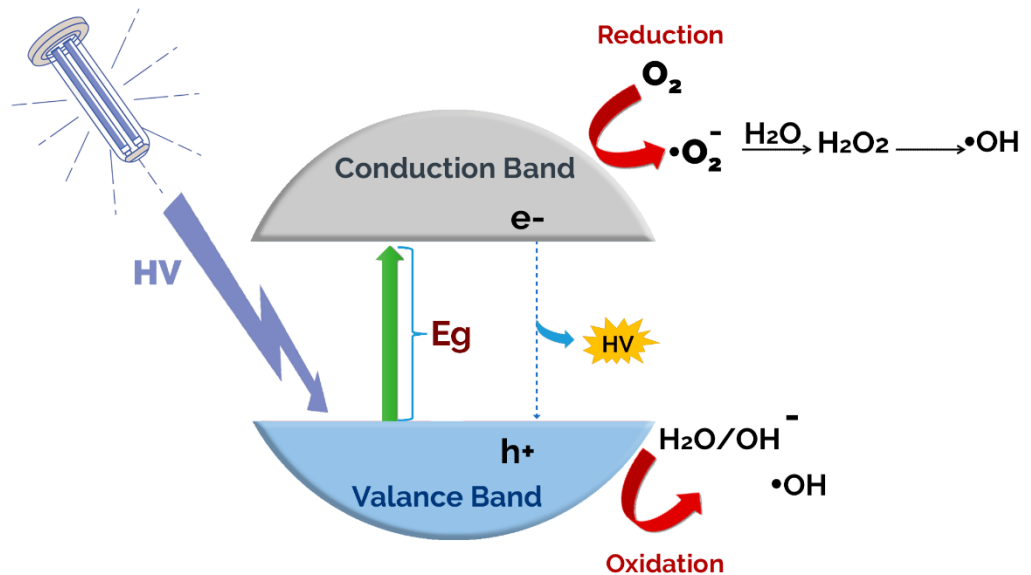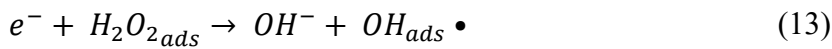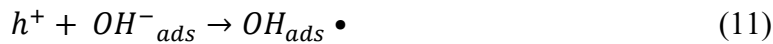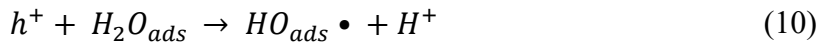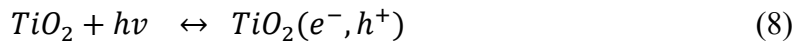
Figure 2.4 Principle of photocatalysis and formation of reactive oxygen species [32].

In general, the acceptor molecule is molecular oxygen, O_2, leading to the formation of superoxide, O_2^- (Equation 12), and peroxides, H_2O_2 (Equation 13), while water and other oxidizable organic or inorganic species react with the positive hole in the valence band. Oxidation usually results in hydroxyl radical, •OH, considered the most important species in the photocatalytic degradation process. •OH oxidation potential is 2.8 eV, being able to oxidize a broad range of compounds. Photo-generated electron/hole pairs can also recombine, hindering photocatalysis efficiency.

Since O_2 and H_2O_2 can act as electron acceptors, preventing recombination of electron-hole pairs (e^-/h^+) air bubbling and H_2O_2 addition are common strategies to enhance reaction rates. For example, the presence of H_2O_2 improved the diesel (0.2 g L^{-1} in seawater, pH 8) removal by Yb_2O_3-doped ZnO photocatalyst (0.6 g L^{-1}) under visible light, from around 31% in absence of oxidant to more than 83% after 2 h when 6.0 mg L^{-1} of H_2O_2 was used. In the absence of photocatalyst or oxidant, diesel removal of 27% was found and attributed to evaporation. On the other hand, H_2O_2 also acts as a scavenger for the formation of hydroxyl radicals (•OH) and superoxide (•O_2), besides being formed as an intermediary during the photocatalytic reaction. In turn, optimal conditions need to be defined [34]. Similarly, O_2 (or air) inlet flow may improve photocatalytic degradation rate enhancing superoxide molecules (•O_2) formation rate and preventing electron-hole recombination, while an excess of bubbles can hinder the proper irradiation of the catalyst surface.

Besides the presence of O_2 and H_2O_2, photocatalytic reaction rates are primarily influenced by photocatalyst properties, pollutant composition, and the light source (wavelength), as well as the operational conditions (mass of the photocatalyst, the pollutant concentration, the radiation intensity, reactor geometry, for example), and the combination of the different factors. Different photocatalytic degradation rates were found for different molecules present in biodiesel (carbon content between C14 – C18, with different chemical bonds). •OH is more likely to attack the methylene bridges, followed by mono-allylic and aliphatic sites [35]. Concerning the photocatalyst dosage in slurry reactors, for a given system, the reaction rate is proportional to the active sites on the catalyst surface (and thus to catalyst mass) until the full adsorption of photon from the luminous source. After this point, the reaction rate remains constant. As for the initial concentrations of organic pollutants, photocatalytic reactions usually follow the Langmuir–Hinshelwood mechanism model. In this case, the reaction rate increases when the feed concentration increases until achieving a plateau. When

the adsorption is weak and/or the concentration of the pollutant is low, the kinetics can be simplified to a pseudo-first-order kinetic [36] and the concentration of a pollutant along photocatalytic reaction time can be expressed according to Equation 16, with an apparent constant k_{app} (min^{-1}):

$$ln \frac{C}{C_0} = -k_{app}t \qquad (16)$$

where t is the reaction time, C is the concentration along the time t and C_0 is the initial concentration. Nevertheless, excess photocatalyst in suspension or pollutant concentration could also add opacity to the feed solution, hindering the proper irradiation of the catalyst and reducing the photocatalytic activity [37]. The reaction rate is strongly positively influenced by the radiant flux of the light source, ϕ $(W\ m^{-2})$. However, if the radiation fluxes are too high, they can increase the recombination rate of electrons and holes and thus reduce the influence factor [38]. Despite the importance of the radiant flux, only the overall lamp power is stated in most of the research papers.

The effect of pH on pollutant degradation may differ depending on the pollutant composition, even when compounds possess similar structures. Results also showed a pH reaction rate dependence according to reactor and light source geometry [39]. The temperature has a small influence on the reaction rate, which results from the equilibrium between the adsorption and desorption constants, and the reaction rate constant of the Arrhenius law, all of which are dependent on temperature. Nevertheless, in most cases, photocatalytic reactions are performed at room temperature and small temperature variations are disregarded. In contrast, optimal pH, H_2O_2 concentration, and dissolved O_2 values are described [34].

The presence of some salts and scavengers (such as carbonate and bicarbonate ions) may reduce photocatalytic activity as they occupy adsorption sites on the surface of the photocatalyst or react with reactive oxygen species formed on the photocatalyst surface. Nevertheless, iron and manganese ions present in wastewaters can contribute to the Fenton and photo-Fenton reactions in acidic conditions [40]. Finally, when analyzing photocatalytic activity, pollutant removal by adsorption [41] and photolysis [42] should also be investigated so as not to be confused with photocatalytic pollutant removal.

2.5   PHOTOCATALYTIC MEMBRANE REACTORS

Hybrid systems that combine the technology of photocatalysis and membrane separation have been intensively studied in different settings. They are commonly called Photocatalytic Membrane Reactors (PMR). In general, PMRs are studied in two main configurations: reactor with suspended catalyst (slurry) (Fig. 2.5a and 2.5b) and reactor with catalyst immobilized in/on the membrane (Fig. 2.5c). Mozia   [4] discussed different configurations of PMR addressing the advantages, disadvantages, and performance of each one. Nevertheless, slurry PMRs do not differ significantly from a sequential photocatalysis-membrane process, where membranes will play the role of separation barrier for the photocatalyst only or both, residual contaminants and photocatalyst particles. Thus, the focus will be given to the second PMR type configuration, i.e., the use of photocatalytic membranes (PMs) [37].

PMs may be produced by adding catalyst as a coating on commercial or produced membranes, or by adding it as filler during the synthesis of membranes. [2,43]. The membrane acts as a support for the catalyst, as well as a separation barrier for the molecules present in the solution. Thus, pollutants photo-decomposition takes place on the membrane surface itself or inside the pores. Therefore, it is required to guarantee the membrane is efficiently illuminated [4] (Fig. 2.5c). Although TiO_2 membranes are commercially available, TiO_2 tends to lose its photocatalytic activity during ceramic membrane production when phase transition temperature is exceeded (up to 600 °C), as normally occurs during ceramic processing. Thus, to produce photocatalytic ceramic membranes with high mechanical strength, a catalytic layer should be applied in the second step after thermal treatment of the support. The resulting titania phase as well as its photocatalyst activity and pore blockage due to coating deposition need to be investigated.

The performance of a PMR using PVDF membranes blended with TiO_2 and separate photocatalytic (PR) and ultrafiltration (UF) systems (PR-UF) using powdered TiO_2 have been compared by Moslehyani et al. [26]. Ballast water (583 ppm of oil) was used for both experiments. In the first, the oily water was irradiated for 6 h by UV light inside PMR, afterward UV lights were switched-off and membrane filtration was started. For the second one, the powdered catalyst was suspended in the oily water in PR and irradiated for 6 h, and then, filtered by UF hollow fibers for 1 h. PR-UF hybrid system could degrade TOC by over 80%, which

was 10% more than PMR. However, in the PR-UF system, flow decayed due to the deposition of oil and agglomeration of the catalyst particles on the membrane surface. On the other hand, the reduction of COD and total dissolved solids by PMR was higher than PR-UF. Additionally, the authors compared TiO$_2$ blended nanocomposite membrane to the neat PVDF one without any photocatalyst in suspension. TiO$_2$ blended membrane showed better permeation flux, rejection, and antifouling capacity.
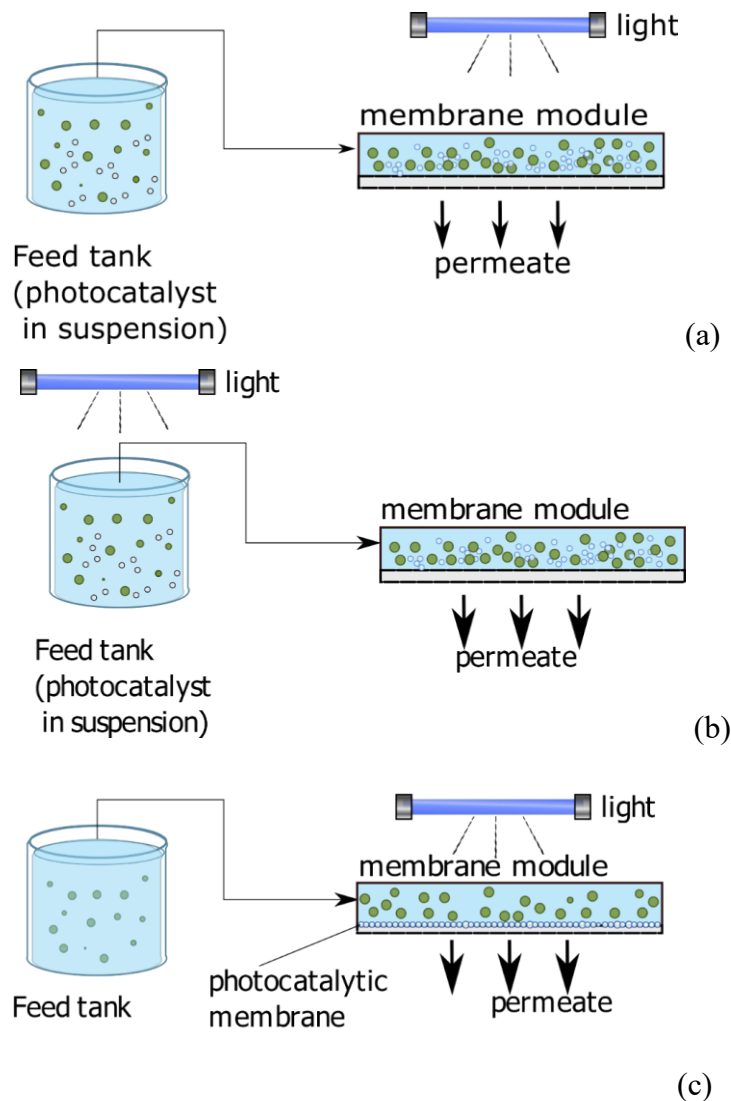
Figure 2.5 Schemes of different photocatalytic membrane reactors [37].

PMs can be applied for the degradation of pollutants as part of the wastewater treatment itself (as in the slurry systems) or mainly for the photocatalytic degradation of foulants as a strategy to maintain the membrane separation process performance. PMs tend to show enhanced

filtration performance compared to conventional membranes [43,44]. The main PM fouling reduction mechanisms, as well the main parameters affecting PM performance are discussed in the next section (Section 2.5.1).

2.6   Photocatalytic membranes for effluent treatment

Fig. 2.6 presents the main antifouling mechanism reported for PM applied to the effluents, regard or regardless of the presence of light. Hydrophilic surfaces are well known for improving the filtration performance of aqueous effluents, in special those containing hydrophobic compounds such as oil. Thus, contact angle measurements have been performed in most of the works. Concerning chemical composition, oxide photocatalysts such as TiO_2, ZrO_2, Fe_2O_3, and graphene oxide (GO), have been used to functionalize the surface by providing hydroxyl (OH) surface groups in abundance, improving the hydrophilic character [45–51]. Pre-wetting a rough hydrophilic surface before filtration improves antifouling performance by trapping water on the roughness allowing the formation of a hydration layer at the membrane interface (Fig. 2.7) [17,52,53]. Different approaches have been used to investigate the photocatalytic effect of PMs, such as (i) irradiation self-cleaning capabilities of fouled membranes after filtration; (ii) photocatalytic oil foulants in the batch system (including photodegradation followed by filtration); and/or (iii) effect of light irradiation during the filtration could be cited.

General
- Reduction of density of fouling layer due highly porous coating
- Adsorption
- Hydrophilicity (surface chemistry and roughness)

Light-induced
- Decomposition of foulants during or after filtration
- Decomposition of soluble compounds during filtration
- Reduction irreversible fouling
- Light induced hydrophilicity
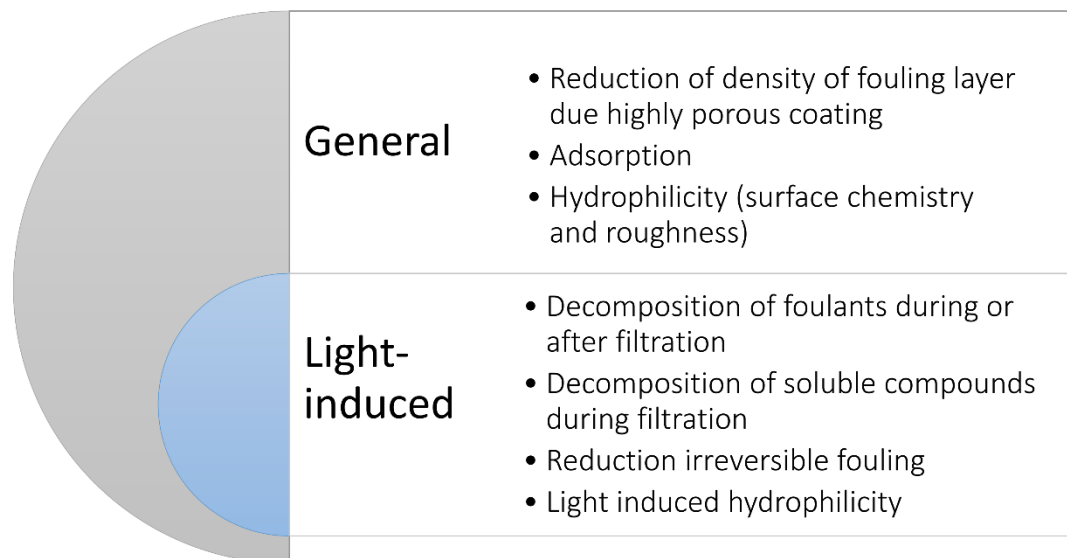
Figure 2.6 Different fouling reduction mechanisms for PM applied to the treatment of oily wastewater. Source: the author.
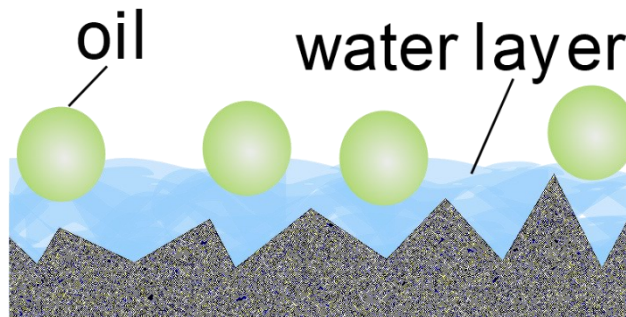
Figure 2.7 Underwater oleophobic surface based on hydration layers. Source: the author.

Zhang et al. [54] investigated the influence of surfactants charges. A SPAN@GO/M88A membrane with a positive surface charge was used to filter Tween 80-, SDS- and CTAB-stabilized emulsions containing uncharged, negatively, and positively charged oil droplets. Higher flux and improved surface cleaning were obtained for the emulsion with the same charge as the surface, CTAB. Fouling mechanisms were explained as follows (Fig. 2.8): uncharged droplets (Tween-80-stabilized) easily resulted in the formation of cake layers on the membrane surface. Negative charged SDS-stabilized emulsion can be attracted to the positive membrane surface and destabilize the colloids, resulting in demulsification. While the demulsification has been associated with oil coalescence, which further makes it difficult for droplets to enter membrane pores [55-57], the accumulation of SDS on the membrane by adsorption gradually reduces the demulsification effect and blocks the pores. Finally, the interaction between the positive surfaces of the droplets and the membrane destabilizes the droplets and promotes their coalescence, while the surface also repels the CTAB molecules so that they cannot be adsorbed on the membrane surface.

Highly porous or voluminous hydrophilic coatings could not only facilitate hydration layers to be formed [58], but also prevent dense fouling layers to be formed on membrane surface as for nsGCN-embedded PAN nanofiber coating mesh on asymmetric alumina (Al_2O_3) produced by Alias et al. [59]. Similarly, increasing GO [53] or MXene [17] interlayer spacing on membrane coatings improves water fluxes. Furthermore, the disturbance of the laminar flow caused by the coating layer along the membrane surface during cross-flow operation could also improve membrane flux [59].
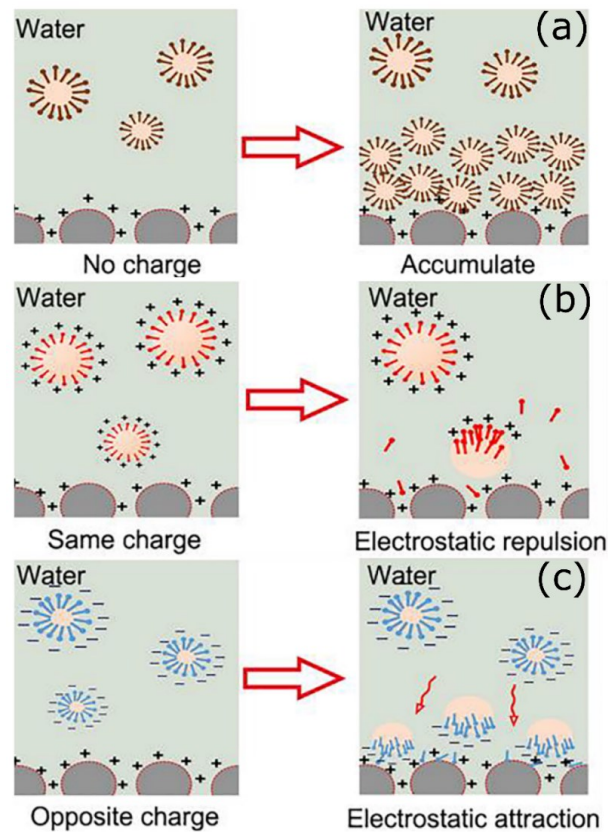
Figure 2.8 Schematic illustration of demulsification by electrostatic interaction for separating different surfactant-stabilized emulsions. Adapted from Zhang et al. [54], reproduced with permission.

2.6.1 Dynamic photocatalysis-filtration

Online photocatalytic degradation during effluent filtration resulted in overall higher fluxes under irradiation compared to operation in the dark indicating that foulants adhering to the outer surface were degraded and cleansed the outer surface of membranes, as can be seen in Fig. 2.9a, where F005 and F05 are Fe_2O_3-coated Al_2O_3 membranes, using thinner and thicker Fe_2O_3 coating layers for the filtration of oily wastewater [60]. The effect of coating thickness is discussed in Section 2.5.1.2. Light-induced flux enhancement reported by Alias et al. [60] is in agreement with those reported by Yue et al. [61]. The authors have produced ZIF-8/GO-coated PVDF membranes. Flux was highly improved along with filtration for the PM membranes under a 500 W Xenon lamp and 0.14 MPa TMP (Fig. 2.10). Besides, light-induced hydrophilicity could enhance flux by repelling oil molecules (Fig. 2.11) [16,61]. Finally, TOC and oil rejection were also improved during filtration under irradiation. (Fig. 2.9c) [16,60].

(a)

(b)
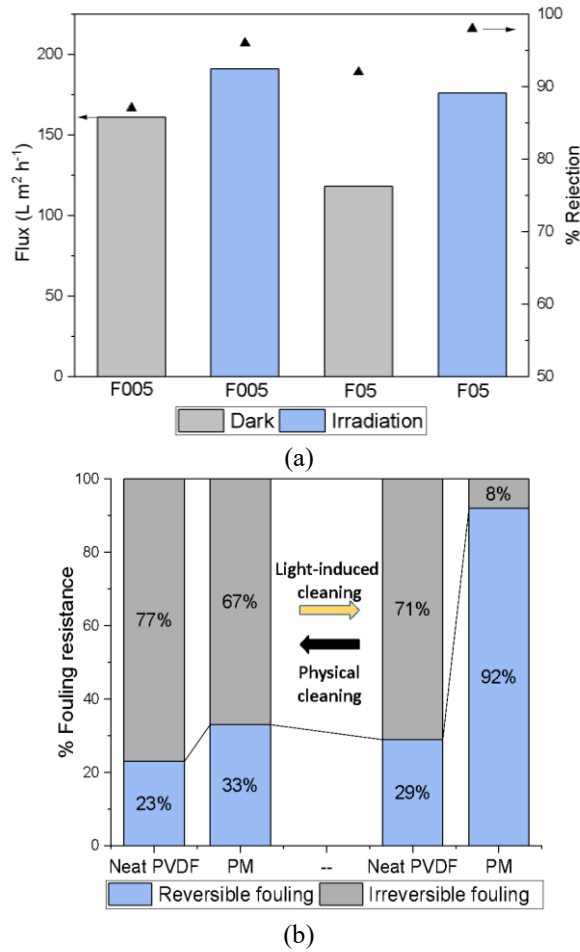
Figure 2.9 (a) Flux and oil rejection in darkness and under radiation for membranes coated with thinner (F005) and thicker (F05) Fe_2O_3 coatings onto Al_2O_3 membranes. Data extracted from Paiman et al. [60] with the software GetData Graph Digitalizer© version 2.26.0.20; (b)reversible and irreversible fouling contributions for Neat PVDF and GO/MCU-C_3N_4/PVDF (PM) membranes after light-induced or physical cleanings. Data extracted Shi et al. [53] with the software GetData Graph Digitalizer© version 2.26.0.20.
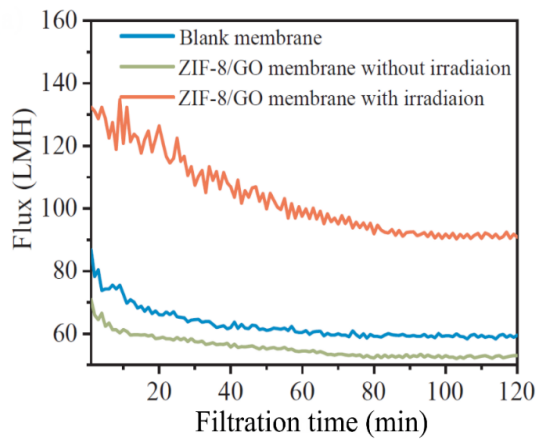
Figure 2.10 (a) Flux of blank and ZIF-8/GO-coated PVDF membranes, with and without irradiation Adapted from Yue et al. [61], reproduced with permission.
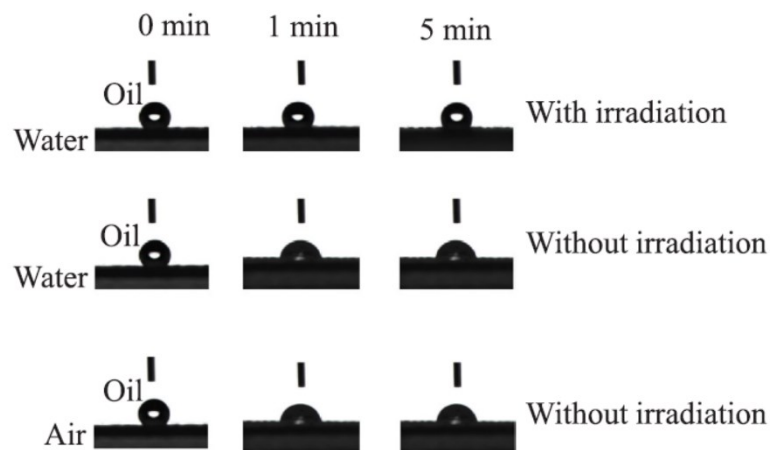
Figure 2.11 Light-induced hydrophilicity. Adapted from Yue et al. [46], reproduced with permission.

Filtration flux under irradiation can be constant and equal to initial flux when the degradation rate on the membrane surface is higher than the foulant deposition rate. If both rates are equal, equilibrium can be achieved [25]. In turn, the fouling deposition rate may also be higher than the fouling degradation rate, resulting in a decrease of the flux along the time, especially for high oil concentrations, as seen in Fig. 2.10. In this case, cleaning breaks are still necessary. Membrane cleaning procedures incur process downtime, in addition to the possibility of membrane damage. The use of PM under UV irradiation can extend membrane operating cycles, reducing operational costs and increasing the membrane [61,62].

Furthermore, in situ degradation of various small molecules such as dyes [63], dioxins and pesticides [52] and pharmaceuticals [64] during oil-water emulsions separation with PM under irradiation have also been demonstrated. The benefits of degrading pharmaceuticals by permeating them through PM under irradiation were recently reported by Li et al. [44]. The authors demonstrated a high carbamazepine degradation during irradiated filtration compared to static batch reaction or reaction with the surface flow without permeation. Although the drug compound showed a low retention rate under dark conditions and the results compared to batch reaction were mainly attributed to degradation due to improved contact between compound and photocatalytic surface

Increasing pollutant concentration in the effluent result in thicker fouling layers on the membrane surface. It affects UV penetration and, thus, reduces photocatalytic surface activation [36]. TOC removal of cutting oil emulsion with different concentrations was evaluated using

photocatalytic hollow fiber PVDF membranes blended with TiO_2 under an 8W UV light, in a PMR with full recirculation of permeate and retentate. TOC removal was remarkably reduced when oil concentration was increased from 100 to 5000 and 1000 ppm (Fig. 2.12). This result is in agreement with the apparent rate constant (k_{app}) found for TOC degradation for the different oil concentrations. The k_{app} values changed from 2.9 x10^{-3} min^{-1} when 250 ppm emulsion was used to 2.0 x10^{-3}, 1.0 x10^{-3}, and 0.2 x10^{-3} min^{-1} respectively, when 1000, 5000, and 10000 ppm emulsion were investigated. Nevertheless, irradiation of PM during filtration is expected to be beneficial for membrane performance. Although flux can decrease even under irradiation, flux drop can be attenuated by partial fouling layer decomposition [36,60,64].

In this sense, a stronger positive effect on the reduction of fouling would be expected if light irradiation is present from the beginning of filtration. This early effect is not only similar to the effect of wetting a membrane but could also complement it to form a protective hydration layer before the oil touches the membrane surface. Nevertheless, although both superhydrophilicity and photocatalytic activity are important properties for PMs for oily wastewater, the relationship between them in terms of best overall membrane performance may not be direct.
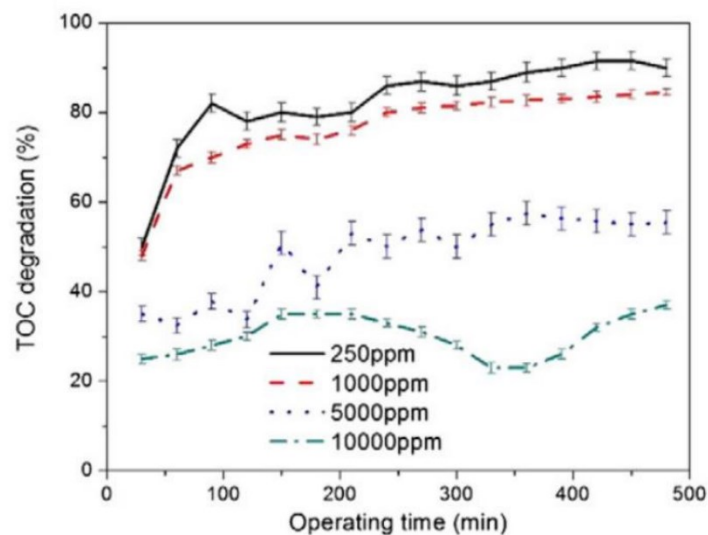
Figure 2.12 Effect of feed concentration on TOC degradation for a PVDF-TiO_2 membrane under UV irradiation for TOC degradation at different feed oil concentrations. From Ong et al. [36], reproduced with permission.

2.6.2 Cleaning performance

Membrane cleaning is an important issue. Light-induced surface cleaning after filtration has been reported. Cleaning performance has been evaluated in terms of Flux Recovery Ratio (FRR), Flux Decline Ratio (FDR) (or Total Fouling Ratio - R_t), Reversible Fouling Ratio (R_r), and Irreversible Fouling Ratio (R_{ir}) [53]:

$$FRR = \frac{J_{w2}}{J_{w1}} \, x100\% \tag{18}$$

$$FDR = 1 - \frac{J_f}{J_{w1}} x100\% \tag{19}$$

$$R_r = 1 - \frac{J_{w2} - J_f}{J_{w1}} x100\% \tag{20}$$

$$R_{ir} = \frac{J_{w1} - J_{w2}}{J_{w1}} x100\% \tag{21}$$

where: J_{w1} and J_{w2} represent the water permeate flux before filtration and after membrane cleaning, J_f is the permeate flux of the fouled membrane; R_r and R_{ir} represent reversible and irreversible fouling, respectively. Thus, higher FRR and lower FDR indicate good self-cleaning and antifouling properties, respectively. The use of PM has resulted in superior reversible/irreversible fouling ratios [53,59,65,66].

Shi et al. [53] prepared GO/MCU-C$_3$N$_4$/PVDF photocatalytic membranes. %Reversible fouling after diesel filtration was improved from 33% reversible fouling after physical cleaning to 92% after physical cleaning followed by 30 minutes of cleaning under visible light (Fig. 2.9b). In turn, the %reversible fouling values for bare PVDF membranes were only 23 and 29%, respectively. When choosing the better overall performance, the operation conditions and membrane performance for long-term operation must be taken into account, though.

2.6.3 Effect of coating coverage and pore size on antifouling effect

The improvements of the flux depend on membrane properties in addition to the operation details. Higher catalysts loading tends to provide higher antifouling properties up to a certain point. It should be noted that the antifouling properties may not achieve the desired

effect if the membrane coating does not completely cover the membrane or does not adhere well to the membrane surface [65]. Similarly, if a membrane presents a low rejection coefficient, extended fouling happens inside the pores. Since (i) photocatalysis is a surface reaction that requires activation by a luminous source and (ii) photocatalysts are mainly coated only onto the membrane surface and not inside the pores, degradation reactions are likely to happen only on the irradiated and coated membrane surface. Consequently, the PM will not be able to decompose these foulants, and the pores will progressively become clogged. Nevertheless, there is still a lack of studies on the consequences of fouling inside the pores for coated PM membranes or regarding the depth and intensity of irradiation penetration which would still be able to photocatalytically degrade foulants within the membrane pores in the case of membranes blended with photocatalysts.

On the opposite, excess photocatalyst may hinder membrane flux. There is a trade-off effect between permeation flux and separation efficiency. The increasing quantity of nanoparticles on the membrane could facilitate the selectivity of the membrane as well as the photocatalytic activity, but reduce permeability due to particles agglomeration which causes pore sizes reduction and increase the flux resistance [17,59,60]. The deposition of α-Fe_2O_3 onto Al_2O_3 hollow fiber membranes increased water flux from 1003 to 1370 L m^2 h^{-1} and 1148 L m^2 h^{-1} when 0.05 and 0.5 M of Fe were used during coating preparation [60]. Flux reduction for the higher Fe concentration was attributed mainly to the formation of additional layers on the membrane surface (Fig. 2.13 right side) which reduced pore size (Fig. 2.13 left side) and created additional transport resistance for the coated membrane with thicker F_2O_3 layers (Fig 2.13), compared to the bare membranes (Fig. 2.13 a, b) or the membranes with lower F_2O_3 concentration (Fig. 2.13 c, d).

Finally, it should be noted that the successful development of photocatalytic membranes depends on both membrane support and coating layer properties and performance. Thus, the first part of this thesis is focused on the development of high-permeability ceramic membranes (Chapter 3). Afterward, the development of PM using TiO_2-coating layers was investigated (Chapters 4 and 5).

.
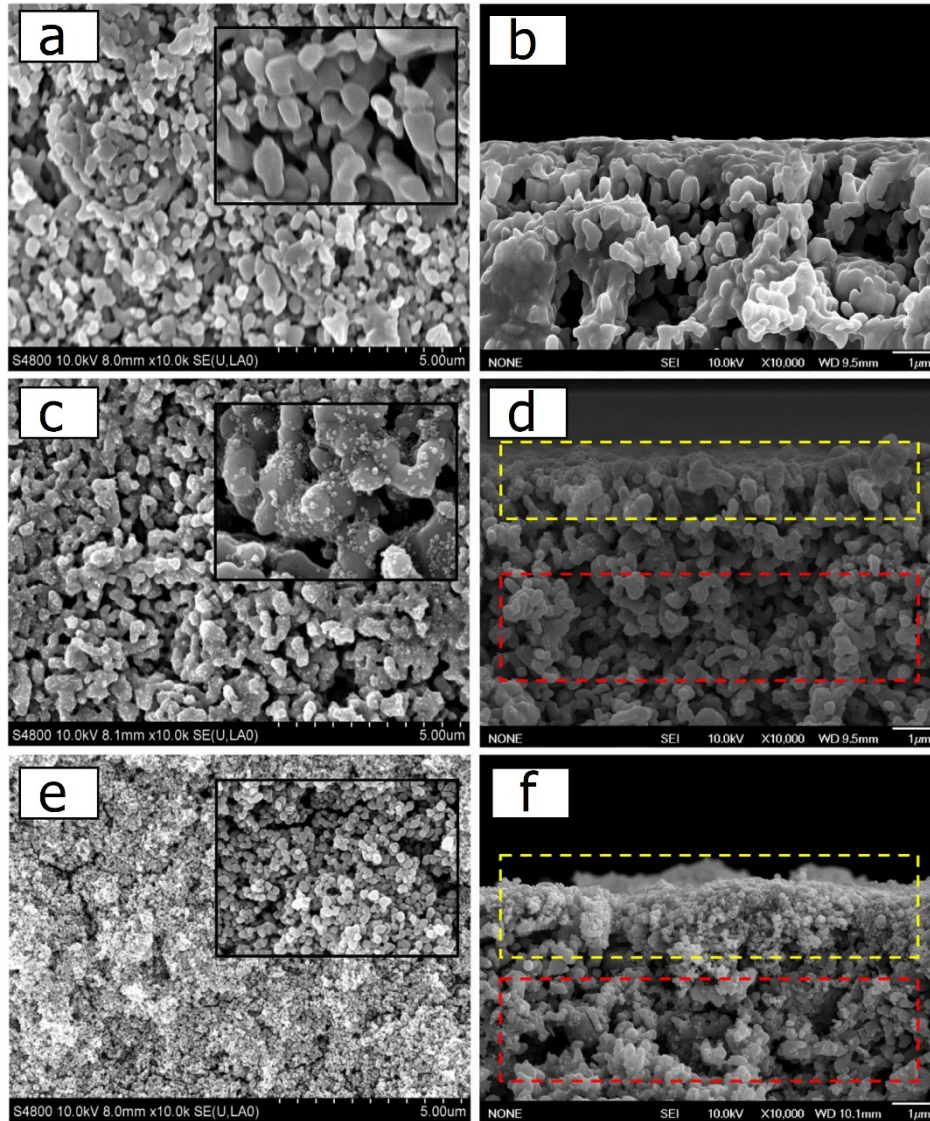
Figure 2.13 The structural images of the outer surface (left side) and cross-section (right side) of pristine and deposited porous α-Fe_2O_3 on Al_2O_3/YSZ hollow fiber membrane at different concentrations; (a, b) Pristine, (c, d) 0.05M (F005) and (e, f) 0.5M (F05). Adapted from Paiman et al. [60], reproduced with permission.

2.7   REFERENCES

[1]   M. Padaki, R.S. Murali, M.S. Abdullah, N. Misdan, A. Moslehyani, M.A. Kassim, N. Hilal, A.F. Ismail, Membrane technology enhancement in oil – water separation. A review, Des. 357 (2015) 197–207. https://doi.org/10.1016/j.desal.2014.11.023.

[2]   S. Leong, A. Razmjou, K. Wang, K. Hapgood, X. Zhang, H. Wang, TiO_2 based photocatalytic membranes: A review, 472 (2014) 167–184. https://doi.org/http://dx.doi.org/10.1016/j.memsci.2014.08.016.

[3]   M.R. Ataabadi, A.H. Behroozi, Improvement in microfiltration process of oily wastewater: A comprehensive review over two decades, J. Environ. Chem. Eng. 9 (2021) 104981. https://doi.org/10.1016/j.jece.2020.104981.

[4]   S. Mozia, Photocatalytic membrane reactors (PMRs) in water and wastewater treatment. A review, Sep. Purif. Technol. 73 (2010) 71–91. https://doi.org/10.1016/j.seppur.2010.03.021

[5]   H.J. Tanudjaja, C.A. Hejase, V. V. Tarabara, A.G. Fane, J.W. Chew, Membrane-based separation for oily wastewater: A practical perspective, Water Res. 156 (2019) 347–365. https://doi.org/10.1016/j.watres.2019.03.021.

[6]   S. Huang, R.H.A. Ras, X. Tian, Antifouling membranes for oily wastewater treatment: Interplay between wetting and membrane fouling, Curr. Opin. Colloid Interface Sci. 36 (2018) 90–109. https://doi.org/10.1016/j.cocis.2018.02.002.

[7]   P.S. Goh, A.F. Ismail, A review on inorganic membranes for desalination and wastewater treatment, Desalination. 434 (2018) 60–80. https://doi.org/10.1016/j.desal.2017.07.023.

[8]   S.M. Samaei, S. Gato-Trinidad, A. Altaee, The application of pressure-driven ceramic membrane technology for the treatment of industrial wastewaters – A review, Sep. Purif. Technol. 200 (2018) 198–220. https://doi.org/10.1016/j.seppur.2018.02.041.

[9]   L.L. Coelho, M. Di Luccio, D. Hotza, R. de Fátima Peralta Muniz Moreira, A.C. Moreira, C.P. Fernandes, K. Rezwan, M. Wilhelm, Tailoring asymmetric Al_2O_3 membranes by combining tape casting and phase inversion, J. Memb. Sci. 623 (2021) 119056. https://doi.org/10.1016/j.memsci.2021.119056.

[10]   K. Suresh, G. Pugazhenthi, Cross flow microfiltration of oil-water emulsions using clay based ceramic membrane support and TiO_2 composite membrane, Egypt. J. Pet. (2016) 679–694. https://doi.org/10.1016/j.ejpe.2016.10.007.

[11]   J. Hermia, Blocking Filtration: Application to Non-Newtonian Fluids in Mathematical models and design methods in solid-liquid separation., 1982.

[12]   E. Iritani, N. Katagiri, Developments of blocking filtration model in membrane filtration, KONA Powder Part. J. 2016 (2016) 179–202. https://doi.org/10.14356/kona.2016024.

[13]   C.-C. Ho, A.L. Zydney, A Combined Pore Blockage and Cake Filtration Model for Protein Fouling during Microfiltration, J. Colloid Interface Sci. 232 (2000) 389–399. https://doi.org/10.1006/jcis.2000.7231.

[14]   Q. Zhang, H. Wang, X. Fan, F. Lv, S. Chen, X. Quan, Surface & Coatings Technology Fabrication of TiO_2 nano fiber membranes by a simple dip-coating technique for water treatment, 298 (2016) 45–52. https://doi.org/10.1016/j.surfcoat.2016.04.054.

[15]   E. Tummons, Q. Han, H.J. Tanudjaja, C.A. Hejase, J.W. Chew, V. V. Tarabara, Membrane fouling by emulsified oil: A review, Sep. Purif. Technol. 248 (2020). https://doi.org/10.1016/j.seppur.2020.116919.

[16]   A. Golshenas, Z. Sadeghian, S.N. Ashrafizadeh, Performance evaluation of a ceramic-based photocatalytic membrane reactor for treatment of oily wastewater, J. Water Process Eng. 36 (2020) 101186. https://doi.org/10.1016/j.jwpe.2020.101186.

[17]   J. Hu, Y. Zhan, G. Zhang, Q. Feng, W. Yang, Y.H. Chiao, S. Zhang, A. Sun, Durable and super-hydrophilic/underwater super-oleophobic two-dimensional MXene composite lamellar membrane with photocatalytic self-cleaning property for efficient oil/water separation in harsh environments, J. Memb. Sci. 637 (2021) 119627. https://doi.org/10.1016/j.memsci.2021.119627.

[18]   X. Zhao, R. Zhang, Y. Liu, M. He, Y. Su, C. Gao, Z. Jiang, Antifouling membrane surface construction: Chemistry plays a critical role, J. Memb. Sci. 551 (2018) 145–171. https://doi.org/10.1016/j.memsci.2018.01.039.

[19]   L.T. Nyamutswa, B. Zhu, S.F. Collins, D. Navaratna, M.C. Duke, Light conducting photocatalytic membrane for chemical-free fouling control in water treatment, J. Memb. Sci. 604 (2020) 118018. https://doi.org/10.1016/j.memsci.2020.118018.[20]   A.A. Olajire, Recent advances on the treatment technology of oil and gas produced water for sustainable energy industry-mechanistic aspects and process chemistry perspectives, Chem. Eng. J. Adv. 4 (2020) 100049. https://doi.org/10.1016/j.ceja.2020.100049.

[21]   S. Putatunda, S. Bhattacharya, D. Sen, C. Bhattacharjee, A review on the application of different treatment processes for emulsified oily wastewater, Int. J. Environ. Sci. Technol. 16 (2019) 2525–2536. https://doi.org/10.1007/s13762-018-2055-6.

[22]   I. Kovács, G. Veréb, S. Kertész, C. Hodúr, Z. László, Fouling mitigation and cleanability of TiO_2 photocatalyst-modified PVDF membranes during ultrafiltration of model oily wastewater with different salt contents, Environ. Sci. Pollut. Res. 25 (2018) 34912–34921. https://doi.org/10.1007/s11356-017-0998-7.

[23]   M.M. Pendergast, E.M.V. Hoek, A review of water treatment membrane nanotechnologies, Energy Environ. Sci. 4 (2011) 1946. https://doi.org/10.1039/c0ee00541j.

[24]   I. Koyuncu, R. Sengur, T. Turken, S. Guclu, M. Pasaoglu. Advances in water treatment by microfiltration, ultrafiltration, and nanofiltration. Advances in Membrane Technologies For Water Treatment, Elsevier (2015), pp. 83-128, https://doi.org/10.1016/B978-1-78242-121-4.00003-4.

[25]   L.L. Coelho, G. Scaratti, A.M. Hissanaga, B.F. Oechsler, H.J. José, R. de F.P.M. Moreira, Modeling and fouling control in a hybrid membrane process using CuO-catalytic membrane coupled to ozone, J. Environ. Chem. Eng. 9 (2021). https://doi.org/10.1016/j.jece.2021.106138.

[26]   A. Moslehyani, M. Mobaraki, T. Matsuura, A.F. Ismail, M.H.D. Othman, M.N.K. Chowdhury, Novel green hybrid processes for oily water photooxidation and purification from merchant ship, Desalination. 391 (2016) 98–104. https://doi.org/10.1016/j.desal.2016.01.003.

[27]   C. Byrne, G. Subramanian, S.C. Pillai, Recent advances in photocatalysis for environmental applications, J. Environ. Chem. Eng. 6 (2018) 3531–3555. https://doi.org/10.1016/j.jece.2017.07.080.

[28]   J. Reszczyńska, T. Grzyb, J.W. Sobczak, W. Lisowski, M. Gazda, B. Ohtani, A. Zaleska, Lanthanide co-doped TiO_2: The effect of metal type and amount on surface properties and photocatalytic activity, Appl. Surf. Sci. 307 (2014) 333–345. https://doi.org/10.1016/j.apsusc.2014.03.199.

[29]   Q. Zhao, M. Wang, H. Yang, D. Shi, Y. Wang, Preparation, characterization and the antimicrobial properties of metal ion-doped TiO_2 nano-powders, Ceram. Int. 44 (2017) 5145–5154. https://doi.org/10.1016/j.ceramint.2017.12.117.

[30]   J. Suave, S.M. Amorim, J. Ângelo, L. Andrade, A. Mendes, R.F.P.M. Moreira, TiO_2/reduced graphene oxide composites for photocatalytic degradation in aqueous and gaseous medium, J. Photochem. Photobiol. A Chem. 348 (2017) 326–336. https://doi.org/10.1016/j.jphotochem.2017.08.064.

[31]   R. Marschall, L. Wang, Non-metal doping of transition metal oxides for visible-light photocatalysis, Catal. Today. 225 (2014) 111–135. https://doi.org/10.1016/j.cattod.2013.10.088.

[32]   N.T. Padmanabhan, H. John, Titanium dioxide based self-cleaning smart surfaces: A short review, J. Environ. Chem. Eng. 8 (2020) 104211. https://doi.org/10.1016/j.jece.2020.104211.

[33]   D. Ma, H. Yi, C. Lai, X. Liu, X. Huo, Z. An, L. Li, Y. Fu, B. Li, M. Zhang, L. Qin, S. Liu, L. Yang, Critical review of advanced oxidation processes in organic wastewater treatment, Chemosphere. 275 (2021) 130104. https://doi.org/10.1016/j.chemosphere.2021.130104.

[34]   X. Yu, Q. Ji, J. Zhang, Z. Nie, H. Yang, Photocatalytic degradation of diesel pollutants in seawater under visible light, Reg. Stud. Mar. Sci. 18 (2018) 139–144. https://doi.org/10.1016/j.rsma.2018.02.006.

[35]   E. Ambrosio, D.L. Lucca, M.H.B. Garcia, M.T.F. de Souza, T.K.F. Thábata, R.P. de Souza, J. V. Visentainer, J.C. Garcia, Optimization of photocatalytic degradation of biodiesel using TiO_2/H_2O_2 by experimental design, Sci. Total Environ. 581–582 (2017) 1–9. https://doi.org/10.1016/j.scitotenv.2016.11.177.

[36] C.S. Ong, W.J. Lau, P.S. Goh, B.C. Ng, A.F. Ismail, Investigation of submerged membrane photocatalytic reactor (sMPR) operating parameters during oily wastewater treatment process, 353 (2014) 48–56. https://doi.org/10.1016/j.desal.2014.09.008.

[37] S. Riaz, S.J. Park, An overview of TiO2-based photocatalytic membrane reactors for water and wastewater treatments, J. Ind. Eng. Chem. 84 (2020) 23–41. https://doi.org/10.1016/j.jiec.2019.12.021.

[38] J.M. Herrmann, Photocatalysis fundamentals revisited to avoid several misconceptions, Appl. Catal. B Environ. 99 (2010) 461–468. https://doi.org/10.1016/j.apcatb.2010.05.012.

[39] R. Vargas, O. Núñez, Photocatalytic degradation of oil industry hydrocarbons models at laboratory and at pilot-plant scale, Sol. Energy. 84 (2010) 345–351. https://doi.org/10.1016/j.solener.2009.12.005.

[40] O.R.S. da Rocha, R.F. Dantas, M.M.M.B. Duarte, M.M.L. Duarte, V.L. da Silva, Oil sludge treatment by photocatalysis applying black and white light, Chem. Eng. J. 157 (2010) 80–85. https://doi.org/10.1016/j.cej.2009.10.050.

[41] N. Yaacob, G.P. Sean, N.A.M. Nazri, A.F. Ismail, M.N. Zainol Abidin, M.N. Subramaniam, Simultaneous oily wastewater adsorption and photodegradation by ZrO_2–TiO_2 heterojunction photocatalysts, J. Water Process Eng. (2020) 101644. https://doi.org/10.1016/j.jwpe.2020.101644.

[42] J. Kang, L. Lu, W. Zhan, B. Li, D. Li, Y. Ren, D. Liu, Photocatalytic pretreatment of oily wastewater from the restaurant by a vacuum ultraviolet/TiO_2 system, J. Hazard. Mater. 186 (2011) 849–854. https://doi.org/10.1016/j.jhazmat.2010.11.075.

[43] O. Iglesias, M.J. Rivero, A.M. Urtiaga, I. Ortiz, Membrane-based photocatalytic systems for process intensification, Chem. Eng. J. 305 (2016) 136–148. https://doi.org/10.1016/j.cej.2016.01.047.

[44] C. Li, Z. Lu, X. Ao, W. Sun, X. Huang, Degradation kinetics and removal efficiencies of pharmaceuticals by photocatalytic ceramic membranes using ultraviolet light-emitting diodes, Chem. Eng. J. 427 (2022) 130828. https://doi.org/10.1016/j.cej.2021.130828

[45]   X. Hu, Y. Yu, J. Zhou, Y. Wang, J. Liang, X. Zhang, Q. Chang, L. Song, The improved oil/water separation performance of graphene oxide modified Al_2O_3 microfiltration membrane, J. Memb. Sci. 476 (2015) 200–204. https://doi.org/10.1016/j.memsci.2014.11.043.

[46]   Q. Chang, J. Zhou, Y. Wang, J. Liang, X. Zhang, S. Cerneaux, X. Wang, Z. Zhu, Y. Dong, Application of ceramic micro filtration membrane modified by nano-TiO_2 coating in separation of a stable oil-in-water emulsion, J. Memb. Sci. 456 (2014) 128–133. https://doi.org/10.1016/j.memsci.2014.01.029.

[47]   D. Lu, W. Cheng, T. Zhang, X. Lu, Q. Liu, J. Jiang, J. Ma, Hydrophilic Fe2O3 dynamic membrane mitigating fouling of support ceramic membrane in ultrafiltration of oil/water emulsion, Sep. Purif. Technol. 165 (2016) 1–9. https://doi.org/10.1016/j.seppur.2016.03.034.

[48]   J.E. Zhou, Q. Chang, Y. Wang, J. Wang, G. Meng, Separation of stable oil-water emulsion by the hydrophilic nano-sized ZrO_2 modified Al_2O_3 microfiltration membrane, Sep. Purif. Technol. 75 (2010) 243–248. https://doi.org/10.1016/j.seppur.2010.08.008.

[49]   X.S. Yi, S.L. Yu, W.X. Shi, N. Sun, L.M. Jin, S. Wang, B. Zhang, C. Ma, L.P. Sun, The influence of important factors on ultrafiltration of oil/water emulsion using PVDF membrane modified by nano-sized TiO_2/Al_2O_3, Desalination. 281 (2011) 179–184. https://doi.org/10.1016/j.desal.2011.07.056

[50]   P. Monash, G. Pugazhenthi, Effect of TiO_2 addition on the fabrication of ceramic membrane supports: A study on the separation of oil droplets and bovine serum albumin (BSA) from its solution, Desalination. 279 (2011) 104–114. https://doi.org/10.1016/j.desal.2011.05.065.

[51]   N.C. Fontão, L.N. Ferrari, J.C. Sapatieri, K. Rezwan, M. Wilhelm, Influence of the Temperature and TiO_2-Incorporation on the Properties of SiOC/SiC Composites for Efficient Wastewater Treatment Applications, Membranes. 12 (2022) 175. https://doi.org/10.3390/membranes12020175.

[52]   M. Ezazi, B. Shrestha, S. Kim, B. Jeong, J. Gorney, K. Hutchison, D.H. Lee, G. Kwon, Selective Wettability Membrane for Continuous Oil−Water Separation and In Situ Visible

Light-Driven Photocatalytic Purification of Water, Glob. Challenges. 4 (2020) 2000009. https://doi.org/10.1002/gch2.202000009.

[53] Y. Shi, J. Huang, G. Zeng, W. Cheng, J. Hu, L. Shi, K. Yi, Evaluation of self-cleaning performance of the modified g-C_3N_4 and GO based PVDF membrane toward oil-in-water separation under visible-light, Chemosphere. 230 (2019) 40–50. https://doi.org/10.1016/j.chemosphere.2019.05.061.

[54] L. Zhang, Y. He, P. Luo, L. Ma, S. Li, Y. Nie, F. Zhong, Y. Wang, L. Chen, Photocatalytic GO/M88A "interceptor plate" assembled nanofibrous membrane with photo-Fenton self-cleaning performance for oil/water emulsion separation, Chem. Eng. J. 427 (2022). https://doi.org/10.1016/j.cej.2021.130948.

[55] W. Cao, W. Ma, T. Lu, Z. Jiang, R. Xiong, C. Huang, Multifunctional nanofibrous membranes with sunlight-driven self-cleaning performance for complex oily wastewater remediation, J. Colloid Interface Sci. 608 (2022) 164–174. https://doi.org/10.1016/j.jcis.2021.09.194.

[56] F. Li, W. Kong, X. Zhao, Y. Pan, Multifunctional TiO_2-Based Superoleophobic/Superhydrophilic Coating for Oil-Water Separation and Oil Purification, ACS Appl. Mater. Interfaces. 12 (2020) 18074–18083. https://doi.org/10.1021/acsami.9b22625.

[57] W. Zheng, J. Huang, S. Li, M. Ge, L. Teng, Z. Chen, Y. Lai, Advanced Materials with Special Wettability toward Intelligent Oily Wastewater Remediation, ACS Appl. Mater. Interfaces. 13 (2021) 67–87. https://doi.org/10.1021/acsami.0c18794.

[58] H. Li, J. Zhang, L. Zhu, H. Liu, S. Yu, J. Xue, X. Zhu, Q. Xue, Reusable membrane with multifunctional skin layer for effective removal of insoluble emulsified oils and soluble dyes, J. Hazard. Mater. 415 (2021) 125677. https://doi.org/10.1016/j.jhazmat.2021.125677.

[59] N.H. Alias, J. Jaafar, S. Samitsu, T. Matsuura, A.F. Ismail, M.H.D. Othman, M.A. Rahman, N.H. Othman, N. Abdullah, S.H. Paiman, N. Yusof, F. Aziz, Photocatalytic nanofiber-coated alumina hollow fiber membranes for highly efficient oilfield produced water treatment, Chem. Eng. J. 360 (2019) 1437–1446. https://doi.org/10.1016/j.cej.2018.10.217.

[60] S.H. Paiman, M.A. Rahman, T. Uchikoshi, N.A.H.M. Nordin, N.H. Alias, N. Abdullah, K.H. Abas, M.H.D. Othman, J. Jaafar, A.F. Ismail. In situ growth of α-Fe_2O_3 on Al_2O_3/YSZ hollow fiber membrane for oily wastewater. Sep. Purif. Technol., 236 (2020). https://doi.org/10.1016/j.seppur.2019.116250.

[61] R.Y. Yue, J. Guan, C.M. Zhang, P.C. Yuan, L.N. Liu, M. Zaheer Afzal, S.G. Wang, X.F. Sun, Photoinduced superwetting membranes for separation of oil-in-water emulsions, Sep. Purif. Technol. 241 (2020) 116536. https://doi.org/10.1016/j.seppur.2020.116536.

[62] M.I. Mohamad Esham, A.L. Ahmad, M.H. Dzarfan Othman, Fabrication, optimization, and performance of a TiO_2 coated bentonite membrane for produced water treatment: Effect of grafting time, Membranes (Basel). 11 (2021). https://doi.org/10.3390/membranes11100739.

[63] Q. Chen, Z. Yu, F. Li, Y. Yang, Y. Pan, Y. Peng, X. Yang, G. Zeng, A novel photocatalytic membrane decorated with RGO-Ag-TiO2 for dye degradation and oil–water emulsion separation, J. Chem. Technol. Biotechnol. 93 (2018) 761–775. https://doi.org/10.1002/jctb.5426.

[64] Y. Zhang, W. Xue, J. Liu, J. Yang, H. Song, X. Zhu, 2D/2D Covalent triazine-based heterostructure membrane for highly enhanced photoactivity and anti-fouling ability, Chem. Eng. J. 424 (2021) 129829. https://doi.org/10.1016/j.cej.2021.129829.

[65] E.N. Santos, Á. Ágoston, S. Kertész, C. Hodúr, Z. László, Z. Pap, Z. Kása, T. Alapi, S.A.G. Krishnan, G. Arthanareeswaran, K. Hernadi, G. Veréb, Investigation of the applicability of TiO_2, $BiVO_4$, and WO_3 nanomaterials for advanced photocatalytic membranes used for oil-in-water emulsion separation, Asia-Pacific J. Chem. Eng. 15 (2020) 1–15. https://doi.org/10.1002/apj.2549.

3 TAILORING ASYMMETRIC ALUMINA MEMBRANES BY COMBINING TAPE CASTING AND PHASE INVERSION

This chapter refers to the study of developing alumina membranes suitable for microfiltration in a single sintering step by combining tape casting and phase inversion. The experimental procedure presented in this chapter was carried out during the sandwich doctorate at the University of Bremen (Bremen, Germany), with exception of X-ray microtomography acquisitions which were performed at the Federal University of Santa Catarina. This study meets the specific objectives described in Section 1.1.2 - Chapter 3.

The complete work carried out in this chapter is presented below in article format, as published in the Journal of Membrane Science (2021) (https://doi.org/10.1016/j.memsci.2021.119056).

3.1 INTRODUCTION

Membrane separation processes appeared in the eighteenth century as an alternative method to conventional processes for wastewater treatment. Since the 1960s, membrane separation has become a significant technology, which is currently applied in different fields, which include pharmaceuticals, food, cosmetics, chemical, and petrochemical industry [1–3].

Various materials have been used to fabricate ceramic membranes including alumina (Al_2O_3) [4], zirconia (ZrO_2) [5], titania (TiO_2) [6] Shirasu porous glass (SPG) [7], and silicon carbide (SiC) [8]. Although the development of ceramic membranes is relatively recent, these membranes present several superior characteristics to polymeric membranes concerning selectivity, permeability, durability, as well as thermal, chemical, and fouling resistance. These properties lead to lower maintenance and replacement requirements, cutting down long-term operating costs. They are of special interest in effluents with a high concentration of organic matter and for processes that require operation at high temperatures and harsh environments [3,9].

Porous membranes may be symmetric or asymmetric, i.e., display uniform or non-uniform morphology throughout the membrane cross-section. Asymmetric membranes have a denser top layer, also called skin. This skin layer can be completely dense or less porous than the support and plays the role of the separation membrane itself. Therefore, asymmetric

membranes are related to higher permeation flux, since the effective membrane thickness can be very thin, while a bottom layer or support enables a lower flux resistance [2,10,11].

Microfiltration (MF) membranes, with a pore range between 0.1 and 5 μm [12], are usually asymmetric. To fabricate them, additional steps at high temperatures are required to combine different layers with graded porosity [3,11]. Despite the aforementioned advantages, the high material and production costs of ceramic membranes still limit their widespread application [2,10,11]. In this regard, phase inversion presents an important advantage as it allows the manufacture of asymmetric membranes in a single sintering step. The formation of different substructures is expected: a more porous intermediary layer, which can be composed of finger-like pores with reduced flow resistance, sandwiched between two denser sponge-like layers and a very thin skin layer. The obtained structure and membrane properties, however, depend on the choice of system components and process parameters [9,11,13].

Phase inversion is commonly used to produce polymeric membranes, but it has been recently adapted to produce ceramic membranes as well [14–16]. Briefly, a homogenous suspension containing ceramic particles dispersed in an organic solvent with polymer binder and additives is initially prepared. Then, the suspension is cast in the desired shape and immersed in a non-solvent bath (usually water), where phase inversion takes place. During this process, the exchange of solvent and non-solvent occurs, leading to liquid-liquid demixing, which involves a complex thermodynamic mechanism. Mass transfer between the two phases increases the concentration of the organic polymer, which in turn results in the membrane solidification (green body) due to polymer precipitation, and the formation of a porous structure [17]. Last, the green body is dried, thermally treated to remove all organics, and then sintered [18,19].

Although the one-step process of phase-inversion has been proven to be an efficient fabrication technique for polymer membranes, the use of this method for the production of ceramic membranes is not yet completely understood. It would allow the production of ceramic membranes with better performance, simple manufacturing, and lower energy consumption, enhancing the economic viability of their application in wastewater treatment [3,11,15,20–22].

Zhu et al. [23] compared porous tubular alumina membranes manufactured by cold pressing and by phase-inversion casting. In the latter, higher porosity, larger average pore size (APS), and lower but acceptable mechanical strength were obtained. Most research on ceramic membranes made by phase inversion is focusing on the development of hollow fibers

[20,24,25]. Few studies have explored the phase-inversion combined with tape casting for ceramic membranes. In those cases, ceramic membranes have been applied mostly in distillation [19,26,27] or as oxygen separation membranes with a gas-tight top layer [13,28,29]. More recently, Nishihora et al. [15] and Yu et al. [22] have shown that phase inversion combined with tape casting could successfully produce flat membranes suitable for microfiltration.

Nevertheless, further studies on this type of ceramic membrane are still needed before it can be used on a larger scale [30]. A better understanding of how to tailor the membrane properties through processing parameters is mandatory. Thus, the present work aims to help fill this gap. Here, flat-sheet ceramic membranes are produced with different slurry compositions (solid and binder loadings) and production parameters (mixing time, sintering temperature, and cast strategy), and their respective effects on the resulting membrane properties are investigated.

3.2   EXPERIMENTAL

3.2.1   Materials

All reagents used were of analytical grade. Alpha-alumina (Almatis, CT3000, d50 ~ 0.4 μm) and graphite powder (Graphit Kropfmühl AG, SGB, 23 LC/99.9, d50 ~ 23 μm) were used to produce either alumina or graphite slurries. N-methyl-2-pyrrolidone (NMP, Sigma), polyethersulfone (PES, BASF Ultrason® E2010), and poly(ethylene glycol) (PEG, Sigma, BioUltra 35000) were used as a solvent, binder, and plasticizer, respectively. PES pellets were dried at 70 °C for 24 h before use to avoid interferences on solution miscibility at this point. Ultrapure water (Milli-Q system, Millipore) was chosen as a non-solvent for the coagulation bath.

3.2.2   Preparation of flat alumina membranes

Alumina membranes were shaped from slurries with different compositions using the procedure represented in Fig. 3.1. First, PES (5.5, 6.2, or 7.0 wt%) and PEG (0.8 wt%) were completely dissolved in suitable amounts of NMP, calculated as follows: wt% NMP = 100 wt% - wt% PES - wt% PEG - wt% alumina (to be added). The solution was stirred at 60 °C for
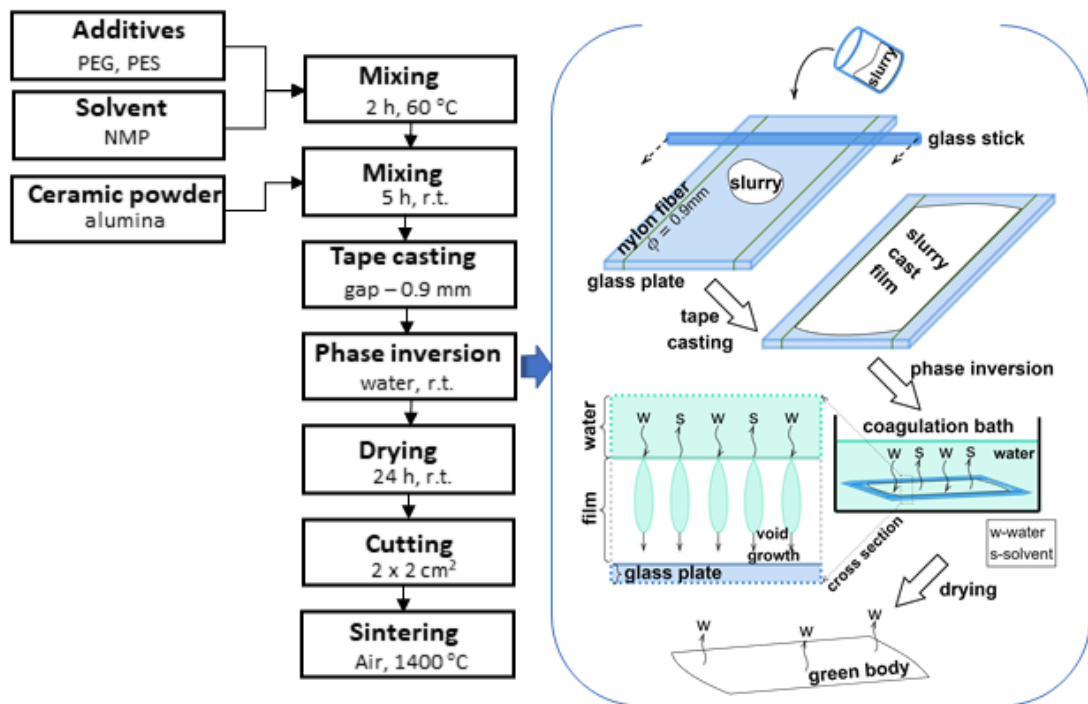
Figure 3.1 Schematic diagram for the preparation of membranes.

homogenization. Next, alumina powder (35, 40, 45, or 50 wt%) was added and mixed for further 5 h at room temperature. The slurry was then cast with a glass rod onto a glass plate equipped with two nylon fibers (diameter = 0.9 mm) to set the thickness (Fig. 3.1). The glass plate was immediately immersed in water at room temperature to initiate solidification by phase-inversion, leading to the formation of the green tape. After 12 h, the green tapes were removed from the water bath and left to dry for at least 24 h at room temperature, then cut into pieces of 2 cm x 2 cm. Thermal treatment was carried out in an electric resistance furnace in air atmosphere. The green tapes were debound at 2 °C min^{-1} from room temperature to 600 °C. After a dwell time of 2 h, the green tapes were sintered at 2 °C min^{-1} to 1400 °C and kept at the final temperature for 3 h. The membranes were cooled in the furnace down to room temperature.

Based on the research work of Chen's group [26,28,29,31], a co-casting strategy was also used for some membranes to reduce the flux resistance caused by a dense layer usually formed on the bottom part of ceramic membranes produced by phase-inversion. Briefly, a slurry containing graphite instead of ceramic powder is produced and a very thin graphite-containing layer is cast underneath a simultaneously cast ceramic layer (Fig. 3.2). The dense bottom layer

formed during phase inversion contains graphite, which can be burned off before sintering. The resulting membranes support should show an improved porosity and, consequently, a higher permeability. In this work, a homemade doctor blade with two knives (Fig. 3.2) was used, allowing the preparation of a thin layer of the graphite slurry (0.15 mm) under an alumina slurry layer of 0.90 mm. The graphite slurry (11.4 wt% PES, 1.6 wt% PEG, and 30.0 wt% graphite powder) was produced in the same way as the alumina slurries.

Additionally, modified membranes were produced for some slurry compositions by increasing the stirring time of the slurry from 5 to 24 h or increasing the final sintering temperature to 1500 °C. All membranes produced are listed in detail in Table 3.1. They were denoted as Ax-Py, where x indicates wt.% alumina in the slurries, while y indicates wt% PES added. For example, sample A35-P7 contains 35 wt% alumina and 7 wt% PES. When not indicated, the slurries were stirred for 5 h and heat-treated at 1400 °C. When different conditions were investigated, the time of mixing or final sintering temperatures were added to the specimen denotation. For instance, a sample mixed for 24 h or sintered at 1500 °C was denoted as A35-P7-24h or A35-P7-1500 respectively. In turn, the samples denoted G-A45-P7 and G-A50-6.5 were produced with graphite co-cast membranes.
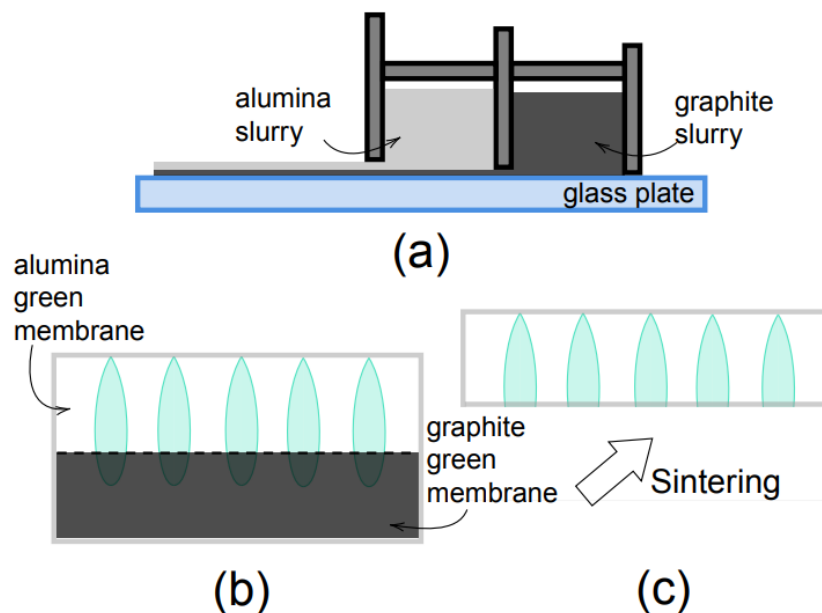
Figure 3.2 Scheme of the preparation of co-cast membranes.

Table 3.1 Ceramic slurries composition.

Sample	Al₂O₃ (wt%)	PES (wt%)	PEG (wt%)	Mixing time (h)	T (°C)
A35-P7	35	7.0	0.8	5	1400
A40-P7	40	7.0	0.8	5	1400
A45-P7	45	7.0	0.8	5	1400
A50-P7	50	7.0	0.8	5	1400
A45-P6.2	45	6.2	0.8	5	1400
A50-P6.2	50	6.2	0.8	5	1400
A50-P5.5	50	5.5	0.8	5	1400
A45-P7-24h	45	7.0	0.8	24	1400
A50-P7-24h	50	7.0	0.8	24	1400
A45-P6.2-1500	45	6.2	0.8	5	1500
A50-P5.5-1500	50	5.5	0.8	5	1500
G-A45-P7	45	7.0	0.8	5	1400
G-A50-P6.2	50	6.2	0.8	5	1400

3.2.3 Membrane characterization

3.2.3.1 Morphology

The macrostructure of the cross-section and surface of the membrane was analyzed by Scanning Electron Microscopy (SEM, 20 kV; Series 2, Obducat CamScan; Supra 40-Carl Zeiss). Before the measurement, samples were sputtered with gold (K550, Emitech, Judges Scientific). X-ray microtomography acquisitions (micro-CT scanner Zeiss XRM Versa-500) were used to assess membrane morphology in different plans. To determine the APS on the top surfaces of the sintered membranes, SEM images (5000x magnification) were analyzed using a dedicated software (ImageJ). One-way ANOVA followed by Tukey post hoc test was used to analyze if the APS were different at 0.05 level. Bulk pore size distribution and porosity were obtained by mercury intrusion porosimetry (Pascal 140/440, Porotec). Bubble-point pressure was determined using a homemade permeation setup for two different membranes. Before the analysis, membranes were sonicated in deionized water for 30 min and let immersed for 24 h. The sizes of through pores were calculated from Wardbush Equation (Equation 1), where d is

the through pore diameter (m), P is the bubble-point pressure (Pa), γ is the water surface tension (0,073 N m^{-1} at 20 °C), S (0.715) is the shape factor commonly employed when analyzing membrane filters, and φ is the contact angle between water and surface, commonly considered zero for ceramic hydrophilic membranes such as alumina ones.

$$d = \frac{4\gamma S.\, cos\varphi}{P} \qquad (1)$$

3.2.3.2 Flexural Strength

The maximum flexural strength of the membranes was obtained by three-point bending tests (Roell Z005, Zwick). A 5 kN load cell (piezoelectric force sensor) was used; the crosshead speed and pre-load were fixed at 0.1 mm min^{-1} and 0.25 N, respectively. Before the tests, the sintered samples were cut into pieces of ~16 mm length and ~2 mm thickness using a diamond wire cutting machine.

3.2.3.3 Water permeation flux

The water permeation was measured in a dead-end filtration cell applying pressures of 0.5, 1, 2, and 3 bar. The membranes were cut in circles of 1 cm diameter (effective area of filtration was 0.785 cm^2). The water flux J (m^3 m^{-2} h^{-1}) was calculated according to Equation 1, where V (m^3) is the permeated volume in a period t (h) through a membrane surface area A (m^2).

$$J = \frac{1}{A} \cdot \frac{dV}{dt} \qquad (2)$$

3.2.3.4   *Permeability simulation*

Micro-CT technique provides morphological information, through 3D and 2D images, that enables one to evaluate the microstructure of samples. [32] This technique was used to assess the variability of the pore morphology throughout two membranes (A45-P7 and A50-P6.2) and its influence on permeability. The micro-CT images were processed with Avizo software (version 8.1/ThermoFisher Scientific), and the intrinsic permeability (Darcian permeability) was numerically simulated in a 3D pore network extracted from the 3D binary image of the membranes [33, 34]. The implemented computational code of Avizo follows the principles of the Maximum Balls technique [35, 36, 37] that consists of a simplification of voxel-based binary images into a network of objects with well-known morphology, in most cases spheres and cylinders, depicting pores and connections, respectively. Both the connectivity and the phase fraction of the original image are kept in the network. The intrinsic permeability is obtained simulating a single-phase fluid flowing viscously through the network via an imposed pressure drop across one single direction, following Darcy's law. The hydraulic resistance of pores and connections is calculated based on the Hagen–Poiseuille law and its geometry. For every single pore network, the mass conservation is applied resulting in a linear system of equations whose solution determines the pressure for the pores of the network. Now, the flow rate in the network can be calculated as well, using Darcy law, the intrinsic permeability.

The permeability was simulated for the three orthogonal directions of the images [32]. The obtained results in the three axes can be interpreted as an indicator of the porous media's degree of anisotropy [38]. Nevertheless, the direction performed in the water permeation test (from the skin layer on the top to the bottom layer: axis z) is the more relevant simulation for the membranes. Two sets of simulations were performed, taking into account two different regions.

3.3   RESULTS AND DISCUSSION

3.3.1 Morphology

The SEM images of the cross-section of different membranes (Fig. 3.3) show typical asymmetric morphologies for ceramic membranes produced by phase inversion.
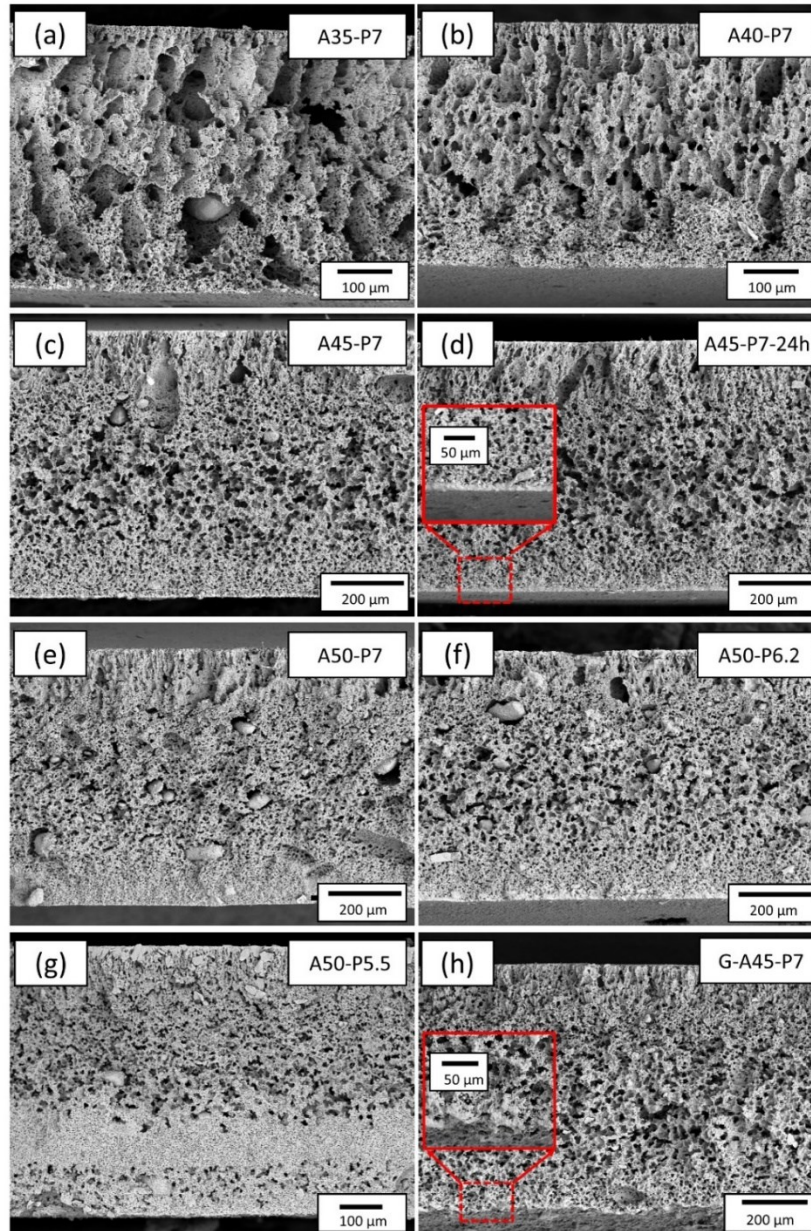
Figure 3.3 SEM images of the cross-section of membranes (a) A35-P7; (b) A40-P7; (c) A45-P7; (d) A45-P7-24h; (e) A50-P7. (f) A50-P6.2; (g) A50-P5.5; (h) G-A45-P7.

As expected, a skin layer was formed on the top surface of the membrane, and, for all non-co-cast membranes (Fig. 3.3a-g), a sponge-like layer was formed at the bottom. The

intermediary layers exhibited regions with high porosity and different features, as observed in Micro-CT images for different 2D sections (Fig. S1). The mechanisms behind pore-forming during phase inversion are not well understood yet. Nevertheless, Kingsbury and Li [16] as well as Wang and Lai [17] have proposed that the phenomenon known as viscous-fingering is important in the formation of finger-like voids during phase inversion. The phenomenon occurs at the interface between fluids with different viscosities, when a less viscous fluid replaces a more viscous one, as is the case with a non-solvent/ceramic suspension system, which occurs during phase inversion processes and form complex patterns. Concentration gradient results in solvent/non-solvent exchange. The phenomenon occurs in the first moments of mixing and is followed by polymer phase precipitation, solidifying the green body resulting in the viscous-fingering shape [9,11].

The effect of varying the alumina loading from 35 to 50 wt% is shown in Fig. 3.3a-d. For 35 and 40 wt% alumina (Fig. 3.3a and Fig. 3.3b), finger-like mixed with sponge-like pores can be seen in almost the entire thickness of the intermediary section. When alumina loading was further increased to 45 and 50 wt% (Fig. 3.3c and Fig. 3.3e), an expressive change of the morphology was observed. The finger-like section was slightly reduced near the skin layer, and the remaining extension of the intermediary layer was replaced by sponge-like pores. The resulting intermediary layer, in turn, also has an asymmetrical structure, with larger pores remaining in the middle of the cross-section, which gradually becomes smaller towards both surfaces. The transition from finger to sponge-like pores can be attributed to a significant enhancement in the suspension viscosity when alumina loading is increased (Fig. S2). Slurry viscosities have been demonstrated to play important role in ceramic support for structure formation [21]. When a viscosity threshold is achieved for a certain slurry, finger-like pores are no longer capable to be formed during phase inversion. This threshold is also called critical viscosity value and it is related to the complex viscous-fingering phenomenon [16,17,21]. Furthermore, irrespective of pore shape, the macropore diameters decreased, as expected, with increasing solid loading. The magnification of Fig. 3.3d shows that the bottom layer of the membrane is already very dense with 45 wt% alumina.

One of the main roles of polymers in the phase inversion process to produce ceramic membranes is to immobilize the ceramic particles when polymer precipitation takes place [16]. During sintering, the polymer acting as a template is burned off and ceramic particles can sinter keeping the same microstructure as the green tape [22]. Varying loads of PES from 7.0 to

6.2 wt.% (membranes A50-P7 and A50-P6.2, respectively) led to a visibly more porous intermediary layer (Fig. 3.3e-f). The alumina/PES ratio for the aforementioned membranes increased from 7.1 to 8.1. Although PES is eliminated during sintering and both slurries have the same ceramic loading, this variation may have led to a lack of polymer to hold all the ceramic particles during phase inversion. Consequently, they tend to disperse into the coagulant bath, which was observed during preparation, instead of remaining in the green tape to be sintered [39].

For membranes produced from slurries containing 45 wt% alumina, a slightly more porous intermediate area with decreasing PES load was observed (Fig. 3.3c and Fig. S3, respectively). Further decrease in PES loading (5.5 wt%) for the membrane containing 50 wt% alumina (Fig. 3.3g) and an alumina/PES ratio = 9.1 resulted in the formation of a thick dense layer in the middle of the cross-section. Again, this result can be attributed to the lack of binder, which causes the expected structure to fall apart during the process. It is worth noting that no changes in the extension of the finger-like pores were observed in these membranes, as the variation in the amount of PES has only a minor influence on the suspension viscosity compared to the effect of the ceramic loading (Fig. S2)

Both higher porosity of the intermediary layer and the finger or sponge-like pores can be desired or undesired characteristics, depending on the other membrane characteristics and the application. Although the presence of macropores may decrease flux resistance, it can reduce the mechanical resistance of the membrane [17].

The membranes were produced with a reduced mixing time of 5 h compared to most of the membranes described in the literature, where times up to 48 h are considered [22]. The microstructure found for a membrane prepared with an increased mixing time of 24 h (Fig. 3.3d) presented the same profile as for the membrane prepared with 5 h mixing (Fig. 3.3d). Nevertheless, some irregular large aggregates were observed when the suspensions were mixed for 5 h (Fig. 3.3c-e), possibly due to the insufficient dispersion of the alumina powder during slurry preparation. No significant changes in the microstructure were observed when the sintering temperature was shifted from 1400 to 1500 °C. Finally, the dense bottom surface (detail in Fig. 3.3d) observed for all the membranes produced by one-layer tape casting (detail in Fig. 3.3d) was successfully removed by graphite co-casting (Fig. 3.3h).

The APS for the top layer of the membrane was calculated from digital image analysis, while the APS of the entire membrane was obtained from Hg intrusion porosimetry

measurements (Table 3.2). Differences between values derived from both techniques are due to membrane anisotropy.

Table 3.2 Average pore size (APS), porosity, and flexural strength of the membranes.

Sample	APS from image processing D (µm) *	APS from Hg porosimetry D (µm)	Porosity (%)	Maximum flexural strength (MPa)	
A35-P7	0.37^{ab}	21.52	72.46	n.m.**	
A40-P7	0.35^{ab}	19.96	71.55	17.67	$\pm$ 5.33
A45-P7	0.42^{a}	8.45	75.15	27.60	$\pm$ 5.34
A50-P7	0.32^{b}	13.18	69.22	28.28	$\pm$ 2.97
A45-P6.2	0.32^{b}	20.03	64.64	24.51	$\pm$ 4.15
A50-P6.2	0.32^{b}	10.48	69.11	41.11	$\pm$ 7.02
A50-P5.5	0.33^{b}	6.82	62.74	35.17	$\pm$ 8.22
A45-P6.2-1500	0.34	16.63	63.43	29.65	$\pm$ 6.17
A50-P5.5-1500	0.38	7.53	45.97	36.03	$\pm$ 9.57
A45-P7-24h	0.38	8.73	53.32	32.86	$\pm$3.33
A50-P7-24h	0.30	12.24	68.93	31.17	$\pm$ 4.37
G-A45-P7	0.32	9.05	72.97	24.84	$\pm$ 6.38
G-A50-P6.2	0.42	8.70	63.03	38.37	$\pm$ 5.37

* Values distributed with different superscript letters (a, b) indicate significant differences (one-way ANOVA with Tukey's post hoc test, $p < 0.05$). ** n.m. = not measured because the membrane was too fragile.

Despite the strong influence of suspension composition on the cross-section morphology of the membrane, no similar influence was found on pore sizes of the membrane top surface (Fig. 3.4a-f and 4i). According to image analysis, the APS of the skin layer is in a range of 0.30-0.42 µm for all membranes, regardless of the process parameters and solid loadings for the tested range. The number of pores accounted for in the calculation and the resulting pore distribution (box-plot) for the different membranes are shown in Table S1 and Fig. S4, respectively. Among the membranes produced under standard conditions, APS is not

considered different at 0.05 level, with exception of A45-P7. Nevertheless, the APS of A45-P7 was not significantly different from the values of A35P7 and A40-P7.
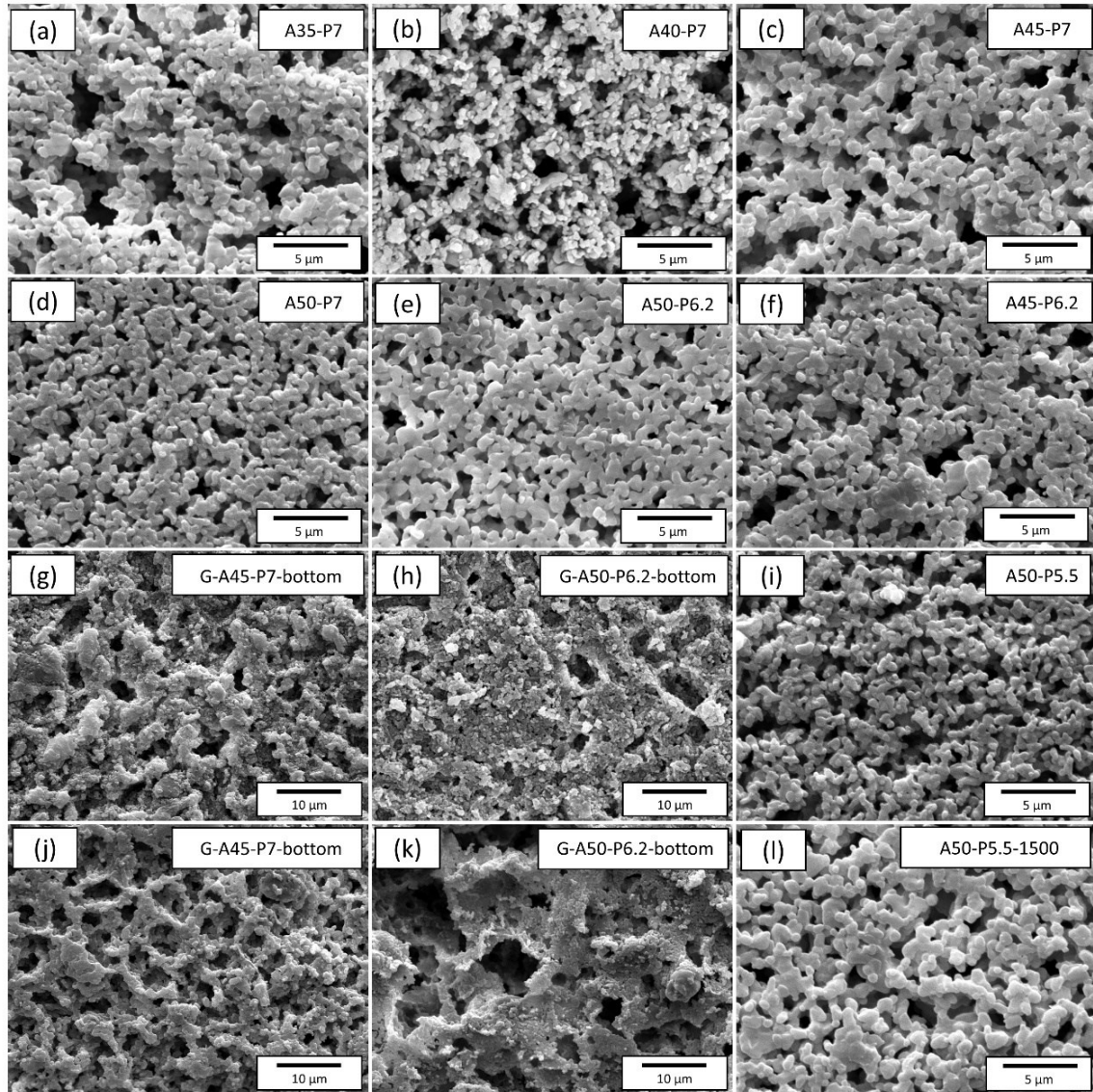
Figure 3.4 SEM images of membrane surfaces. (a) A35-P7; (b) A40-P7; (c) A45-P7; (d) A50-P7; (e) A50-P6.2 (f) A45-P6.2; (g) A45-P7-bottom; (h) A-50-P6.2-bottom; (i) A50-P5.5; (j) GA-45-P7-bottom; (k) G-A50-P6.2-bottom; (l) A50-P5.5-1500.

When the sintering temperature was increased to 1500 °C (Fig. 3.4l), the surface grain boundaries became slightly smoother due to the higher sintering degree [40]. While the APS values found for the membranes sintered at 1500 °C appear to be higher than their counterparts with the same composition sintered at 1400 °C (Table 2), which would be consistent with Cheng

et al., the differences in the Tukey's test were not significant at a level of 0.05. No differences were found for membranes produced with the increased mixing time of 24 h compared to the standard time of 5 h. It should also be noted that no cracks were observed on membrane surfaces.

Fig. 3.4(g-h) shows the bottom surface of the membranes A45-P7 and A50-6.2 respectively, while Fig. 3.4(j-k) shows the co-cast counterparts G-A45-P7 and G-A50-6.2. The latter showed a much more open bottom surface so that the formation of a denser layer could be successfully prevented by the co-cast strategy. While the upper surface plays the role of a selective barrier in a filtration application, the only function of the bottom part is to act as a support structure with low flux resistance and good mechanical strength. If this barrier can be removed without loss of the mechanical strength of the membrane, an optimization of the membrane performance can be expected [29]. Nevertheless, the bottom surface of membrane G-A50-P6.2 (Fig. 3.4k) is quite heterogeneous showing areas with low porosity as well. This fact indicates that this process still needs to be optimized to produce a more homogeneous graphite layer, mainly for more viscous slurries such as the one used for membrane A50-P6.2. Since membrane A50-P6.2 possesses a thicker dense layer in the bottom compared to A45-P6.2, a thicker graphite layer could improve the homogeneity of this surface.

APS of the whole membrane measured by mercury porosimetry was found to be in a range of 6.82-21.52 μm. These results include dead pores, which do not participate in permeation. Nevertheless, Micro-CT analysis (Section 3.3.4 – Permeability simulation) has shown that around 99% of these membranes' porosity was through pores. The largest through pores for A45-P7 and A50-P6.2 membranes were calculated from Equation 2 using the bubble-point technique since it only counts for the through pores. Largest through pores sizes of 13 and 15 μm were obtained for A45-P7 and A50-P6.2. For the same membranes, APS obtained from mercury porosimetry were 8.7 and 10.5 μm respectively.

Comparing these bulk APS to images of membrane cross-sections (Fig. 3.3), the larger pore sizes values of A35-P7 and A40-P7 can be ascribed to finger-like pores, while smaller pore sizes values found for A45-P7 and A50-P7 membranes can be ascribed to sponge-like pores. This change in macrostructure is confirmed by the pore size distribution (Fig. S5). For the membranes sintered at 1500 °C, for which the slurry was mixed for 24 h or co-cast, APS remained approximately unchanged compared to the ones produced with the same composition

under standard conditions. The produced membranes presented high total porosity in a range between 46% and 75% (Table 2).

3.3.2 Flexural strength

The maximum flexural strength (Table 3.2) ranged from 17.7 to 41.1 MPa for all membranes except A35-P45. This membrane was too fragile and could not be tested. Flexural strength values of 22.2 MPa found for alumina flat supports (3 mm thickness, 37.43% porosity, APS = 13.9 µm) have been considered already suitable for the filtration process at the tested transmembrane pressure of 2 bar [41], while flexural strength values up to 58 MPa can be found for different flat ceramic membranes published in the literature (Table 3.3).

While it could be expected that the flexural strength increases when porosity decreases, no clear relation was observed in this study. Nevertheless, this behavior was observed for the relationship between APS and the maximum flexural strength. Additionally, this tendency is observed for membranes produced under standard conditions when Al_2O_3 loading increases and PES loading decreases (Fig. 3.5).
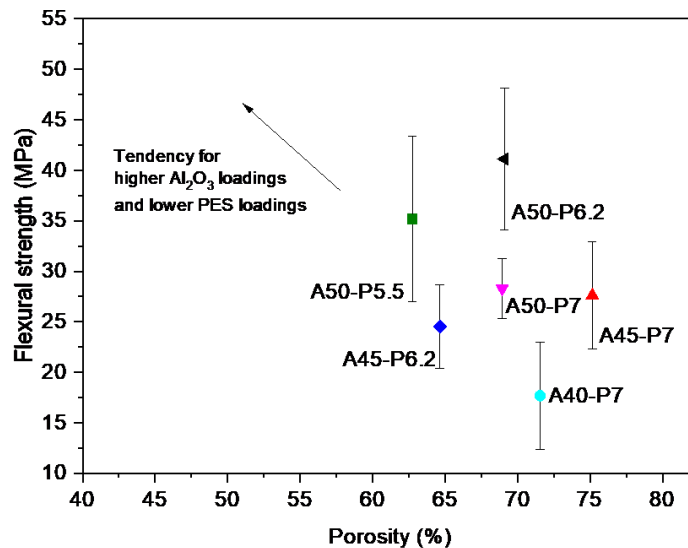
Figure 3.5 Relationship between flexural strength porosity for membranes produced under standard conditions

Table 3.3 Microfiltration planar ceramic membranes properties.

Membrane material	Forming method	Morphology	APS* (μm)	Porosity (%)	Thickness (mm)	Flexural strength (MPa)	Water permeance ($m^3m^{-2}h^{-1}bar^{-1}$)	Reference
Al_2O_3	Tape casting phase inversion	Asymmetric	0.30 – 0.42[a]	46.1 – 75.2	0.7	24.5 – 41.1	13.8 – 108.7	This work
Mullite	Tape casting phase inversion	Asymmetric	1.2[a]	68.3	0.7 – 1	34.7	14.7	[15]
Al_2O_3	Tape casting phase inversion	Asymmetric	0.08 – 0.12[b]	50-80	0.19 – 0.48	-	13 – 41	[22]
TiO_2/Al_2O_3	Plaster mold casting	Symmetric	2.4[c]	42	3	46.2	45.4	[40]
TiO_2/Clay	Uniaxial pressing	Asymmetric	0.9[b]	43.3	5	-	1	[42]
TiO_2/Al_2O_3	Uniaxial pressing	Asymmetric	0.2[a]	28.8	2	58	-	[43]
Al_2O_2/SiO_2/kaolin/mullite	Uniaxial pressing	Symmetric	1.9[a]	58.3	-	-	0.6	[44]
Al_2O_3	Tape casting	Symmetric	0.1 - 0.7[a]	25 - 55	0.3-0.8	-	0.1– 0.9	[45]
SiO_2/Al_2O_3	Tape casting	Asymmetric	0.25[b]	37.4	3	25.1	5	[41]
APTES/YSZ	Aqueous tape casting	Symmetric	1.4[a]	51	0.2	-	0.6	[5]

*Values distributed with different superscript letters were derived from different pore size measurement techniques: [a] surface image processing; [b] N_2 permeation; [c] Hg porosimetry.

Membrane A50-6.7 showed the highest maximum flexural strength (41.1 MPa). A clear increase in strength is observed with increasing alumina loading. The substantial increment of the strength from A40-P7 to A45-P7 is also attributed to the change in macrostructure from finger-like to sponge-like pores. In contrast, no correlation was found for the change in

concentration of PES (Fig. 3.6a). A slight decrease in flexural strength was observed for co-cast membranes (Fig. 3.6b) may be attributed to the removal of the denser bottom layer, since denser layers, in general, improve the mechanical strength. On the other hand, a slight tendency to improve strength was observed when the sintering temperature or mixing time of the slurry was increased (Table 2). This behavior can be attributed to a higher densification degree and slightly more homogenous slurries, respectively.

3.3.3   Water permeation

Pure water fluxes of new asymmetric membranes were analyzed. Fig. 3.7 presents the correlation between water flux at 1 bar and membrane flexural strength. An improvement of the flexural strength tends to result in a loss of permeability. Although it could be expected that this result is related to the porosity, no clear relation was observed in this study, as mentioned in Section 3.3.2. It is more likely that this relationship is related to the asymmetric structure of the membranes. The highest permeability observed for membrane A40-P7 can be attributed to the finger-like pores. However, this membrane presents the lowest flexural strength among the tested set and may not be suitable for microfiltration.

(a)

(b)
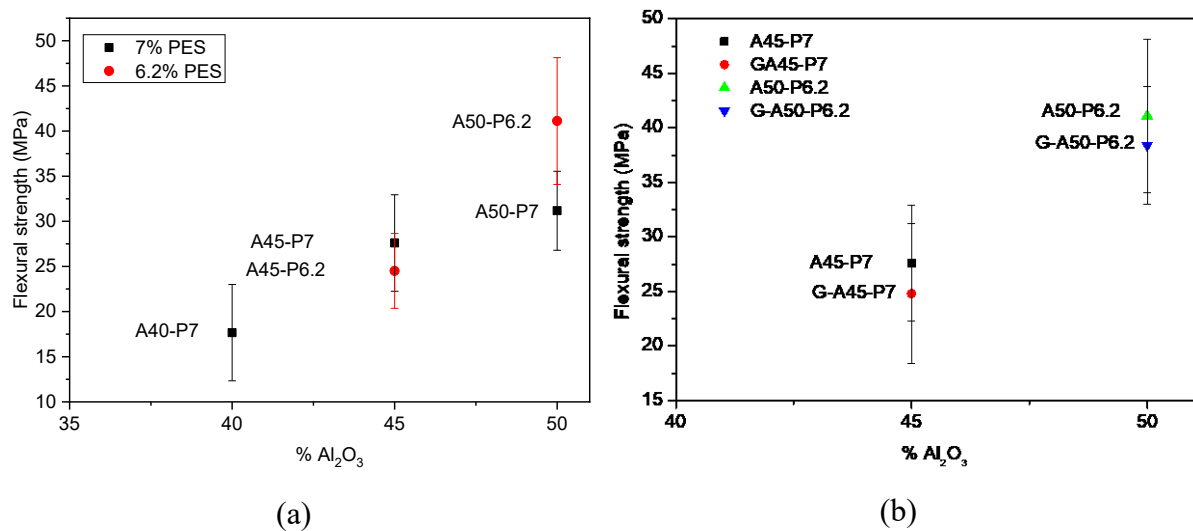
Figure 3.6 Flexural strength of alumina membranes with increasing solids content and (a) different PES loading, and (b) graphite co-cast.
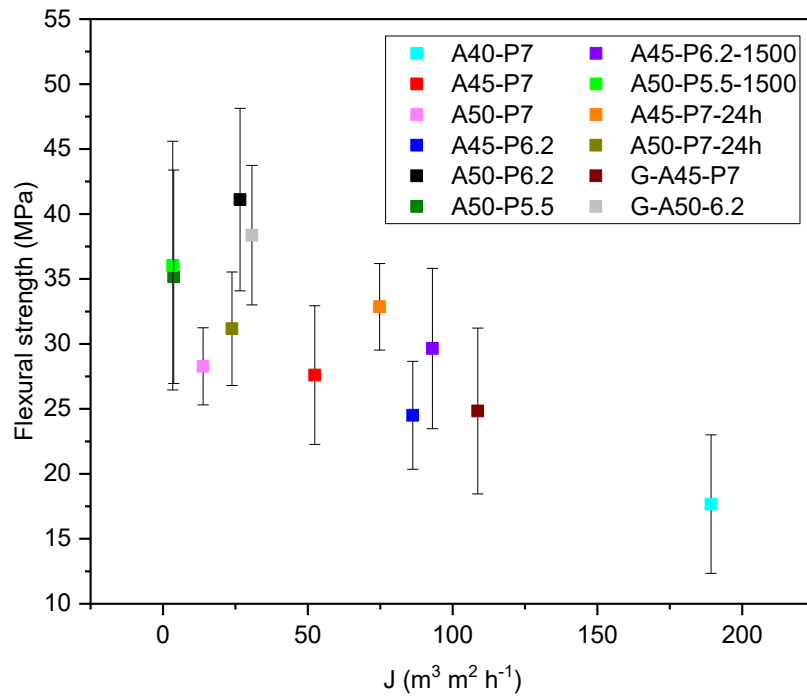
Figure 3.7 Relationship between flexural strength and water permeation flux at 1 bar for membranes produced under standard conditions.

Fig. 3.8 shows pure water fluxes of the membranes at 0.5, 1, 2, and 3 bar as a function of different compositions (Fig. 3.8a), mixing times (Fig. 3.8b), sintering temperatures (Fig. 3.8c), and with and without co-casting (Fig. 3.8d). With increasing alumina loading the flux decreases significantly, while flexural strength was improved. Flux at 3 bar was reduced by 67 and 73% for each increase of alumina load of 5 wt%. Changing the amount of PES from 7 to 6.2 wt% for membranes with 45 and 50 wt% alumina resulted in an increase of the water flux at 3 bar of 72% and 92%, respectively. Nevertheless, all of these membranes show a comparably high flux of pure water. Samples A45-P7 and A50-P6.2 presented fluxes of 52.40 and 26.60 m^3 m^{-2} h^{-1} at 1 bar and maximum flexural strength of 26.60 and 41.11 MPa, respectively. The influence of the resulting morphology on the permeability of A45-P7 and A50-P6.2 membranes is discussed in Section 3.3.4 (Simulated permeability). On the other hand, the lowest flux (3.72 m^3 m^{-2} h^{-1} at 1 bar) was observed for the A50-P5.5 membranes due to the dense layer formed in the intermediary section (Fig. 3.3g) as discussed in Section 3. 3.1, which strongly suppressed the flux.
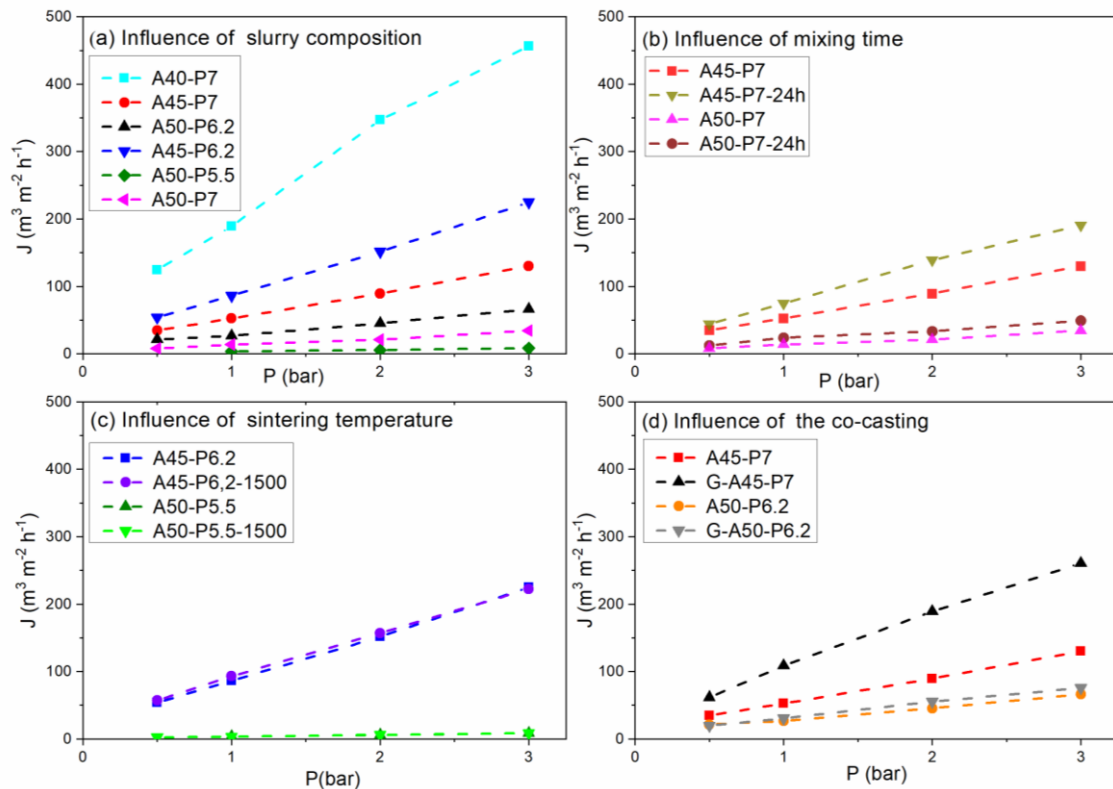
Figure 3.8 Water permeation of membranes produced at different: (a) compositions, (b) mixing times, (c) sintering temperatures, and (d) with and without co-casting.

Increasing the mixing time of the slurry that resulted in more homogeneous slurries, slightly improved the flux (Fig. 3.8b) and no change in flux resulted from the increase in sintering temperature from 1400 to 1500 °C Fig. 3.8c).

Finally, Fig. 3.8d shows the permeation water flux for the co-cast membranes. The influence of co-casting was significantly different for each tested composition. While comparing A45-P7 with the respective co-cast membrane GA45-P7, water flux was improved by 100% at 3 bar, for the membrane pair A50-P6.2 / G-A50-P6.2, the increase of flux was only 15%. As observed in SEM images of the cross-section, the resulting morphology of the bottom side of membrane G-A50-P6.2 was very heterogeneous. Still, co-casting has proven to be an important strategy to further improve the permeability of ceramic membranes produced by phase inversion. In addition, to the best of our knowledge, it is the first time the co-casting strategy was tested for membranes suitable for the microfiltration process.

The membranes A50-P6.2 (APS = 0.32 μm, thickness ~ 0.7 mm, 69.11% porosity, flexural strength = 41.11 MPa) and A45-P7 (APS = 0.42 μm, thickness ~ 0.7 mm, 75.15%

porosity, flexural strength = 27.60 MPa), for example exhibit 19.9 and 38.8 times higher water fluxes at 1 bar than commercial membranes of symmetric alumina hollow fibers (APS = 0.60 μm, outer/inner diameter = 4.8/3 mm, 39% porosity, Deltapore Systems BV). Water fluxes of the A50-P6.2 membranes are also slightly higher than the most permeable asymmetric mullite membrane produced by Nishihora et al. [15] (APS = 1.18± 0.8 μm, 68.27% porosity, flexural strength = 34.6 MPa). High permeabilities of both membranes are attributed to the morphology of the membranes resulting from the phase inversion technique. Further results published in the literature on membrane properties for flat microfiltration ceramic membranes are addressed in Table 3. It is difficult to make straightforward comparisons between membranes with different properties. Differences may be even higher when different pore size measurement techniques were used. Nevertheless, even when comparing membranes whose pore sizes were measured from surface image processing, it can be noted that membranes produced in this work presented elevated water permeances while keeping the same range of thickness, flexural strength, and porosity for all presented membranes.

3.3.4 Permeability simulation

Micro-CT images were acquired for A45-P7 and A50-P6.2 membranes to better investigate the influence of membrane morphology on their permeabilities. Two different sets of simulations of permeability were performed from the skin layer on the top to the bottom layers (axis z). The first one was carried out in four volumes of interest (V1, V2, V3, and V4) taken inside the membranes according to the variation of the pore morphology (Fig. 3.9). The results of the simulations of intrinsic permeability (k) are displayed in terms of Darcy permeability unit D (1 D~$10^{-12}\,m^2$). Only the percolation network is taken into account in these simulations. It can be observed that almost the entire network (99.34%) of the A50-P6.2 sample has percolating pores (only 0.66% are unused pore structures). The same is true for the A45-P7, 98.69% of the pore network accounts for percolating pores, while only 1.31% refers to unused porosity. The simulations results indicate the influence of the intermediary layer morphology on permeability. The differences in intra-membrane permeability in three axes indicate the preferential fluid flow in the z-axis for all the simulated volumes (V1, V2, V3, and V4), indicating the presence of finger-like pores although they are only visually discernible in

V1 (Fig. 3.9). Additionally, V1 presents the highest difference in permeability between z and x or y-axis. Even though in 2D images the pores do not seem to present a preferential path in a certain direction for V2, V3, and V4, the 3D analysis allowed this information to be obtained. This result can be attributed to the main direction of fluids' movement during pore formation in the phase inversion process (z-axis).
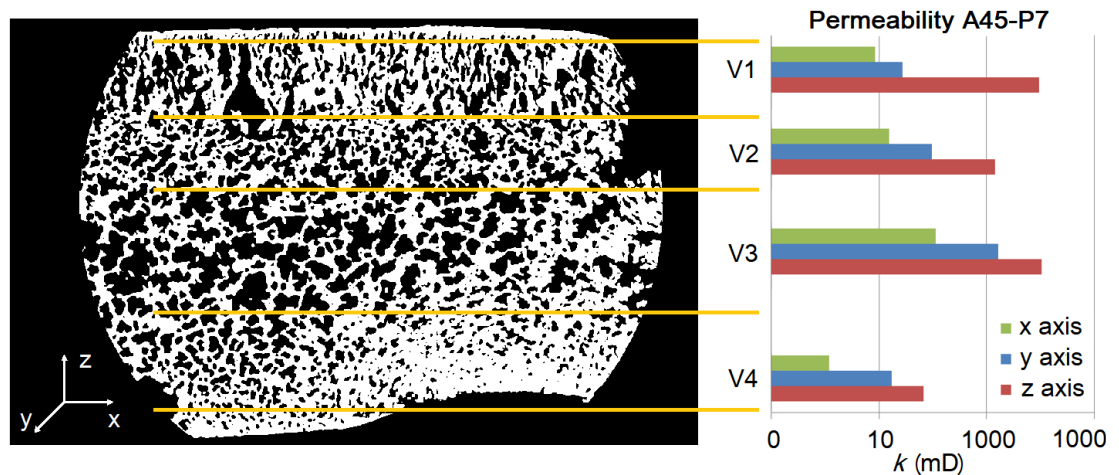
(a)
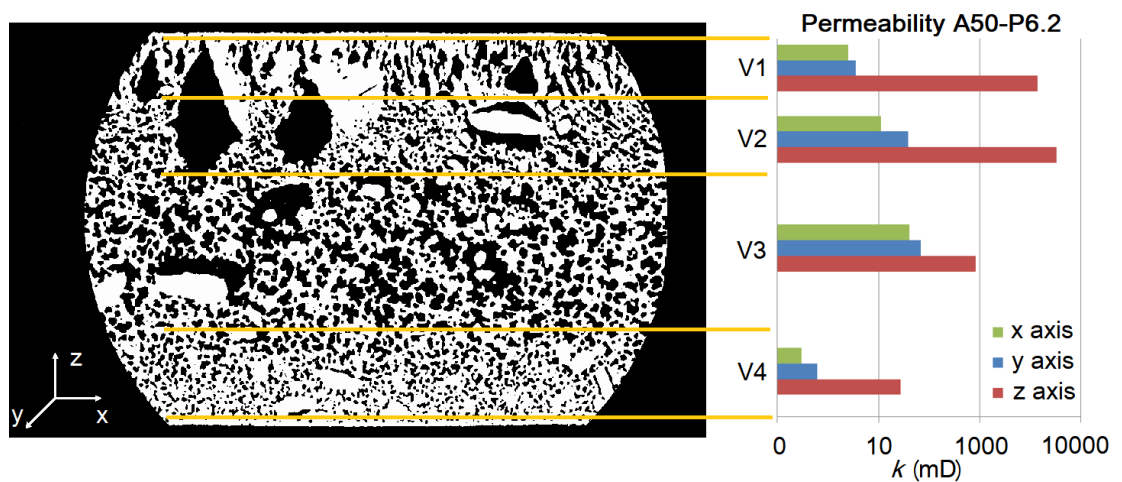
(b)

Figure 3.9 Micro-CT images (left side) and results of the permeability (k) simulations (right side) in different depths (V1, V2, V3, and V4) of z-axis for the membranes (a) A45-P7 and (b) A50-P6.2.

The second set of simulations was also carried in the same direction (z-axis), but the cross-section was divided into three volumes of interest (Fig. 3.10): (i) a volume that enclosed

the whole extension of the membranes (V0: orange); (ii) a thinner volume comprising only the membrane upper layer, including the skin-layer (V0: yellow) and (iii) another thinner volume comprising the lower layer, including the bottom surface (V5: red). It is important to note that, differently from V1 and V4, in this set, top and bottom surfaces are included. The simulation results in terms of permeability k for the z-axis can be found in Table 3.4.
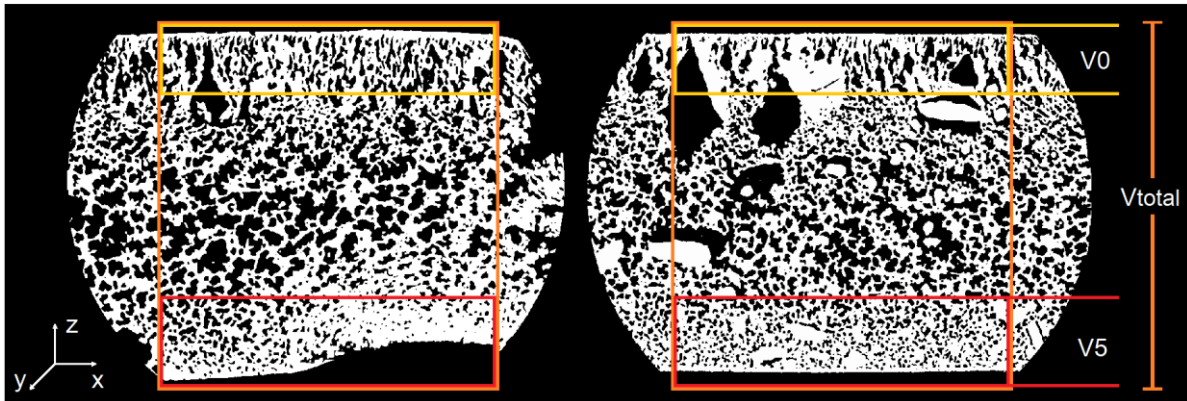
Figure 3.10 Delimitations of the volumes used in permeability simulations of the membranes A45-P7 (left) and A50-P6.2 (right).

Table 3.4 Permeability simulations results.

	Permeability (mD) – z-axis						
Sample	**V_{total}**	**V0**	**V5**	**V1**	**V2**	**V3**	**V4**
A45-P7	5.37	12.37	1.21	9406.97	1438.22	10616.60	66.63
A50-P6.2	1.78	4.69	0.93	14094.30	33247.20	838.77	27.27

As can be noticed in Fig. 3.3, the top skin layer and the bottom surface are the less porous regions of the membranes, concentrating the smaller pores as well. V0 and V5 were then chosen to analyze the influence of these denser layers on the permeability of the membranes. Permeability is related to the capability of fluids to percolate porous media. The difficulty in percolating increases if the porous media is more resistive, i.e. if the porous media presents narrow constrictions. This is in agreement with the simulation results. The values found for the last set of simulations (V0, V5, and V_{total}) are far lower than those found for the intermediary layers (V1, V2, V3, and V4). Even though the intermediate layers present larger pores, it is the porous regions at the skin layer and bottom surface that control the permeability of the membranes. The results are also in agreement with the water flux results found for the co-cast

membranes compared to their counterparts produced under standard conditions (Fig. 3.8d). Although A45-P7 and A50-P6.2 present similar permeabilities for the bottom surface volume (V5), which indicates similar flux resistances for both membranes in this region, the permeability of the upper region which includes the skin layer (V0) is considerably higher for A45-P7. Consequently, the removal of the less porous bottom layer (Fig. 3d) by co-casting (Fig. 3h) for these membranes allowed a significant improvement in water flux for the membranes G-A45-P7 compared to A45-P7. On the other hand, after removing the bottom layer of A50-P6.2 membranes (G-A50-P6.2), the low permeability of the skin layer for this slurry composition still hinders the membrane flux.

3.4 CONCLUSIONS

Asymmetric alumina membranes were successfully prepared by combining tape casting and phase inversion. The membranes presented surface large pore sizes (0.30 – 0.42 µm) in a range suitable for microfiltration and outstanding water permeability up to 38 times higher than those of commercial microfiltration membranes with large APS (0.6 µm).

Alumina loading was the main influence on membrane morphology, but not on surface pore sizes. Increasing the amount of alumina decreases the flux in accordance with the observed morphology of each membrane. Even for the regions where finger-like pores are not easily observed in 2D images, intrinsic permeability simulation from Micro-CT scans has proven the existence of a flow direction preference towards the z-axis (from top to bottom, as the finger-like pores).

Membranes prepared with a slurry with 45/7 and 50/6.2 alumina/PES wt% are considered to have the best set of properties in terms of flexural strength and permeability. Increasing the mixing time of the slurry resulted in membranes with slightly improved water flux. In turn, increasing sintering temperature has not modified membranes' microstructure or water flux. Graphite co-casting has proven to be an excellent strategy to further improve membrane performance. The overall permeability of the membranes is controlled by the skin layer and bottom surface regions.

Phase-inversion tape casting has proven to be a promising alternative route to produce microfiltration ceramic membranes with higher performance and energy savings compared to conventional methods since only one sintering step is necessary.

3.5 REFERENCES

[1] S. Mozia, Photocatalytic membrane reactors (PMRs) in water and wastewater treatment. A review, Sep. Purif. Technol. 73 (2010) 71–91. https://doi.org/10.1016/j.seppur.2010.03.021

[2] M. Padaki, R.S. Murali, M.S. Abdullah, N. Misdan, A. Moslehyani, M.A. Kassim, N. Hilal, A.F. Ismail, Membrane technology enhancement in oil–water separation. A review, Desalination. 357 (2015) 197–207.

https://doi.org/10.1016/j.desal.2014.11.023

[3] P.S. Goh, A.F. Ismail, A review on inorganic membranes for desalination and wastewater treatment, Desalination. 434 (2017) 60–68. https://doi.org/10.1016/J.DESAL.2017.07.023.

[4] X. Lu, J. Yang, X. Li, F. Sun, F. Wang, Y. Chao, Effects of phase transformation on properties of alumina ceramic membrane: A new assessment based on quantitative X-ray diffraction (QXRD), Chem. Eng. Sci. 199 (2019) 349–358. https://doi.org/10.1016/j.ces.2018.12.054.

[5] B.A. da Silva, V. de Souza Godim de Oliveira, M. Di Luccio, D. Hotza, K. Rezwan, M. Wilhelm, Characterization of functionalized zirconia membranes manufactured by aqueous tape casting, Ceram. Int. 46 (2020) 16096–16103. https://doi.org/10.1016/j.ceramint.2020.03.162.

[6] S. Leong, A. Razmjou, K. Wang, K. Hapgood, X. Zhang, H. Wang, TiO2 based photocatalytic membranes: A review, J. Memb. Sci. 472 (2014) 167–184. https://doi.org/10.1016/j.memsci.2014.08.016.

[7] M. Kukizaki, Shirasu porous glass (SPG) membrane emulsification in the absence of shear flow at the membrane surface: Influence of surfactant type and concentration, viscosities of dispersed and continuous phases, and transmembrane pressure, J. Memb. Sci. 327 (2009) 234–243. https://doi.org/10.1016/j.memsci.2008.11.026.

[8] D. Hotza, M. Di Luccio, M. Wilhelm, Y. Iwamoto, S. Bernard, J.C. Diniz da Costa, Silicon carbide filters and porous membranes: A review of processing, properties, performance and application, J. Memb. Sci. 610 (2020).

https://doi.org/10.1016/j.memsci.2020.118193.

[9]   S.M. Samaei, S. Gato-Trinidad, A. Altaee, The application of pressure-driven ceramic membrane technology for the treatment of industrial wastewaters – A review, Sep. Purif. Technol. 200 (2018) 198–220.

https://doi.org/10.1016/j.seppur.2018.02.041.

[10]   M. Lee, Z. Wu, K. Li, 2. Advances in ceramic membranes for water treatment, A. Basile, A. Cassano, N.K. Rastogi (Eds.), Advances in Membrane Technologies for Water Treatment, Woodhead Publishing, Oxford (2015), p. 43-82. https://doi.org/10.1016/B978-1-78242-121-4.00002-2.

[11]   K.P. Lee, T.C. Arnot, D. Mattia, A review of reverse osmosis membrane materials for desalination-Development to date and future potential, J. Memb. Sci. 370 (2011) 1–22. https://doi.org/10.1016/j.memsci.2010.12.036.

[12]   S.F. Anis, R. Hashaikeh, N. Hilal, Microfiltration membrane processes: A review of research trends over the past decade, J. Water Process Eng. 32 (2019) 100941. https://doi.org/10.1016/j.jwpe.2019.100941.

 [13]   W. He, H. Huang, J. fen Gao, L. Winnubst, C. Sheng Chen, Phase-inversion tape casting and oxygen permeation properties of supported ceramic membranes, J. Memb. Sci. 452 (2014) 294–299. https://doi.org/10.1016/j.memsci.2013.09.063.

[14]   G.R. Guillen, Y. Pan, M. Li, E.M.V. Hoek, Preparation and characterization of membranes formed by nonsolvent induced phase separation: A review, Ind. Eng. Chem. Res. 50 (2011) 3798–3817. https://doi.org/10.1021/ie101928r.

[15]   R.K. Nishihora, E. Rudolph, M. Gabriela, N. Quadri, D. Hotza, K. Rezwan, M. Wilhelm, Asymmetric mullite membranes manufactured by phase-inversion tape casting from polymethylsiloxane and aluminum diacetate, J. Memb. Sci. 581 (2019) 421–429. https://doi.org/10.1016/j.memsci.2019.03.047.

[16]   B.F.K. Kingsbury, K. Li, A morphological study of ceramic hollow fibre membranes, J. Memb. Sci. 328 (2009) 134–140. https://doi.org/10.1016/j.memsci.2008.11.050.

[17] B. Wang, Z. Lai, Finger-like voids induced by viscous fingering during phase inversion of alumina/PES/NMP suspensions, J. Memb. Sci. 405–406 (2012) 275–283. https://doi.org/10.1016/j.memsci.2012.03.020.

[18] G. Mustafa, K. Wyns, A. Buekenhoudt, V. Meynen, Antifouling grafting of ceramic membranes validated in a variety of challenging wastewaters, Water Res. 104 (2016) 242–253. https://doi.org/10.1016/j.watres.2016.07.057.

[19] S. Tao, Y.D. Xu, J.Q. Gu, H. Abadikhah, J.W. Wang, X. Xu, Preparation of high-efficiency ceramic planar membrane and its application for water desalination, J. Adv. Ceram. 7 (2018) 117–123. https://doi.org/10.1007/s40145-018-0263-7.

[20] L. Zhu, M. Chen, Y. Dong, C.Y. Tang, A. Huang, A low-cost mullite-titania composite ceramic hollow fiber microfiltration membrane for highly efficient separation of oil-in-water emulsion, Water Res. 90 (2016) 277–285. https://doi.org/10.1016/J.WATRES.2015.12.035.

[21] S.K. Hubadillah, Z. Harun, M.H.D. Othman, A.F. Ismail, P. Gani, Effect of kaolin particle size and loading on the characteristics of kaolin ceramic support prepared via phase inversion technique, J. Asian Ceram. Soc. 4 (2016) 164–177. https://doi.org/10.1016/j.jascer.2016.02.002.

[22] L. Yu, M. Kanezashi, H. Nagasawa, T. Tsuru, Phase inversion/sintering-induced porous ceramic microsheet membranes for high-quality separation of oily wastewater, J. Memb. Sci. (2020) 117477. https://doi.org/10.1016/j.memsci.2019.117477.

[23] Z. Zhu, J. Xiao, W. He, T. Wang, Z. Wei, Y. Dong, Short Communication A phase-inversion casting process for preparation of tubular porous alumina ceramic membranes, J. Eur. Ceram. Soc. 35 (2015) 3187–3194. https://doi.org/10.1016/j.jeurceramsoc.2015.04.026.

[24] X. Zhang, D.K. Wang, D. Ruben, S. Lopez, J.C. Diniz, Fabrication of nanostructured TiO_2 hollow fiber photocatalytic membrane and application for wastewater treatment, Chem. Eng. J. 236 (2014) 314–322. https://doi.org/10.1016/j.cej.2013.09.059.

[25] N. Abdullah, M.A. Rahman, M.H.D. Othman, A.F. Ismail, J. Jaafar, A.A. Aziz, Preparation and characterization of self-cleaning alumina hollow fiber membrane using the phase inversion and sintering technique, Ceram. Int. 42 (2016) 12312–12322. https://doi.org/10.1016/j.ceramint.2016.05.003.

[26]   C. Ren, H. Fang, J. Gu, L. Winnubst, C. Chen, Preparation and characterization of hydrophobic alumina planar membranes for water desalination, J. Eur. Ceram. Soc. 35 (2015) 723–730. https://doi.org/10.1016/j.jeurceramsoc.2014.07.012.

[27]   J.Q. Gu, C. Ren, X. Zong, C. Chen, L. Winnubst, Preparation of alumina membranes comprising a thin separation layer and a support with straight open pores for water desalination, Ceram. Int. 42 (2016) 12427–12434. https://doi.org/10.1016/j.ceramint.2016.04.183.

[28]   Y. Meng, W. He, X. Xiang Li, J. Gao, Z. Zhan, J. Yi, C. Chen, H.J.M. Bouwmeester, Asymmetric La0.6Sr0.4Co0.2Fe0.8O3-Δmembrane with reduced concentration polarization prepared by phase-inversion tape casting and warm pressing, J. Memb. Sci. 533 (2017) 11–18. https://doi.org/10.1016/j.memsci.2017.03.025.

[29]   R. Yuan, W. He, Y. Zhang, J. Gao, C. Chen, Preparation and characterization of supported planar Zr0.84Y0.16O1.92–La0.8Sr0.2Cr0.5Fe0.5O3-δ composite membrane, J. Memb. Sci. 499 (2016) 335–342. https://doi.org/10.1016/j.memsci.2015.10.066.

[30]   S.K. Hubadillah, M.H.D. Othman, T. Matsuura, A.F. Ismail, M.A. Rahman, Z. Harun, J. Jaafar, M. Nomura, Fabrications and applications of low-cost ceramic membrane from kaolin: A comprehensive review, Ceram. Int. 44 (2018) 4538–4560. https://doi.org/10.1016/j.ceramint.2017.12.215.

[31]   H. Huang, J. Lin, Y. Wang, S. Wang, C. Xia, C. Chen, Facile one-step forming of NiO and yttrium-stabilized zirconia composite anodes with straight open pores for planar solid oxide fuel cell using phase-inversion tape casting method, J. Power Sources. 274 (2015) 1114–1117. https://doi.org/10.1016/j.jpowsour.2014.10.190.

[32]   N.P. Stochero, E.G. de Moraes, A.C. Moreira, C.P. Fernandes, M.D.M. Innocentini, A.P. Novaes de Oliveira, Ceramic shell foams produced by direct foaming and gelcasting of proteins: Permeability and microstructural characterization by X-ray microtomography, J. Eur. Ceram. Soc. 40 (2020) 4224–4231. https://doi.org/10.1016/j.jeurceramsoc.2020.05.036.

[33]   Dong, H., Blunt M., Pore-network extraction from micro-computerized-tomography imagens. Physical Review 80(3) (2009) 1-11. https://doi.org/10.1103/PhysRevE.80.036307

[34]   P.H. Valvatne, M.J. Blunt Predictive pore-scale modeling of two-phase flow in mixed wet media Water Resour. Res., 40 (2004), 1-21. https://doi.org/10.1029/2003WR002627

[35]   Dong, H., 2007. Micro-CT imaging and pore network extraction. Ph.D. Dissertation, Imperial College London, London, England, 213p.

[36]   Al-Kharusi, A. S. Z., 2007. Pore-scale characterization of carbonate rocks. Ph.D. Dissertation, Department of Earth Science and Engineering, Imperial College London, London, England, 275 p.

[37]   Silin, D., Patzek T., Pore space morphology analysis using maximal inscribed spheres. Physica a 371, (2006) 330-360.

https://doi.org/10.1016/j.physa.2006.04.048

[38]   C. Daish, R. Blanchard, K. Gulati, D. Losic, D. Findlay, D.J.E. Harvie, P. Pivonka, Estimation of anisotropic permeability in trabecular bone based on microCT imaging and pore-scale fluid dynamics simulations, Bone Reports. 6 (2017) 129–139. https://doi.org/10.1016/j.bonr.2016.12.002.

[39]   S.K. Hubadillah, M.H.D. Othman, M.A. Rahman, A.F. Ismail, J. Jaafar, Preparation and characterization of inexpensive kaolin hollow fibre membrane (KHFM) prepared using phase inversion/sintering technique for the efficient separation of real oily wastewater, Arab. J. Chem. 13 (2020) 2349-2367. https://doi.org/10.1016/j.arabjc.2018.04.018.

[40]   Y. Cheng, Y. Yu, C. Peng, J. Wu, Preparation and characterization of high flux alumina membrane supports by composite pore former method, Ceram. Int. 46, 8, Part 1 (2020) 11297-11303. https://doi.org/10.1016/j.ceramint.2020.01.158.

[41]   W. Zhu, Y. Liu, K. Guan, C. Peng, W. Qiu, J. Wu, Integrated preparation of alumina microfiltration membrane with super permeability and high selectivity, J. Eur. Ceram. Soc. 39 (2019) 1316–1323. https://doi.org/10.1016/j.jeurceramsoc.2018.10.022

[42]   K. Suresh, G. Pugazhenthi, Cross flow microfiltration of oil-in-water emulsions using clay based ceramic membrane support and TiO2 composite membrane, Egypt. J. Pet. (2016) 679–694. https://doi.org/10.1016/j.ejpe.2016.10.007.

[43]   H.R. Mahdavi, M. Arzani, T. Mohammadi, Synthesis, characterization and performance evaluation of an optimized ceramic membrane with physical separation and photocatalytic degradation capabilities, Ceram. Int. 44 (2018) 10281–10292.

https://doi.org/10.1016/j.ceramint.2018.03.035.

[44]   Chen, M. Duan, S. Fang, Fabrication of novel superhydrophilic and underwater superoleophobic hierarchically structured ceramic membrane and its separation performance of oily wastewater, Ceram. Int. 42 (2016) 8604–8612.

https://doi.org/10.1016/j.ceramint.2016.02.090.

[45]   N. Das, S. Bandyopadhyay, D. Chattopadhyay, H.S. Maiti, Tape-cast ceramic membranes for microfiltration application, J. Mater. Sci. 31 (1996) 5221–5225.

https://doi.org/10.1007/bf00355928.

4 PHOTOCATALYTIC MICROFILTRATION MEMBRANES PRODUCED BY MAGNETRON SPUTTERING WITH SELF-CLEANING CAPABILITIES

This chapter refers to the study of the deposition of Al_2O_3 membranes with TiO_2 by magnetron sputtering as a strategy to produce photocatalytic membranes with tailored porosity. For this purpose, membranes produced as denoted as "A50-P6.2" in Chapter 2 were used.

This study meets the specific objectives described in Section 1.1.2 Specific objectives – Chapter 4. The Experimental procedure presented here was partially performed at the Surface Engineering Laboratory of the Manchester Metropolitan University (MMU, England).

The complete work carried out in this chapter is presented below in article format, as published in the scientific journal Thin Solid Films (2022) (https://doi.org/10.1016/j.tsf.2022.139143).

4.1 INTRODUCTION

The world faces severe pressure on clean water supplies, leading to serious environmental and population health problems [1,2]. Given the increasing amount and complexity of industrial effluents and the inefficiency of conventional water and wastewater treatment techniques in treating them properly, there is an urgent need for technologies to improve wastewater treatment, removing even trace amounts of toxic pollutants [2–6]. Membrane separation processes [2,7] and advanced oxidative processes such as photocatalysis [8–10] and hybrid systems [11–14] have emerged as important technologies to overcome such limitations.

Micro-, ultra-, and nanofiltration membranes are physical selective porous barriers with progressively reduced pore sizes and a gradient pressure is used as a driving force for filtration. [15]. The membrane surface plays the role of the selective barrier. Thus, membrane selectivity (separation capacity) is mainly governed by the relation between the pore size of the membrane surface and the size of the pollutant molecule. Smaller pore sizes lead to higher selectivity but increase the flux resistances, which reduces the flux and leads to higher energy consumption [16,17]. Therefore, asymmetric membranes with a hierarchical porous structure composed of a porous support (mechanical resistance and high permeability) and one or several layers with

gradient porosity (suitable surface pore size) have been developed to produce membranes with high permeability and selective [18–20]. It should also be noted that the effective membrane thickness may vary from the theoretical one, as it is based on a previous calibration made by deposition on a smooth substrate.

Despite the benefits and current importance, ceramic membranes still suffer from serious fouling problems. Fouling is a common process where species present in the filtration medium block pores by forming a cake-like layer on the membrane surface or depositing inside the pores, which hinders membrane flux [7]. Various strategies, including the use of Photocatalytic Membranes (PMs), have been investigated to produce membranes with antifouling or self-cleaning capabilities that could improve filtration performance and life span of the membrane and reduce replacement costs [6,21–25]. Photocatalysis is based on the generation of high reactive radicals on a photocatalyst by a suitable luminous source. By using an efficient photocatalyst on the membrane surface exposed to the light, refractory or toxic compounds deposited on the membrane surface could be degraded and/or eliminated. Titania (TiO$_2$) is the most used photocatalyst, with the anatase phase generally considered more active than the rutile phase [26]. Under UV irradiation, TiO$_2$ PM could achieve an effective removal of organic matter such as dyes [27], phenol [28], oil [29], and emerging pollutants [30]. PMs can be produced by depositing an active layer on the membrane surface.

The deposition of a thin layer of photocatalyst is frequently done by sol-gel dip-coating [31] or chemical vapor deposition [32], but can also be done by physical vapor deposition, such as magnetron sputtering [33]. Magnetron sputtering is a plasma-based thin film deposition process used to produce a wide variety of metallic and ceramic coatings. It is reproducible, highly scalable, and provides excellent control over the chemical and morphological properties of the deposited materials [34]. Magnetron sputtering is an industrially-relevant method of choice to produce photocatalytic coatings as it provides reliable control of parameters such as crystallinity, composition, and thickness is applicable for several types of photocatalysts and presents good adhesion [35]. Although it has been applied to several types of surfaces, photocatalytic membranes produced by this technique are scarce [17,33,36,37].

Sanchez et al. [33] have investigated photocatalytic ceramic membranes functionalized by magnetron sputtering. Nevertheless, self-cleaning properties were not evaluated and only nanofiltration membranes were used by the authors. Due to the high potential of such a hybrid system, further investigation should be performed to produce efficient, self-cleaning, and long-

lasting membranes. In this sense, the objective of the present work was to evaluate the effect of varying the amount of deposited photocatalyst on microfiltration alumina membranes to produce photocatalytic membranes with tailored porosity and self-cleaning capabilities.

4.2   EXPERIMENTAL

4.2.1   Membrane preparation

Alumina flat membranes (approximately 16 mm x 16 mm x 0.7 mm) with pore sizes suitable for the microfiltration process, produced as previously reported [38], were coated with titanium dioxide thin films via pulsed Direct Current (pDC) reactive magnetron sputtering. The deposition process was performed under high vacuum, with a base pressure of $3x10^{-3}$ Pa and a working pressure of $4.4x10^{-1}$ Pa, achieved through a combination of rotary (BOC Edwards 80) and turbo-molecular (Leybold TMP1000) pumps. A single 300x100 mm titanium target (99.5% purity) was fitted onto a Gencoa Ltd unbalanced type II magnetron. The distance between the target and the substrate was set to 50 mm. The argon flow rate was maintained via mass-flow controller and kept constant at 50 sccm for all experimental runs. The oxygen flow was regulated by a Speedflo®™ controller from Gencoa Ltd to produce stoichiometric films and to minimize target poisoning. The magnetron was powered by an Advanced Energy Pinnacle Plus power supply in pDC mode operating at 1 kW, pulse frequency of 100 kHz, and 60% duty cycle.

The coating thickness was estimated by simultaneously depositing titanium dioxide on alumina membranes and flat microscope glass slide substrates under the same deposition conditions. The coating thickness on the glass slide was measured by creating an artificial step, by covering part of it with Kapton tape before the deposition. A Profilm3D interferometer from Filmetrics, with a magnification of 50x, was used to measure the height of the artificial step. Based on a previous calibration, coatings of 50, 200, and 400 nm of estimated thickness were deposited on membrane surfaces by varying the deposition time from 5 to 30 minutes. The films were annealed in air at 600 °C for 1 h in an electric furnace. Membranes here are denoted as "MS-x nm", where x relates to coating thickness.

Before filtration tests, membranes were cut in circles of 1 cm diameter (geometric area of filtration was 0.785 cm^2).

4.2.2 Membrane morphology and surface chemistry

Scanning electron microscopy (SEM) (Zeiss Supra 40 VP-FEG-SEM) images obtained at 2 kV using secondary electron mode at 2 kV and electron dispersive spectroscopy (EDS) analysis (Tescan Vega-3 LMU coupled with a probe of energy-dispersive X-ray spectroscopy) were used to analyze the effect of the coatings in terms of surface morphology and composition. For EDS imaging, 15 mm of working distance, 15 kV voltage, and 9 MV beam intensity were used. Average pore sizes of the surface were determined from SEM images (5000 x magnification) using dedicated software (ImageJ) [38,39]. Raman spectroscopy (Anton Paar Cora 5200, integration time = 5000 ms, 250 mW, 784 nm, 5 scans for each sample) and X-ray diffraction (XRD) (PANalytical X'pert powder diffractometer with CuKα radiation (λ = 1.541 Å) were used to identify the crystalline phases on the membrane upper surface. For XRD analysis, a piece of an as-produced coated membrane was mounted in a horizontal position on the sample stage. Grazing incidence mode at 0.5-degree angle of incidence over a scan 2θ range from 20° to 60°, 40 kV accelerating voltage and 30 mA applied current were used.

4.2.3 Photocatalytic activity

The photocatalytic activity was evaluated through methylene blue (MB) photocatalytic decolorization under ultraviolet irradiation (UV). Membranes were placed into crystallization dishes containing a solution of 3.2 mg L^{-1} MB in water and kept in the dark for 24 h to ensure the adsorption equilibrium was achieved. Next, membranes were transferred to a new 3.2 mg L^{-1} MB solution and exposed to UV light (λ = 365 nm, 15 W) for 24 h. The resulting MB decolorization was analyzed using a UV-Vis spectrophotometer via absorbance decay measurements. The percentage of MB removal (%MB removal) was calculated as described in Equation. 1

$$\% \, MB \, removal = (1 - C/C_0).100\% \qquad (1)$$

where C_0 and C are respectively, the initial and final MB concentration.

4.2.4 Filtration experiments

Membrane filtration tests were performed using a self-made membrane module equipped with a UV LED light (3 W LED, λ = 365 nm), placed 7 cm above the membrane surface on the permeation side and the flux was set in a cross-flow configuration, with total retentate recycling (Fig. 4.1). The permeate flux (J) (L m^{-2} h^{-1}) along the experiments was calculated according to Equation 2, where V (L) is the permeated volume in a period t (h) through a membrane surface area A (m^2).

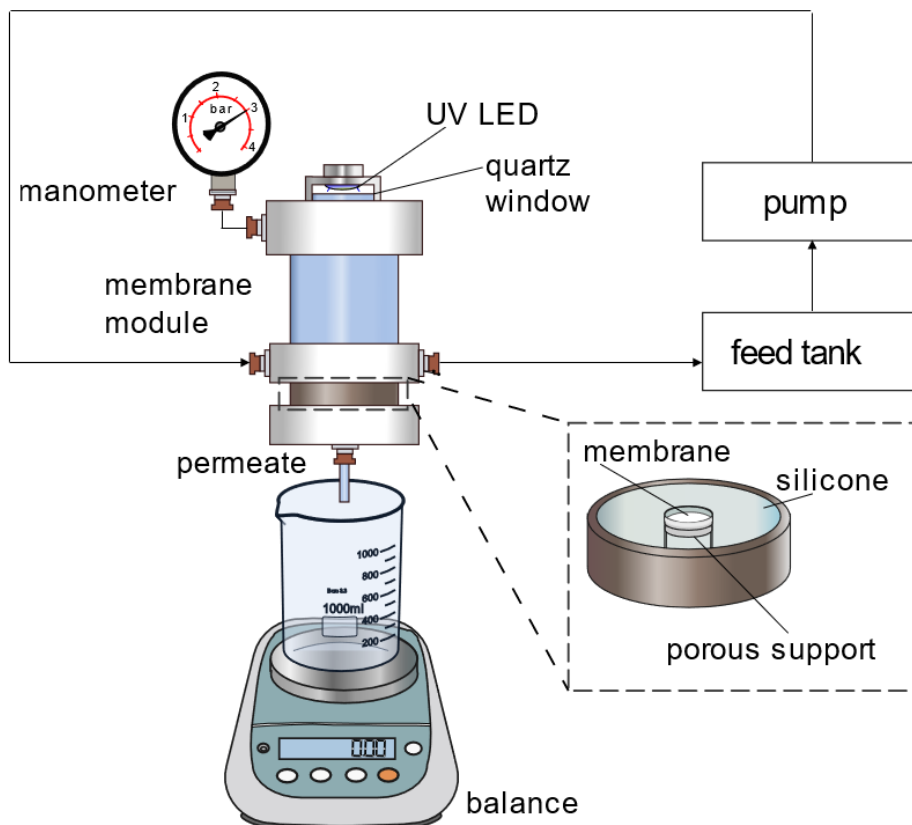$$J = \frac{1}{A} \cdot \frac{dV}{dt} \qquad\qquad (2)$$

Figure 4.1 Membrane module.

The experiments were divided into three different filtration test sets. In the first and second sets, membranes with the thicker TiO_2 layers, namely MS-200 nm and MS-400 nm were used to filter an MB solution (3.2 mg L^{-1}). Transmembrane pressure (TMP) was set at 0.3 MPa. For the third set, the membrane MS-50 nm was used to filter a soybean oil emulsion (1 g L^{-1}) at 0.1 MPa TMP. To produce the oily emulsion, 2 mM of sodium dodecyl sulfate was dissolved in 1 L of deionized water. Then, 1 g of soybean oil was mixed under vigorous magnetic stirring for 5 min, followed by sonication for 5 min. At the end of each experiment, the membrane was kept inside the filled module for 15 h under UV at ambient pressure. No transport of the solution through the membrane was observed during this period. Next, without removing the membrane or emptying the module/recirculation tank, TMP was set back to 0.3 MPa (in the case of MB filtration) or 0.1 MPa (in the case of oil emulsion filtration), and a new filtration cycle (2nd cycle) was initiated to evaluate the fouling self-cleaning properties of each membrane/system.

The first filtration test was conducted with the membrane with the thicker TiO_2 layer, MS-400 nm, without UV light for 1 h, followed by the 15 h interval under UV. The 2nd cycle was performed under the same conditions as the 1st cycle. For the second filtration test, the membrane MS-200 nm was used. Here, the first filtration cycle was performed without UV light for 45 min, followed by a further 30 min permeation under UV light. TMP was then set to ambient pressure for the 15 h interval under UV before the 2nd cycle was started. For the 2nd filtration cycle, the experiment started once again at 0.3 MPa without UV, which was then turned on after a permeation volume of 5 mL was reached. Permeate MB concentration after each test was obtained through a UV-Vis spectrophotometer and the %MB removal was calculated according to Equation 1.

For the third set, the membrane MS-50 nm was used to filter a soybean oil emulsion (1 g L^{-1}) at 0.1 MPa. Three permeate samples were collected after 15, 25, and 35 mL permeate, respectively. After the first sampling, the UV light was switched on. For each permeate sample, %Turbidity removal was calculated according to Equation 3, where *Turb* and *Turb$_0$* are the sampled permeate and feed emulsion turbidity respectively. At the end of the filtration experiment, overall membrane selectivity was evaluated in terms of Total Organic Carbon (TOC) according to Equation 4, where TOC is the TOC of the filtrate at the end of the experiment and TOC_0 refers to the feed emulsion TOC.

$$\%Turb\ removal = \left(1 - \frac{Turb}{Turb_0} \right).100\% \tag{3}$$

$$\%TOC\ removal = \left(1 - \frac{TOC}{TOC_0} \right).100\% \tag{4}$$

4.3   RESULTS AND DISCUSSION

4.3.1   Membrane morphology and surface chemistry

The coated membrane surfaces have been analyzed by SEM. Fig. 2(a-c) shows SEM images of surface cross-section (50kx magnification) for uncoated, 50 nm, and 400 nm coated membranes, respectively. A columnar layer of TiO_2 on the surface of the membrane can be observed for MS-400 nm membrane (Fig. 2c), displaying a thickness close to 400 nm. Although surface modification can also be observed at MS-50 nm (Fig. 2b), it is less obvious due to the smaller thickness of the coating layer combined with the porous natures of the membranes. Furthermore, a 10kx magnification SEM image of the MS-50 nm (Fig. 2d) revealed the presence of heterogeneity in the degree of membrane surface coverage.

TiO_2 coating layers can play different roles. First, TiO_2 has been used to improve permeability by improving membrane hydrophilicity and/or producing light-induced hydrophilicity, besides reducing fouling caused by non-polar compounds such as oil molecules. In this case, TiO_2 surface coverage can contribute to membrane performance [29,40,41], due to the combined effect of enhanced hydrophilicity and photocatalytic activity under light irradiation. Second, TiO_2 can produce photocatalytic membranes, which have been used for photocatalytic degradation of bulk contaminants using immobilized photocatalysts followed by non-simultaneous filtration [42]; to degrade small molecules which cannot be retained during filtration [43]; and, more interestingly, to produce self-cleaning, antifouling membranes and photocatalytic activity under light irradiation [44,45]. In the last case, the homogeneous and complete coverage of the membrane surface with TiO_2 is an important issue.

Figure 4.2 SEM images of surface cross-section (50kx magnification) before (a) and after film deposition for (b) MS-50 nm and (c) MS-400 nm, and (d) SEM image (10kx) of membrane surface for MS-50 nm, indicating coverage heterogeneity.

Finally, coating deposition can be used for pore size tailoring depending on the desired application (particle size of the pollutants). Fig. 4.3 shows SEM micrographs of the surfaces for the bare membrane (a) and after film deposition for (b) MS-50 nm, (c) MS-200 nm, and (d) MS-400 nm. Membrane surfaces modified by the addition of a TiO_2 layer increased in thickness from 50 nm (MS-50 nm) and 200 nm (MS-200 nm) (Fig. 4.3b-c) when compared to the uncoated membrane (Fig. 4.3a). When the thickness of the coating layer is further increased to 400 nm (Fig. 4.3d) no difference is observed anymore compared to the 200 nm coating layer (MS-200 nm).

No significant changes in the pore sizes were observed for the MS-50 nm compared to the bare membrane (Table 4.1). On the other hand, for the membranes MS-200 nm and MS-400 nm, the deposited layer almost filled the whole surface pores, when compared to the uncoated membrane. For these membranes, average pore sizes were reduced to 0.12 μm. Besides, the total membrane area occupied by pores dropped from almost 9% for the bare and MS-50 nm membranes, to less than 1% for MS-200 nm and MS-400 nm. All membranes were

in a pore size range (0.62-0.12 μm) suitable for microfiltration, while MS-200 nm and MS-400 nm could also be considered ultrafiltration membranes. This result suggests that magnetron sputtering can be used to produce tailored surface porosity, although further intermediary coating thickness needs to be investigated.

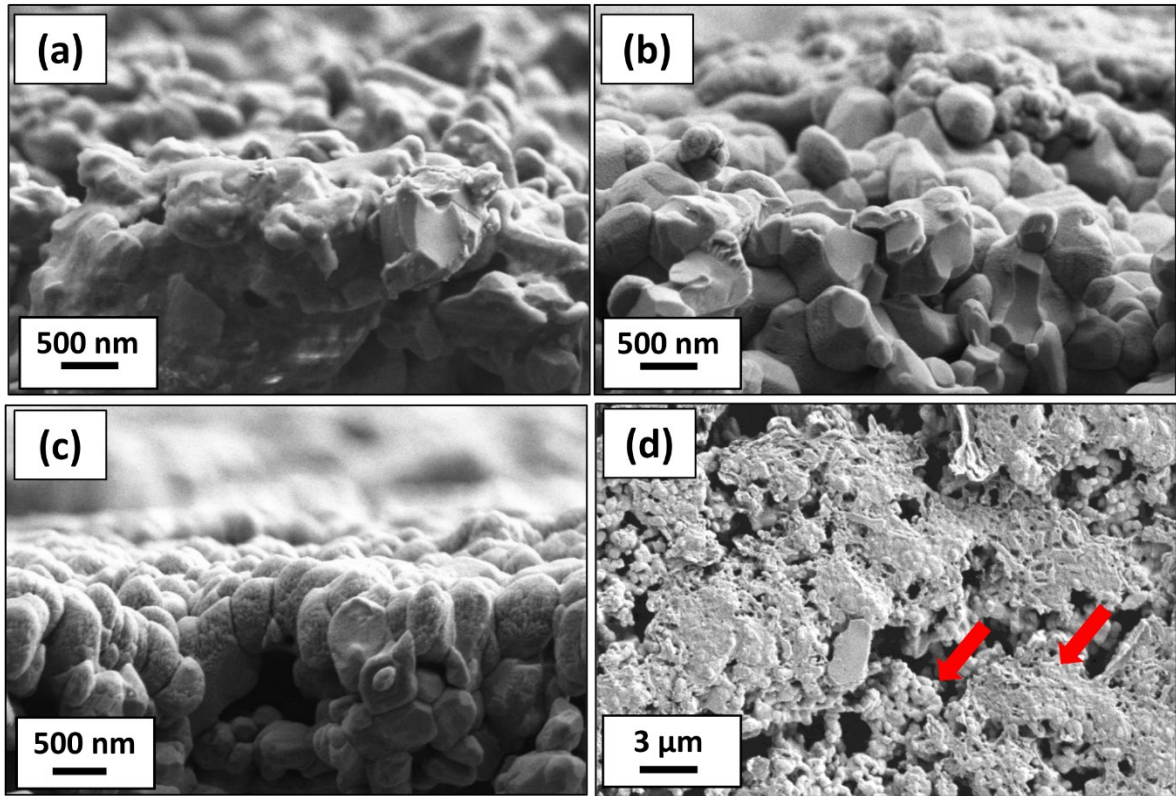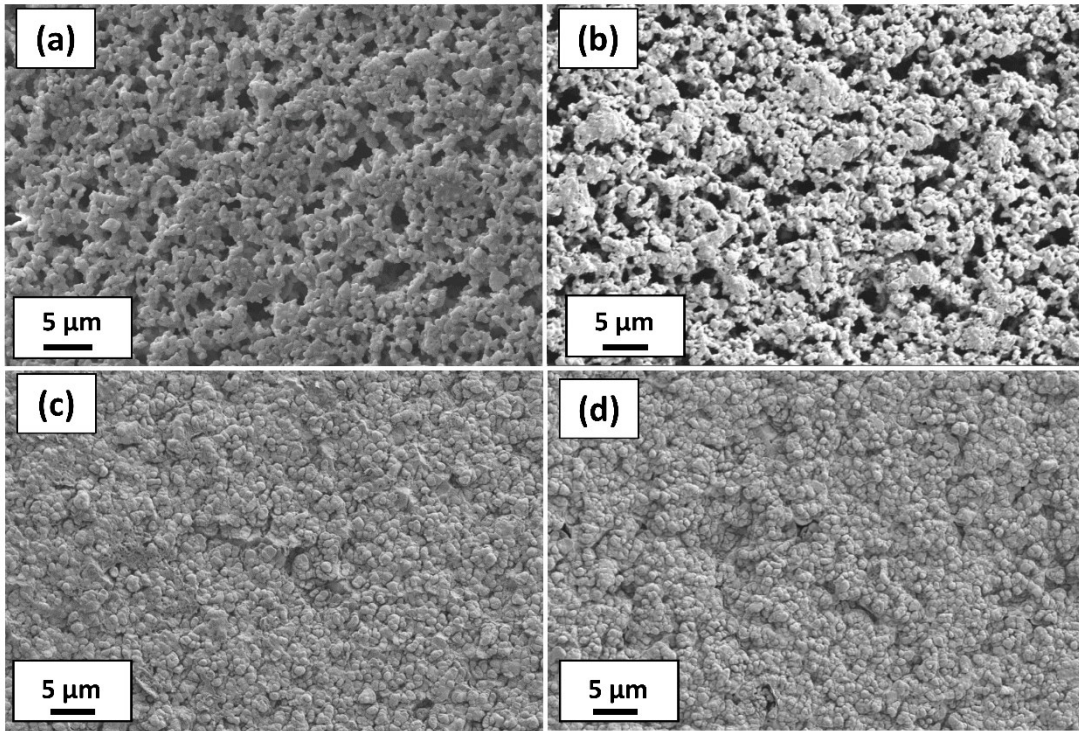
Figure 4.3 SEM images of membrane surface (5kx magnification) before (a) and after film deposition for (b) MS-50 nm, (c) MS-200 nm, and (d) MS-400 nm.

Table 4.1 Average pore size, number of pores counted, and %area occupied by pores from surface image processing (SEM images 5000x magnification) using dedicated software (ImageJ).

Membrane	Average pore size (μm)	Counts	% Area occupied by pores
Bare	0.63	535	9
MS-50 nm	0.49	531	9
MS-200 nm	0.12	1144	<1
MS-400 nm	0.14	1542	<1

EDS elemental mapping analysis for aluminum (green), oxygen (blue), and titanium (red) were performed using an MS-200 nm membrane, with the SEM image showing both, surface and cross-section portions. (Fig. 4.4a). While Al and O are well distributed on both

sections, the Ti map confirms the presence of Ti homogeneously distributed on the membrane surface. Although the sparse red point indicates the presence of Ti along the membrane cross-section, EDS data for two selected areas (Spectrum 1 and 2 in Fig. 4.4b) identified the presence of aluminum and oxygen. An element profile (Fig. 4.4c) was obtained along a data line (Fig. 4.4b) from the estimated surface to the inside of the membrane through the cross-section. It was possible to confirm that Ti penetrated only a few micrometers (less than 8 µm) inside the membrane pores. The presence of Au visible in Fig. 4.4c is due to gold sputtering before the SEM images were taken. Titania in the anatase phase was formed on coated membrane surfaces according to Raman spectrum (Fig. 4.5a) and further confirmed by XRD (Fig. 4.5b), while no rutile peaks were found. Additionally, a significant increase in anatase peaks was observed in the XRD patterns of the coating from 50 to 400 nm coatings.
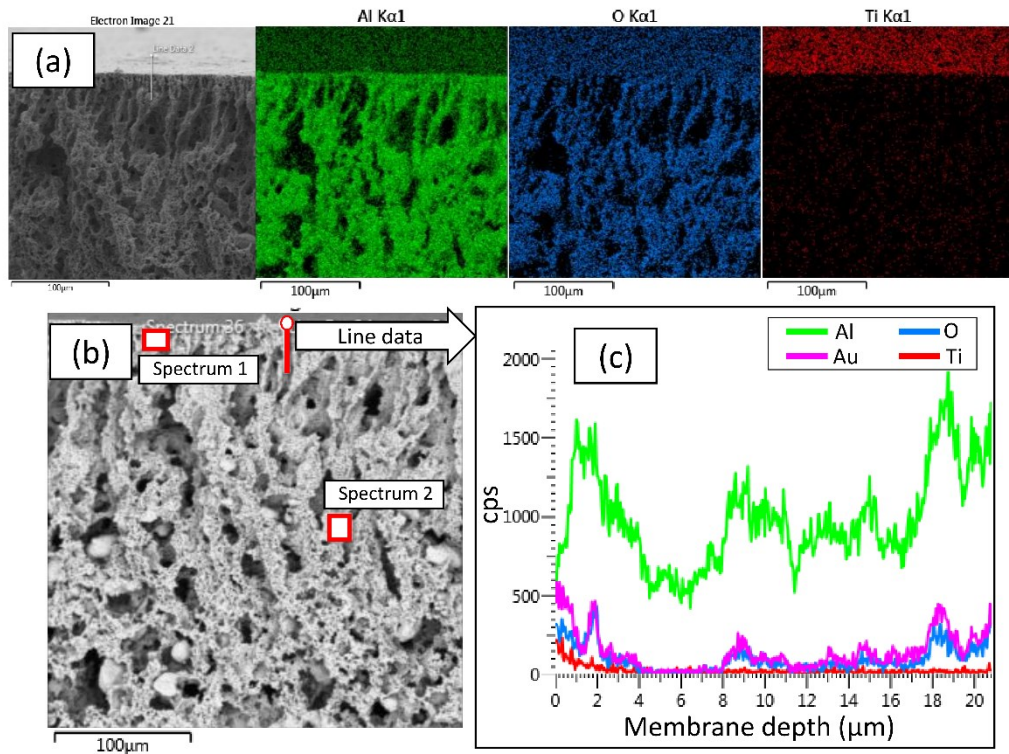
Figure 4.4 (a) Color mapping for aluminium, oxygen, and titanium of a MS-200 nm membrane, (b) near-surface cross-section SEM image of a MS-200 nm membrane with selected two areas (spectrum 1 and 2) and a line for EDS analysis, and (c) element data along the selected line.
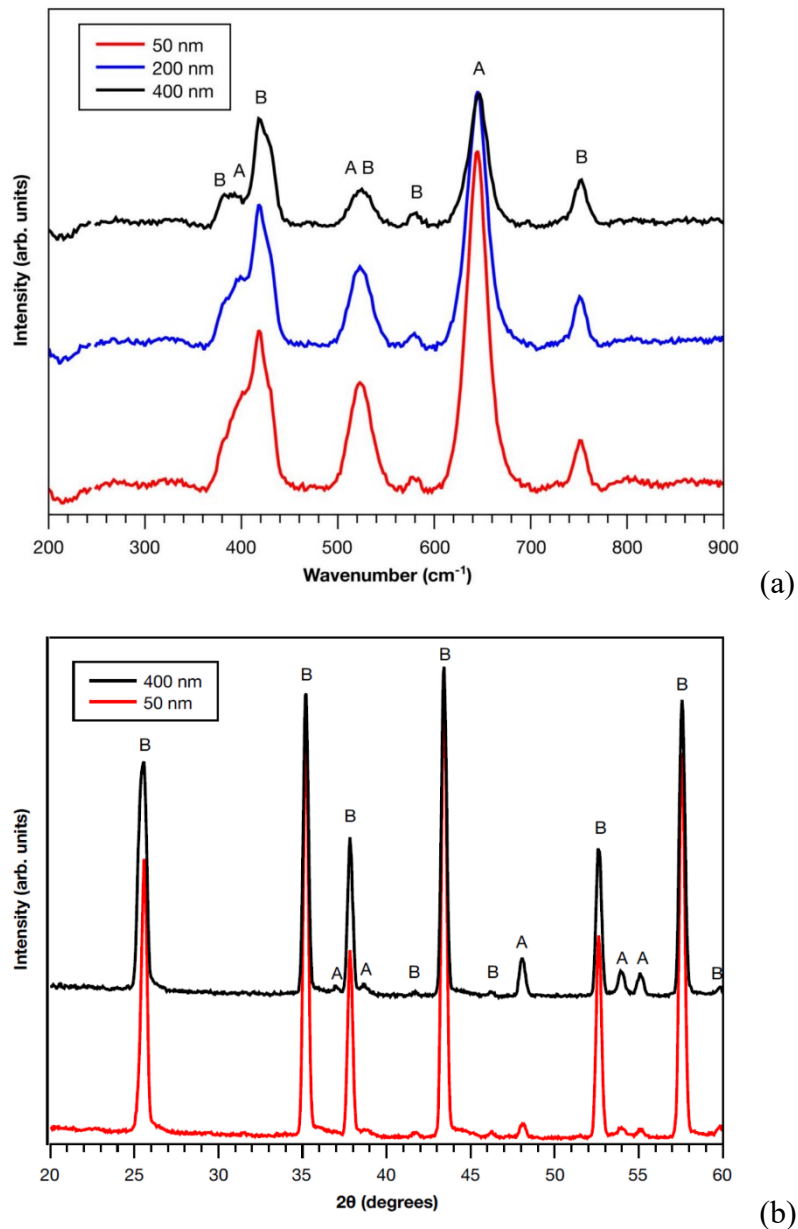
Figure 4.5 Raman (a) and XRD spectra (b) for produced membranes. Peaks assigned as "A" refer to the anatase phase of TiO_2, "B" refers to α-Al_2O_3.

4.3.2   Photocatalytic activity

UV energy can degrade some compounds due to photolysis reactions, even in absence of photocatalysts. Thus, to prove the MB solution discoloration is due to photocatalysis, experiments in the absence of membranes in the MB-containing solution were carried out before the photocatalytic experiments. MB photolysis degradation was lower than 2% under

the experimental conditions used in this study. Photocatalytic tests showed photocatalytic active layers were produced. While for bare membranes less than 2% MB removal (due to photolysis) was achieved, this amount was much higher - 21 and 26% - for MS-50 nm and MS-200 nm membranes, respectively. It is also worth mentioning that an increase of 4x on TiO_2 layer thickness led to only a 4% improvement in MB removal efficiency. The small increase in MB removal can be explained by the fact that photocatalysis is a surface phenomenon that requires surface irradiation [26]. It has been shown that the light can penetrate deep and activate TiO_2 when the layer is very thin. Using a radiant flux of 3.48 mW cm^{-2}, photo-generated electrons and holes were formed mainly on TiO_2 films with a surface depth of around 30 nm. A further increase of the TiO_2 film thickness had a minor influence on photocatalytic activity [20].

4.3.3 Methylene Blue filtration

MS-400 nm and MS-200 nm membranes were used in the first and second sets of filtration experiments, respectively. When comparing the thicker membrane (Fig. 4.6a) to the second one (Fig. 6b), the permeation flux was significantly lower. The higher flux is due to the thinner coating layers on MS-200 nm, which reduces flux resistance. Despite that, the membrane MS-400 nm demonstrated high MB selectivity, removing approximately 86 % of MB from the permeate. In the MS-200 nm, membrane selectivity fell to 66.5 % MB elimination, a 20 % reduction in selectivity.

Flux decline along filtration experiments for both MS-400 nm (Fig. 4.6a) and MS-200 nm (Fig. 4.6b) membranes are attributed to fouling formation. Fouling can be formed on the membrane surface or inside the pores, depending on the fouling mechanism as described by Hermia's law [46]. A fouling layer on a membrane surface is called cake and may happen regardless of the formation of fouling inside the pores. The main influence on fouling in the pores is the ratio between pore and pollutant size. Membranes with smaller relative pore sizes present higher selectivity and are more likely to foul only or mainly at the surface. Since fouling is a normal phenomenon in membrane processes, cleaning pause procedures are necessary. Thus, physical cleaning, chemical cleaning or both combined have been applied for this purpose, where irreversible residual contamination is still to be expected. [47].
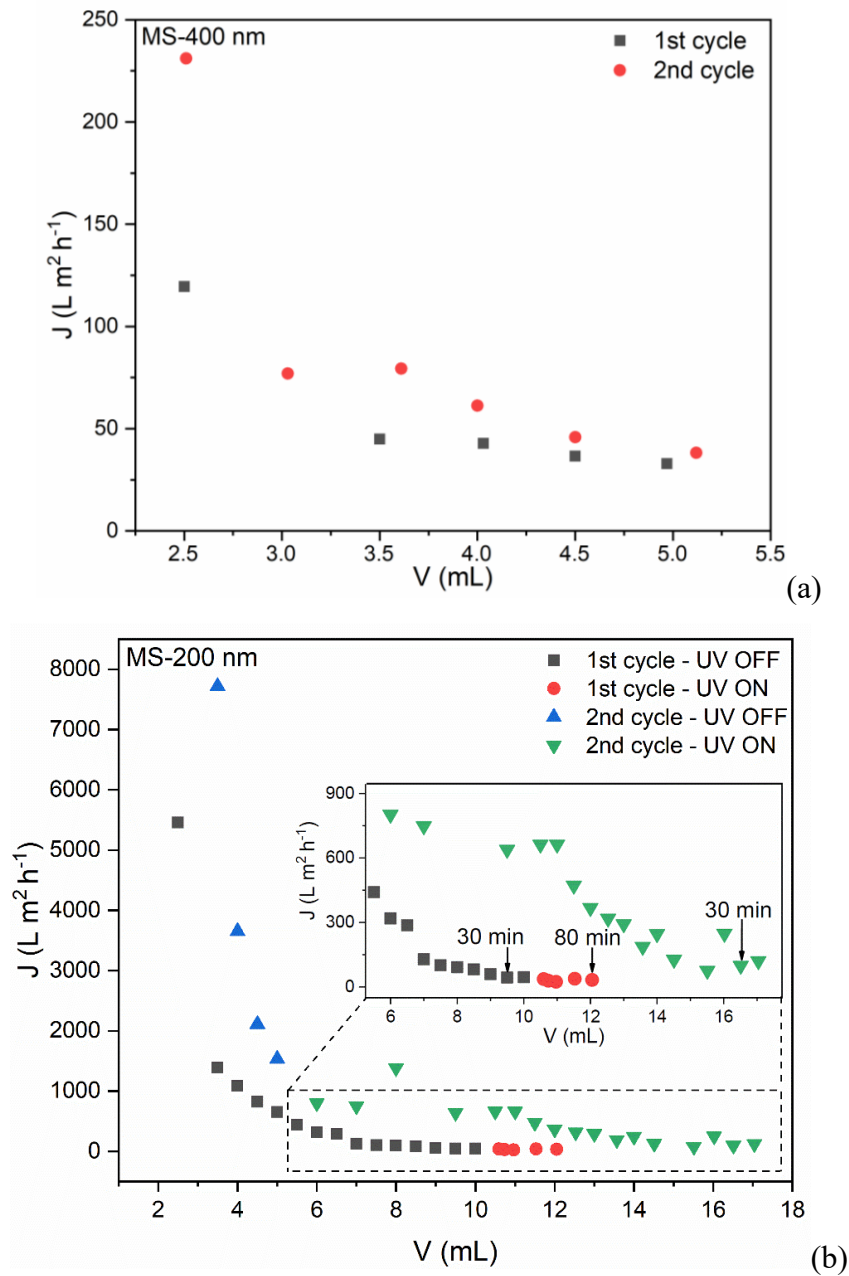
Figure 4.6 Permeate flux and the respective permeate volumes for (a) MS-400 nm and (b) MS-200 nm (insert with a zoom between 5.5 and 18 mL) membranes during filtration of a methylene blue solution 3.2 mg L^{-1} under 0.3 MPa for two filtration cycles, with an interval of 15 h under UV.

Membranes containing photocatalytic surfaces under suitable radiation have been reported to improve membrane cleaning performance and reduce irreversible fouling without the necessity of adding chemicals [48,49]. In this work, membranes were capable of completely recovering MB flux after UV treatment (15 h interval under UV after the 1st filtration cycle) and the second cycle showed a similar behavior compared to the 1st cycle (Fig. 6a and Fig. 6b).

Since the module was kept filled during the 15-hour UV irradiation, the higher initial flux values for the second cycle can be due to a slightly lower concentration of the MB solution within the module at the start of the second cycle. It should be noted that only the surface of the membranes produced contains photocatalyst, which means that only surface fouling can be photocatalytically decomposed under UV irradiation. The complete recovery of flux for both membranes indicates that fouling has formed mainly on the membrane surface.

The 1st cycle using MS-200 nm was performed without UV light for the first 10 mL permeate (45 min), after which the flux rate was already very low (Fig. 4.6b – 1st cycle – UV OFF). Next, UV light was switched on and flux was recorded for a further 30 min (around 2 mL of permeate). Nonetheless, in contrast to the 15 h UV treatment, no increment in the flux J was observed during this period (Fig. 4.6b – 1st cycle – UV ON). Since photocatalysis is a surface reaction, an excess of foulant will slow down the reaction rate by preventing light from reaching the membrane surface. To investigate this influence, the UV light was turned on earlier for the second filtration cycle, after a permeation volume of 5 mL had been achieved. Up to a permeate volume of 10 mL permeation, a slight flux recovery was observed, with a flux drop rate attenuation. The oscillation of the flux during the UV irradiation period (inset in Fig. 4.6b) was attributed to the fouling degradation reactions, which almost doubled the permeation volume in the same time range. After a certain period, the UV light could no longer maintain or reduce the flux drop during filtration (Fig. 4.6b). This can happen when the deposition rate of the fouling solutes on the membrane surface is faster than the degradation reaction [50]. In this context, surface fouling deposition can extend operation periods between cleaning intervals when optimized conditions are used.

4.3.4 Oily emulsion filtration

The membrane with the thinner titania layer, MS-50 nm, possesses an average pore size suitable only for microfiltration. Oily wastewater is an important global issue and its treatment by photocatalysis, micro, and ultra-filtration treatment have received increasing interest, while the application of photocatalytic membrane for this purpose is still scarce [9,17,29,42,51–57]. Thus, filtration of a soybean oil emulsion (1 g L^{-1}) at 0.1 MPa was chosen as the target pollutant to evaluate this membrane.

Three samples were collected after 15, 25, and 35 mL permeate, respectively. After the first sampling, UV light was turned on (Fig. 4.7). At the end of the experiment, an overall TOC removal of 60% was achieved, while turbidity removal was 85.5, 95, and 96% for the first, second, and third sampling, respectively. Turbidity removal increases were attributed to pore narrowing due to the deposition of foulants on the membrane or inside the pores. [58] Despite the retention (TOC removal) results, no flux recovery or flux drop rate attenuation was observed during the experiments with oily wastewater under UV (Fig. 4.7). Also, differently from the MB filtration experiments, no flux recovery was observed after the 15 h UV interval under UV. To confirm this effect, the membrane module was again kept overnight under UV irradiation at ambient pressure to provide long-term irradiation on the membrane surface. Still, no flux recovery was observed. For this reason, it was not possible to perform a 2nd filtration cycle in this case.
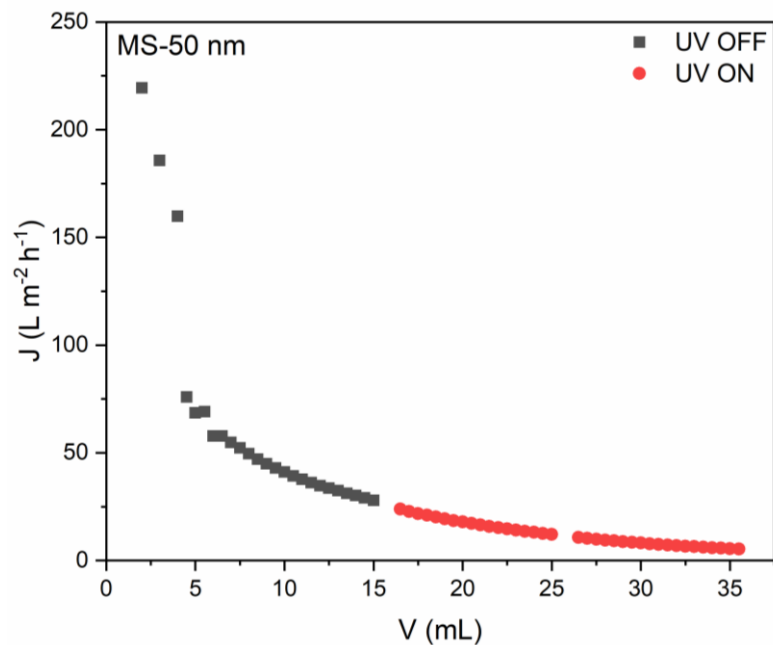
Figure 4.7 Permeate flux and the respective permeate volumes for MS-50 nm during a 1 g L^{-1} oily emulsion filtration at 0.1 MPa.

The lack of flux recovery is driven by two main factors. Firstly, the membrane has separated 60% of the feed oil. This means that some of the oil has passed through the membrane pores and deposited inside the pores. Although batch photocatalyst tests (Section 4.3.2) have shown similar photocatalytic capabilities for MS-50 nm and MS-200 nm membranes, the photocatalytic surface layer of the membrane is not able to decompose fouling inside the pores.

In this case, the question arises as to the pore size of the membrane, whereby filtration performance could be improved by using a bare membrane with narrower pore sizes (improving selectivity), while 50 nm coating layer can solely play the role of surface functionalization (photocatalysis). Secondly, photocatalysis is a surface reaction. Thick layers of foulant compounds deposited on the membrane surface during the filtration can hinder the proper irradiation of the photocatalytic surface. Also, if the degradation mechanism is indirect oxidation (OH^- and O_2^-) and the TiO_2 layer is completely insulated with oil, the radical formation can be hindered by the lack of sufficient oxygen on the membrane surface [29,59]. A membrane module equipped with more intense light irradiation could improve the photocatalytic reaction rate to a certain degree, which could improve the antifouling properties of the membrane and increase the duration of the filtration cycle [50,60].

4.4   CONCLUSIONS

Photocatalytic ceramic membranes suitable for micro- or ultrafiltration processes with tailored surface porosity and using a UV light for MB removal were produced by TiO_2 deposition by magnetron sputtering. High selectivity and self-cleaning properties were obtained. An anatase coating layer was formed on the membrane surfaces and the coating thickness was a major influence on selectivity, but a minor effect on photocatalytic activity. Only 4% more MB removal was obtained when the TiO_2 coating layer was increased by 4 times (from 50 to 200 nm). Higher flux can be obtained in the early presence of UV light, while the light has a little online effect on flux when a thick fouling layer has been formed. An extended UV exposure was able to recover the MB flux. Under the conditions used, degradation of soybean oil could not be observed. Further investigation is required to improve the antifouling properties for oily wastewater filtration. Finally, magnetron sputtering is a versatile technique, future work can also involve the deposition of different photocatalysts to produce active layers under visible light.

4.5   REFERENCES

[1]   M. Kamali, D.P. Suhas, M.E. Costa, I. Capela, T.M. Aminabhavi, Sustainability considerations in membrane-based technologies for industrial effluents treatment, Chem. Eng. J. (2019). https://doi.org/10.1016/j.cej.2019.02.075.

[2]   S.P. Dharupaneedi, S.K. Nataraj, M. Nadagouda, K.R. Reddy, S.S. Shukla, T.M. Aminabhavi, Membrane-based separation of potential emerging pollutants, Sep. Purif. Technol. 210 (2019) 850–866. https://doi.org/10.1016/j.seppur.2018.09.003.

[3]   S. Leong, A. Razmjou, K. Wang, K. Hapgood, X. Zhang, H. Wang, TiO2 based photocatalytic membranes: A review, J. Memb. Sci., 472 (2014) 167–184. http://dx.doi.org/10.1016/j.memsci.2014.08.016.

[4]   G. Mustafa, K. Wyns, A. Buekenhoudt, V. Meynen, Antifouling grafting of ceramic membranes validated in a variety of challenging wastewaters, Water Res. 104 (2016) 242–253. https://doi.org/10.1016/j.watres.2016.07.057.

[5]   R. Molinari, C. Lavorato, P. Argurio, Recent progress of photocatalytic membrane reactors in water treatment and in synthesis of organic compounds. A review, Catal. Today. 281 (2017) 144–164. http://dx.doi.org/10.1016/j.cej.2015.03.120.

[6]   L.T. Nyamutswa, B. Zhu, S.F. Collins, D. Navaratna, M.C. Duke, Light conducting photocatalytic membrane for chemical-free fouling control in water treatment, J. Memb. Sci. 604 (2020) 118018. https://doi.org/10.1016/j.memsci.2020.118018.

[7]   M. Padaki, R.S. Murali, M.S. Abdullah, N. Misdan, A. Moslehyani, M.A. Kassim, N. Hilal, A.F. Ismail, Membrane technology enhancement in oil-in-water separation: a review, Des. 357 (2015) 197–207. https://doi.org/10.1016/j.desal.2014.11.023.

[8]   C. Byrne, G. Subramanian, S.C. Pillai, Recent advances in photocatalysis for environmental applications, J. Environ. Chem. Eng. 6 (2018) 3531–3555. https://doi.org/10.1016/j.jece.2017.07.080.

[9]   P.C. Silva, N.P. Ferraz, E.A. Perpetuo, Y.J.O. Asencios, Treatment of oil produced water using advanced oxidative processes: Heterogeneous-photocatalysis and photo-Fenton,

Environ. Div. 2018 - Core Program. Area 2018 AIChE Annu. Meet. 4 (2018) 35–37. https://doi.org/10.12957/jse.2019.40991.

[10] D. Ma, H. Yi, C. Lai, X. Liu, X. Huo, Z. An, L. Li, Y. Fu, B. Li, M. Zhang, L. Qin, S. Liu, L. Yang, Critical review of advanced oxidation processes in organic wastewater treatment, Chemosphere. 275 (2021) 130104. https://doi.org/10.1016/j.chemosphere.2021.130104.

[11] X. Chen, Y. Hu, Z. Xie, H. Wang, Materials and Design of Photocatalytic Membranes, Elsevier Inc., 2018. https://doi.org/10.1016/B978-0-12-813549-5.00003-7.

[12] S. Samsami, M. Mohamadi, M.H. Sarrafzadeh, E.R. Rene, M. Firoozbahr, Recent advances in the treatment of dye-containing wastewater from textile industries: Overview and perspectives, Process Saf. Environ. Prot. 143 (2020) 138–163. https://doi.org/10.1016/j.psep.2020.05.034.

[13] N. Nasrollahi, L. Ghalamchi, V. Vatanpour, A. Khataee, Photocatalytic-membrane technology: a critical review for membrane fouling mitigation, J. Ind. Eng. Chem. 93 (2020) 101–116. https://doi.org/10.1016/j.jiec.2020.09.031.

[14] S. Mozia, Photocatalytic membrane reactors (PMRs) in water and wastewater treatment. A review, Sep. Purif. Technol. 73 (2010) 71–91. https://doi.org/10.1016/j.seppur.2010.03.021.

[15] M. Lee, Z. Wu, K. Li, Advances in ceramic membranes for water treatment, 2015. https://doi.org/10.1016/B978-1-78242-121-4.00002-2.

[16] N.F.D. Junaidi, N.H. Othman, N.S. Fuzil, M.S. Mat Shayuti, N.H. Alias, M.Z. Shahruddin, F. Marpani, W.J. Lau, A.F. Ismail, N.F.D. Aba, Recent development of graphene oxide-based membranes for oil-in-water separation: A review, Sep. Purif. Technol. 258 (2021) 118000. https://doi.org/10.1016/j.seppur.2020.118000.

[17] D. Zhang, G. Wang, S. Zhi, K. Xu, L. Zhu, W. Li, Z. Zeng, Q. Xue, Superhydrophilicity and underwater superoleophobicity TiO2 /Al2O3 composite membrane with ultralow oil adhesion for highly efficient oil-in-water emulsions separation, Appl. Surf. Sci. 458 (2018) 157–165. https://doi.org/10.1016/j.apsusc.2018.07.052.

[18]   I. Horovitz, I. Horovitz, V. Gitis, D. Avisar, H. Mamane, Ceramic-based photocatalytic membrane reactors for water treatment - Where to next?, Rev. Chem. Eng. 36 (2020) 593–622. https://doi.org/10.1515/revce-2018-0036.

[19]   S. Riaz, S.J. Park, An overview of TiO2-based photocatalytic membrane reactors for water and wastewater treatments, J. Ind. Eng. Chem. 84 (2020) 23–41. https://doi.org/10.1016/j.jiec.2019.12.021.

[20]   H. Choi, E. Stathatos, D.D. Dionysiou, Sol-gel preparation of mesoporous photocatalytic TiO2 films and TiO2/Al2O3 composite membranes for environmental applications, Appl. Catal. B Environ. 63 (2006) 60–67. https://doi.org/10.1016/j.apcatb.2005.09.012.

[21]   S.M. Samaei, S. Gato-Trinidad, A. Altaee, The application of pressure-driven ceramic membrane technology for the treatment of industrial wastewaters – A review, Sep. Purif. Technol. 200 (2018) 198–220. https://doi.org/10.1016/j.seppur.2018.02.041.

[22]   M.N. Subramaniam, P. Goh, W. Lau, B. Ng, Chapter 3 - Development of nanomaterial-based photocatalytic membrane for organic pollutants removal, Elsevier Inc., 2019. https://doi.org/10.1016/B978-0-12-814503-6.00003-3.

[23]   T. Yang, F. Liu, H. Xiong, Q. Yang, F. Chen, C. Zhan, Fouling process and anti-fouling mechanisms of dynamic membrane assisted by photocatalytic oxidation under sub-critical fluxes, Chinese J. Chem. Eng. 27 (2019) 1798–1806. https://doi.org/10.1016/j.cjche.2018.10.019.

[24]   A. Moslehyani, S.K. Hubadillah, M. Hafiz, D. Othman, A.F. Ismail, T. Matsuura, Contaminants: Water and Wastewater Treatment, (2018) 189–208.

[25]   L. Chen, P. Xu, H. Wang, Photocatalytic membrane reactors for produced water treatment and reuse: Fundamentals, affecting factors, rational design, and evaluation metrics, J. Hazard. Mater. 424 (2022) 127493. https://doi.org/10.1016/j.jhazmat.2021.127493.

[26]   A. Fujishima, X. Zhang, D.A. Tryk, TiO2 photocatalysis and related surface phenomena, Surf. Sci. Rep. 63 (2008) 515–582. https://doi.org/10.1016/j.surfrep.2008.10.001.

[27]   C.P. Athanasekou, N.G. Moustakas, S. Morales-Torres, L.M. Pastrana-Martínez, J.L. Figueiredo, J.L. Faria, A.M.T. Silva, J.M. Dona-Rodriguez, G.E. Romanos, P. Falaras,

Ceramic photocatalytic membranes for water filtration under UV and visible light, Appl. Catal. B Environ. 178 (2014) 12–19. https://doi.org/10.1016/j.apcatb.2014.11.021.

[28]   N.E. Salim, J. Jaafar, A.F. Ismail, M.H.D. Othman, M.A. Rahman, N. Yusof, M. Qtaishat, T. Matsuura, F. Aziz, W.N.W. Salleh, Preparation and characterization of hydrophilic surface modifier macromolecule modified poly (ether sulfone) photocatalytic membrane for phenol removal, Chem. Eng. J. 335 (2018) 236–247. https://doi.org/10.1016/j.cej.2017.10.147.c

[29]   A. Golshenas, Z. Sadeghian, S.N. Ashrafizadeh, Performance evaluation of a ceramic-based photocatalytic membrane reactor for treatment of oily wastewater, J. Water Process Eng. 36 (2020) 101186. https://doi.org/10.1016/j.jwpe.2020.101186.

[30]   H. Salazar, P.M. Martins, B. Santos, M.M. Fernandes, A. Reizabal, V. Sebastián, G. Botelho, C.J. Tavares, J.L. Vilas-Vilela, S. Lanceros-Mendez, Photocatalytic and antimicrobial multifunctional nanocomposite membranes for emerging pollutants water treatment applications, Chemosphere. 250 (2020). https://doi.org/10.1016/j.chemosphere.2020.126299.

[31]   Y.X. Li, P. Li, Y.Z. Wu, Z.L. Xu, M.L. Huang, Preparation and antifouling performance of thin inorganic ultrafiltration membrane via assisted sol-gel method with different composition of dual additives, Ceram. Int. (2020). https://doi.org/10.1016/j.ceramint.2020.09.056.

[32]   B.J. Starr, V. V. Tarabara, M. Zhou, S. Roualdès, A. Ayral, Coating porous membranes with a photocatalyst: Comparison of LbL self-assembly and plasma-enhanced CVD techniques, J. Memb. Sci. 514 (2016) 340–349. https://doi.org/10.1016/j.memsci.2016.04.050.

[33]   S. Sanches, C. Nunes, P.C. Passarinho, F.C. Ferreira, V.J. Pereira, J.G. Crespo, Development of photocatalytic titanium dioxide membranes for degradation of recalcitrant compounds, J. Chem. Technol. Biotechnol. 92 (2017) 1727–1737. https://doi.org/10.1002/jctb.5172.

[34]   P.J. Kelly, R.D. Arnell, Magnetron sputtering: a review of recent developments and applications, 56 (2000) 159–172. https://doi.org/10.1016/S0042-207X(99)00189-X.

[35]   M. Ratova, P.J. Kelly, G.T. West, X. Xia, Y. Gao, deposition of visible light active photocatalytic bismuth molybdate thin films by reactive magnetron sputtering, (2016). https://doi.org/10.3390/ma9020067.

[36]   S. Khamseh, F. Abdollahzadeh Davani, A. Samimi, The effects of RF-sputtered TiO2 top layer on pore structure of composite ceramic membranes, Surf. Coatings Technol. 258 (2014) 1256–1258. https://doi.org/10.1016/j.surfcoat.2014.07.014.

[37]   R. Bergamasco, F.V. da Silva, F.S. Arakawa, N.U. Yamaguchi, M.H.M. Reis, C.J. Tavares, M.T.P.S. de Amorim, C.R.G. Tavares, Drinking water treatment in a gravimetric flow system with TiO2 coated membranes, Chem. Eng. J. 174 (2011) 102–109. https://doi.org/10.1016/j.cej.2011.08.056.

[38]   L.L. Coelho, M. Di Luccio, D. Hotza, R. de Fátima Peralta Muniz Moreira, A.C. Moreira, C.P. Fernandes, K. Rezwan, M. Wilhelm, Tailoring asymmetric Al2O3 membranes by combining tape casting and phase inversion, J. Memb. Sci. 623 (2021) 119056. https://doi.org/10.1016/j.memsci.2021.119056.

[39]   J. Sakaliuniene, B. Abakevičiene, K. Šlapikas, S. Tamulevičius, Influence of magnetron sputtering deposition conditions and thermal treatment on properties of platinum thin films for positive electrode-electrolyte-negative electrode structure, Thin Solid Films. 594 (2015) 101–108. https://doi.org/10.1016/j.tsf.2015.10.016.

[40]   M.A. Henderson, A surface science perspective on TiO2 photocatalysis, 66 (2011) 185–297. https://doi.org/10.1016/j.surfrep.2011.01.001.

[41]   S. Huang, R.H.A. Ras, X. Tian, Antifouling membranes for oily wastewater treatment: Interplay between wetting and membrane fouling, Curr. Opin. Colloid Interface Sci. 36 (2018) 90–109. https://doi.org/10.1016/j.cocis.2018.02.002.

[42]   A. Moslehyani, M. Mobaraki, T. Matsuura, A.F. Ismail, M.H.D. Othman, M.N.K. Chowdhury, Novel green hybrid processes for oily water photooxidation and purification from merchant ship, Desalination. 391 (2016) 98–104. https://doi.org/10.1016/j.desal.2016.01.003.

[43]   C. Li, Z. Lu, X. Ao, W. Sun, X. Huang, Degradation kinetics and removal efficiencies of pharmaceuticals by photocatalytic ceramic membranes using ultraviolet light-emitting diodes, Chem. Eng. J. 427 (2022) 130828. https://doi.org/10.1016/j.cej.2021.130828.

[44]   N.T. Padmanabhan, H. John, Titanium dioxide based self-cleaning smart surfaces: A short review, J. Environ. Chem. Eng. 8 (2020) 104211. https://doi.org/10.1016/j.jece.2020.104211.

[45]   J. Hu, Y. Zhan, G. Zhang, Q. Feng, W. Yang, Y.H. Chiao, S. Zhang, A. Sun, Durable and super-hydrophilic/underwater super-oleophobic two-dimensional MXene composite lamellar membrane with photocatalytic self-cleaning property for efficient oil/water separation in harsh environments, J. Memb. Sci. 637 (2021) 119627. https://doi.org/10.1016/j.memsci.2021.119627.

[46]   W. Zhang, L. Ding, Investigation of membrane fouling mechanisms using blocking models in the case of shear-enhanced ultrafiltration, Sep. Purif. Technol. 141 (2015) 160–169. https://doi.org/10.1016/j.seppur.2014.11.041.

[47]   W. He, H. Huang, J. fen Gao, L. Winnubst, C. sheng Chen, Phase-inversion tape casting and oxygen permeation properties of supported ceramic membranes, J. Memb. Sci. 452 (2014) 294–299. https://doi.org/10.1016/j.memsci.2013.09.063.

[48]   Y. Shi, J. Huang, G. Zeng, W. Cheng, J. Hu, Photocatalytic membrane in water purification: is it stepping closer to be driven by visible light?, J. Memb. Sci. 584 (2019) 364–392. https://doi.org/10.1016/j.memsci.2019.04.078.

[49]   E.N. Santos, Á. Ágoston, S. Kertész, C. Hodúr, Z. László, Z. Pap, Z. Kása, T. Alapi, S.A.G. Krishnan, G. Arthanareeswaran, K. Hernadi, G. Veréb, Investigation of the applicability of TiO2, BiVO4, and WO3 nanomaterials for advanced photocatalytic membranes used for oil-in-water emulsion separation, Asia-Pacific J. Chem. Eng. 15 (2020) 1–15. https://doi.org/10.1002/apj.2549.

[50]   W. Zhang, L. Ding, J. Luo, M.Y. Jaffrin, B. Tang, Membrane fouling in photocatalytic membrane reactors (PMRs) for water and wastewater treatment: A critical review, Chem. Eng. J. 302 (2016) 446–458. https://doi.org/10.1016/j.cej.2016.05.071.

[51] L. Zhu, M. Chen, Y. Dong, C.Y. Tang, A. Huang, A low-cost mullite-titania composite ceramic hollow fiber microfiltration membrane for highly efficient separation of oil-in-water emulsion, Water Res. 90 (2016) 277–285. https://doi.org/10.1016/J.WATRES.2015.12.035.

[52] P. Monash, G. Pugazhenthi, Effect of TiO2 addition on the fabrication of ceramic membrane supports: A study on the separation of oil droplets and bovine serum albumin (BSA) from its solution, Desalination. 279 (2011) 104–114. https://doi.org/10.1016/j.desal.2011.05.065.

[53] L. Yu, M. Kanezashi, H. Nagasawa, T. Tsuru, Phase inversion/sintering-induced porous ceramic microsheet membranes for high-quality separation of oily wastewater, J. Memb. Sci. 595 (2020) 117477. https://doi.org/10.1016/j.memsci.2019.117477.

[54] N. Yaacob, G.P. Sean, N.A.M. Nazri, A.F. Ismail, M.N. Zainol Abidin, M.N. Subramaniam, Simultaneous oily wastewater adsorption and photodegradation by ZrO2–TiO2 heterojunction photocatalysts, J. Water Process Eng. (2020) 101644. https://doi.org/10.1016/j.jwpe.2020.101644.

[55] M. D'Auria, L. Emanuele, R. Racioppi, V. Velluzzi, Photochemical degradation of crude oil: Comparison between direct irradiation, photocatalysis, and photocatalysis on zeolite, J. Hazard. Mater. 164 (2009) 32–38. https://doi.org/10.1016/j.jhazmat.2008.07.111.

[56] C.S. Ong, W.J. Lau, P.S. Goh, B.C. Ng, A.F. Ismail, Investigation of submerged membrane photocatalytic reactor (sMPR) operating parameters during oily wastewater treatment process, 353 (2014) 48–56. https://doi.org/10.1016/j.desal.2014.09.008.

[57] N.H. Alias, J. Jaafar, S. Samitsu, N. Yusof, M.H.D. Othman, M.A. Rahman, A.F. Ismail, F. Aziz, W.N.W. Salleh, N.H. Othman, Photocatalytic degradation of oilfield produced water using graphitic carbon nitride embedded in electrospun polyacrylonitrile nanofibers, Chemosphere. 204 (2018) 79–86. https://doi.org/10.1016/j.chemosphere.2018.04.033.

[58] E. Iritani, A review on modeling of pore-blocking behaviors of membranes during pressurized membrane filtration, Dry. Technol. 31 (2013) 146–162. https://doi.org/10.1080/07373937.2012.683123.

[59]   M. Grao, M. Ratova, C.C. Amorim, R.B.P. Marcelino, P. Kelly, Crystalline TiO2 supported on stainless steel mesh deposited in a one step process via pulsed DC magnetron sputtering for wastewater treatment applications, J. Mater. Res. Technol. 9 (2020) 5761–5773. https://doi.org/10.1016/j.jmrt.2020.03.101

[60]   J.M. Herrmann, Photocatalysis fundamentals revisited to avoid several misconceptions, Appl. Catal. B Environ. 99 (2010) 461–468. https://doi.org/10.1016/j.apcatb.2010.05.012.

5 PHOTOCATALYTIC AND ANTIFOULING PERFORMANCE OF TITANIA-COATED ALUMINA MEMBRANES

This chapter refers to the development of TiO_2 coated Al_2O_3 photocatalytic membranes by sol-gel dip-coating. This study meets the specific objectives described in section 1.1.2 - Chapter 5. Insights on coating properties and photocatalytic antifouling capabilities, as well as its influence on fouling mechanisms, were discussed and presented below.

5.1 INTRODUCTION

The membrane separation processes have become an important and increasing industrial technology for several applications and have emerged as a strategy to improve water and wastewater treatment when conventional processes cannot reach the desired efficiency [1–5]. Ceramic membranes possess superior chemical, mechanical and thermal stability over polymeric membranes and the market is expected to reach 3.1 billion USD by 2025 [5].

On the other hand, fouling is still the main concern regarding membrane separation processes (MSP). Together with the high costs of ceramic membranes, fouling hinders their wider application. The development of membranes with high permeability through microstructure engineering and antifouling capabilities can improve the membrane performance and extend its life span, resulting in higher economic viability. Various antifouling approaches have been investigated[5–7], including bioinspired surface design [8], surface patterning [9], and catalytic membranes in hybrid systems [10].

Photocatalysis is an Advanced Oxidative Process based on the activation of a photocatalyst by a suitable light source according to its bandgap, generating highly reactive radicals, such as hydroxyl ($\cdot OH$) and superoxide radicals ($\cdot O_2^-$) [11]. Heterogeneous photocatalysis is known for the possibility of degrading pollutants even refractory or low concentration compounds, such as emerging pollutants, which have become a global concern [12]. Photocatalytic reactors are usually operated on a laboratory scale using slurry systems, while catalysts powder recovery is an important limitation for the scale-up. Photocatalytic membranes can be produced by immobilizing photocatalysts into or onto the membrane surface, in a synergic behavior in comparison to the isolated processes [13]. TiO_2 is the most widely

studied photocatalyst because of its good stability, environmental friendliness, low cost, strong oxidation ability, and relatively low bandgap, although it is only active under UV light. Anatase is the most active phase, presenting a phase transition to rutile near 600 °C [14–16].

In this context, photocatalytic membranes (PM) have recently emerged as an alternative to overcome limitations related to membrane and photocatalysis processes. In photocatalytic reactors, the operational costs can be reduced through catalyst recovery as well as hindering catalyst loss with the use of immobilized catalysts. Concerning the membrane process, PMs can provide antifouling capabilities by decomposing organic foulants at the membrane surface during the filtration process, improving membrane performance when properly irradiated [17,18]. Furthermore, the permeation of wastewater through the membranes can increase the removal of organic pollutants compared to reactors containing immobilized photocatalysts with the surface flux without permeation, even in the case where the membranes cannot effectively retain the pollutants. The effect is attributed to the forced contact between irradiated photocatalytic surface and pollutant during the filtration process [19]. A similar strategy was used by Scaratti et al. [10] to decompose 1,4 dioxane during surface water filtration by catalytic CuO-coated membranes in an ozone/membrane hybrid system. Finally, some photocatalysts such as TiO_2 provide hydrophilicity to surfaces, which can produce antifouling capabilities by repelling hydrophobic compounds, such as oils [20].

Although different supports and photocatalysts have been reported for the photocatalytic membrane separation process applied to water treatment, literature results are still limited. Nevertheless, ceramic membranes are preferred for photocatalytic applications since polymer membranes may be damaged by UV irradiation. In turn, due to sintering steps, post functionalization with photocatalyst coating onto ceramic membranes is preferred. Coatings can be added by various methods, such as vacuum filtration, electro-spraying, dip-coating, deposition of gas-phase photocatalyst, and magnetron sputtering. [14,18,21]. By adjusting TiO_2 magnetron sputtered coating layers thickness, Coelho et al. [22] proved that is possible to produce a photocatalytic membrane with tailored pore sizes and selectivity. However, the control of pore size remains a challenge. Coating layers are frequently related to pore blockage, undesirably reducing membrane permeability when membranes with suitable pore sizes are used [23]. Furthermore, low catalyst adhesion on the membrane surface and defects, such as cracks, are challenges to be faced [24,25].

Sol-gel is one of the most traditional techniques for deposition of metal oxide thin films to a range of surfaces and presents several advantages such as low capital and operational costs, simplicity and possibility of tuning film porosity and thickness, production of surfaces high purity, homogeneity, excellent physical properties, enhanced area and high photocatalytic activity [14,26,27]. Sol-gel can be coated on the membrane surface by different techniques, such as spin-coating, drop-coating, and dip-coating. Although TiO_2 powder P25 is the most used photocatalyst for slurry applications, this material consists of nanoparticle aggregates, which hinder a homogeneous distribution in the membrane surface. For this reason, a TiO_2 sol-gel solution using a photocatalyst precursor such as titanium tetraisopropoxide or tetra-titanium(IV) tert-butoxide is commonly used [25,28], while the addition of TiO_2 powder on sol-gel containing TiO_2 precursor solution was also reported [24]. A sintering step is then used to produce the TiO_2 crystalline phase and improve catalyst adhesion.

Žerjav et al. [26] compared TiO_2 thin films deposited on soda-lime glasses by magnetron sputtering and spin-coating sol-gel, which were applied to the photocatalytic degradation of bisphenol A. Films produced by sol-gel were thinner (165-270 nm), more porous, and showed higher degradation than the films prepared by magnetron sputtering (500-530 nm). In both cases, pure anatase was formed. However, as TiO_2 is active only under UV irradiation, much effort in photocatalyst engineering has been done to produce photocatalysts active under visible light. One of the most common strategies is doping photocatalysts to reduce their bandgap or charge recombination. Žerjav et al. [26] added appropriate amounts of NH_4NO_3 or $Cu(NO_3)_2$ to the sol-gel aiming to obtain a single TiO_2 layer doped with 1.5% nitrogen or copper. Doping increased degradation under visible light, but reduced it under UV compared to pure TiO_2 coating layers. Furthermore, higher bisphenol removal was achieved when two 150 W lamps were used respectively as UV and visible light sources. Still, doping TiO_2 did not alter significantly the physical properties of produced films, although films thickness and rugosity were slightly reduced. Thus, TiO_2 coatings were successfully applied to membrane surfaces and their respective filtration performance can be further extended to optimized conditions using doped photocatalysts.

In this context, a facile route to produce photocatalytic TiO_2-coated Al_2O_3 by sol-gel dip-coating without modifying the original membrane morphology was investigated. The membranes were characterized using Scanning Electronic Microscopy, Raman spectroscopy, and X-ray diffraction. Membranes' photocatalytic activity was proved by the decolorization of

a methylene blue in a batch reactor. The membrane selectivity and antifouling capabilities were investigated for acetaminophen or oily wastewater filtration under different operational conditions. Finally, fouling modeling was used to investigate the fouling/antifouling mechanisms.

5.2 EXPERIMENTAL

5.2.1 Materials

Alpha-alumina (Almatis, CT3000, d50 ~ 0.4 µm), N-methyl-2-pyrrolidone (NMP, Sigma), polyethersulfone (PES, BASF Ultrason® E2010), and poly(ethylene glycol) (PEG, Sigma, BioUltra 35000) were used to produce an alumina slurry, and ultrapure water (Milli-Q system, Millipore) was chosen for the coagulation bath to produce the alumina green tape. Isopropanol (NEON), acetylacetone (NEON), titanium(IV) tert-butoxide (ALDRICH), and acetic acid (VETEC) were used to produce a sol-gel. Lubricating oil (Lubrax GL 5 90) and Sodium Dodecyl Sulfate (SDS) were used to produce synthetic oily wastewater. Methylene blue (LAFAN) and acetaminophen (SIGMA) were used to produce solutions as target dissolved pollutants.

5.2.2 Preparation of membranes

Flat alumina membranes (~ 16 mm x 16 mm x 0.7 mm) were produced as previously reported (Chapter 3) [29] by combining phase-inversion and tape casting. The slurry composition was set as 7%, 0.8%, 47.2%, and 45% of PES, PEG, NMP, and alumina powder respectively. The green tapes were debound at 2 °C min^{-1} from room temperature to 600 °C. After a dwell time of 2 h, the green tapes were sintered at 2 °C min^{-1} to 1400 °C and kept at the final temperature for 3 h. The membranes were cooled in the furnace down to room temperature.

The produced alumina membranes were functionalized with TiO_2 coating layers using a sol-gel dip-coating technique [30] to produce photocatalytic membranes. The procedure comprised three main steps as described in Fig. 5.1: (i) sol-gel preparation followed by (ii)membrane coating, and finally (iii) membrane sanding. Sol-gel was produced under vigorous

magnetic stirring. First, 0.61 mL acetylacetone was dropwise added to 69 mL of isopropanol to control the hydrolysis and condensation reactions, followed by the dropwise addition of 6 mL of Titanium (IV) tert-butoxide as TiO_2 precursor. After 30 min mixing, 6.86 mL of acetic acid was then dropwise added to the solution and mixed for a further 30 min resulting in a transparent yellowish sol-gel. Next, flat alumina microfiltration membranes (16 mm x 16 mm x 0.7 mm) were then dip-coated into sol-gel and left to dry at ambient temperature and then heat-treated at 2 min^{-1} °C from room temperature to 550 °C kept at the final temperature for 30 min in an air atmosphere to produce a TiO_2 coating layer. The membranes were cooled in the furnace down to room temperature. The process was repeated to produce membranes with 1, 2, or 3 coating layers. They were denoted as 1x, 2x, and 3x. Before filtration tests, membranes are sanded to produce disc membranes (1 cm diameter). TiO_2 added mass per layer was calculated.
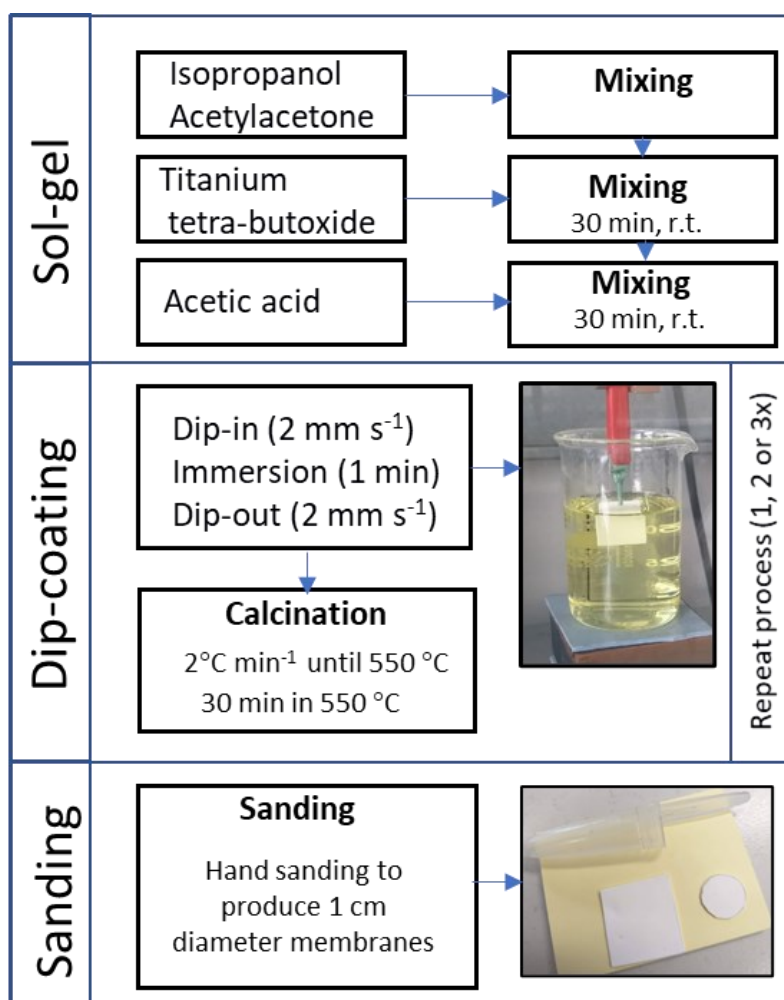

Figure 5.1 Process scheme of the preparation of membranes.

5.2.3 Morphological and chemical characterization

The sol-gel solution produced from alkoxide precursor requires a heat treatment for the decomposition of residual organic content and crystallization of the TiO_2 sol network to form the TiO_2 desired phases. For photocatalytic applications, anatase is preferred over rutile due to its higher photocatalytic activity. Phase transition is known to occur near 600 °C but may vary depending on the precursor. Given the complex decomposition process, thermogravimetric (TG) and differential thermal analysis (DTA) was conducted for the dry mixture from the sol-gel solution to support the selection of an appropriate calcination temperature. TG/DTA was performed in an STA 503 thermal analysis system from BÄHR Thermoanalyse GmbH up to 1050 °C with a heating rate of 2 °C min^{-1} and a flow rate of 2 L h^{-1} of Argon. The crystalline phases formed after sintering pure sol-gel powder at 550 °C and 600 °C were analyzed by X-ray diffraction (Shimadzu XRD 7000), Cu-Kα radiation (1.5409 Å), 2θ ranging from 10° to 80° in steps of 0.02° and a counting time per step of 2° min^{-1} X'pert High Score software (Malvern Panalytical) was used for phase quantification.

The microstructure of the cross-section and surface of the produced membranes were analyzed by Scanning Electron Microscopy (SEM, 20 kV; Series 2, Obducat CamScan; Supra 40-Carl Zeiss). Before the measurement, samples were sputtered with gold (K550, Emitech, Judges Scientific). TiO_2 formation on the membrane surface was confirmed by Raman spectroscopy (Anton Paar Cora 5200, 250 mW, 784 nm).

UV light is required to activate TiO2, which cannot be activated under visible light due to its bandgap. On the other hand, shorter wavelengths (such as $\lambda = 254$ nm – UVC) are known to result in high rates of photolysis. Thus, UV lamps with wavelength $\lambda = 365$ nm were chosen for photocatalytic experiments. The wavelength of the lamps provided by the suppliers indicates the peak emission. However, the lamps can emit a range of wavelengths as filters are not used. Radiant flux was not measured. Membrane photocatalytic activity was characterized in terms of methylene blue (MB) degradation under UV light (8 W) For the tests, MB saturated membranes were immersed for 8 h into beakers containing an MB solution (30 mL, 5 mg L^{-1}) under UV the light.

MB concentration was measured using a calibration curve in a UV-Vis spectrophotometer (HACH) at $\lambda = 665$ nm. The percentage of MB removal (%MB removal)

was calculated as described in Equation 1, where C_0 and C are the initial and final MB concentrations, respectively.

$$\%MB\ removal = \left(1 - \frac{C}{C_0}\right)$$
(1)

5.2.4 Filtration performance

All filtration and permeation experiments were performed using a custom-made filtration apparatus (Fig. 5.2) equipped with a 10 W UV LED ($\lambda = 365$ nm) placed 7 cm above the membrane surface. Permeate was collected in a beaker on an electronic balanced coupled with a customized data acquisition system. Permeate flux was calculated using (L m^{-2} h^{-1}) along with the experiments according to Equation 2, where V (L) is the volume permeated in a period t (h) through a membrane and A is the surface area A (m^2). Feed density was considered to be 1 g mL^{-1} regardless of the pollutant type since their concentration was low. Cross-flow mode with retentate recirculation and transmembrane pressure at 1 bar was applied for all the experiments.

$$J = \frac{1}{A} \cdot \frac{dV}{dt}$$
(2)

5.2.4.1 Water permeation flux

Water permeation was measured for bare and 1x, 2x and 3x coated membranes at 1 bar in dark conditions to evaluate the effect of TiO$_2$ coating on membrane permeability.

5.2.4.2 Light-induced antifouling properties

Antifouling capabilities of the produced membranes were investigated during the permeation of acetaminophen (1 mg L^{-1}) using 4 L of feed solution. Flux along filtration

experiment was calculated using Equation 2. Experiments were performed with and without UV light.
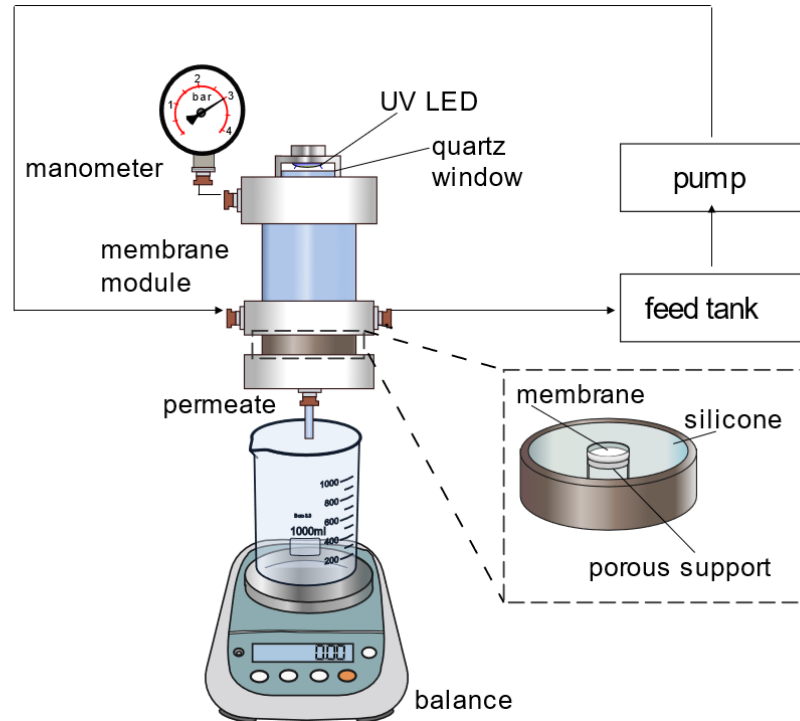

Figure 5.2 Membrane permeation module. Source: Coelho et al. [22].

5.2.4.3 *Oily wastewater filtration*

Oily wastewater filtration for SDS-stabilized emulsions containing 50, 100, and 250 ppm (1 L) of lubricating oil was performed under UV and in dark conditions. Emulsions with such low oil concentrations are reported to have low removal for traditional treatment methods. Furthermore, high oil loadings result in more serious fouling issues and lower photocatalytic activity. Thus, the selected oil concentration can be used as a target pollutant to simulate a polishing treatment and as a first attempt to evaluate the effectiveness of photocatalytic removal of oily fouling. Membrane flux was calculated according to Equation (2). Membranes' selectivity was evaluated through TOC removal (Equation 3), where TOC is the total organic carbon of the filtrate at the end of the experiment and TOC_0 refers to the feed emulsion TOC. For the analysis, 10 mL of each sample was used.

$$\%TOC\ removal = \left(1 - \frac{TOC}{TOC_0} \right).100\% \tag{3}$$

5.2.5 Fouling mechanisms and modeling

A fitting model based on Hermia's law (Equations 4 and 5) was applied to identify the effect of the photocatalytic coating on fouling mechanisms and plugging constant during the permeation of acetaminophen. A dynamic model was solved using the Euler method. The *SOLVER* tool from Microsoft Excel® was used to minimize the RSS by employing the generalized reduced gradient (GRG) nonlinear method (Equations 4 and 5).

$$\frac{dJ}{dt} = -K_n J^{3-n} \tag{4}$$

$$J = \frac{dv}{dt} \tag{5}$$

where J is the instantaneous filtration rate (m³/s), v is the cumulative filtrate volume collected per unit of membrane area (m³/m²), K_n is a plugging constant and n is the blocking index, i.e., a variable that characterizes the mechanism of the fouling model, with $n = 2$ for complete blocking, $n = 3/2$ for standard blocking, $n = 1$ for intermediate blocking, and $n = 0$ for cake filtration [31,32].

5.3   RESULTS AND DISCUSSION

5.3.1   Evaluation of coating sintering temperature

TGA and DTA analyses were conducted on the dry mixture from the sol-gel solution to support the selection of an appropriate calcination temperature (Fig 5.3). The endothermic peak at around 125 °C and corresponding ~7,5% weight loss refers to loss of water and organics loosely absorbed at the surface. Two big exothermic peaks are observed at approximately 360 °C and 510 °C respectively. The first happens due to volatilization and combustion of the

organic species and thus, is accompanied by intense mass loss. The second peak is accompanied by a minimum weight loss and suggests the formation of the anatase phase. A very discreet peak observed at around 750 °C may be related to the formation of the rutile phase. A total weight loss of around 45% was observed during the heat process.
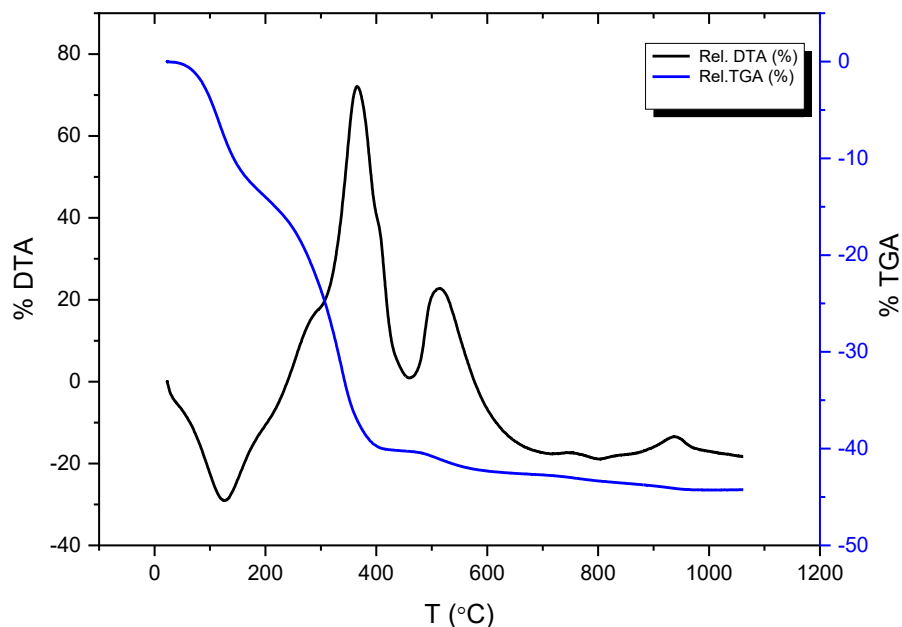

Figure 5.3 Thermogravimetric analysis (TGA) and differential thermal analysis (DTA) for the solids resulting from sol-gel after solvent evaporation.

XRD spectra (Fig. 5.4) showed the formation of anatase (100%) at 550 °C, resulting in the transformation of 10% to the rutile phase when the sintering temperature of 600 °C was used. Since the anatase phase is known to have higher photocatalytic activity than rutile and aims at superior economic and environmental viability, the temperature of 550 °C was chosen for sintering the coated membranes after the dip-coating.
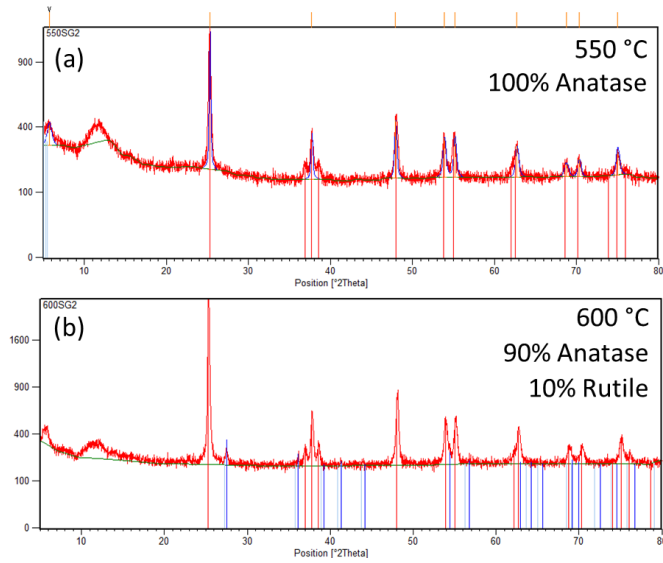
Figure 5.4 XRD spectra and phase quantification from sol-gel resulting powder after sintering process at (a) 550 °C and (b) 600 °C.

5.3.2 Morphological and chemical characterization of the coating membranes

Raman spectroscopy was used to confirm the formation of the anatase phase on the surface of the TiO_2 functionalized membrane after sintering at 550 °C for 1, 2 and 3 layers of TiO_2 added. The Raman spectra (Fig. 5.5) confirmed the presence of TiO_2 as the only titanium compound present (assign as "A"), in addition to the characteristic peaks of Al_2O_3 according to the spectrum observed for the bare membrane (assign as "B").
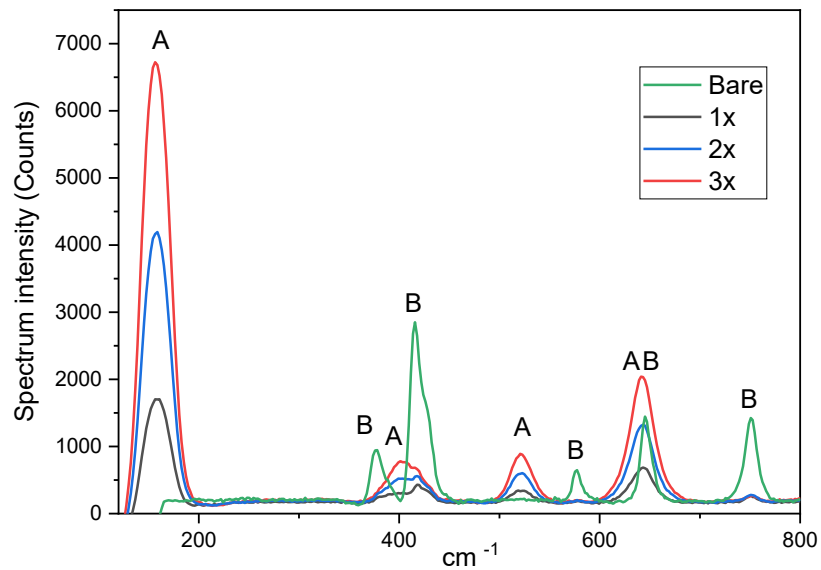

Figure 5.5 RAMAN analysis of the different membranes.

The mass of TiO_2 added per sol-gel layer was calculated (Table 5.1). The overcoating resulted in the addition of homogeneous layers of TiO_2, with ~1.7 mg of TiO_2 per layer for each membrane. This value corresponds to less than 0.7 mg TiO_2/cm^2, which is very low and in agreement with the SEM images of the surface of the coated membrane surfaces (Fig. 5.6). The images for bare, 1x, 2x, and 3x coated membranes demonstrated that the morphology of the membrane surface remained almost unaffected, without considerable changes in the membrane pore size, with a good distribution of TiO_2, without a new layer being identified. The low film thickness is attributed to the low viscosity of the TiO_2 sol [33].

Table 5.1 Added TiO_2 mass per layer.

| Number of layers	Mass of TiO_2 added (mg)	Mass of TiO_2 added per layer (mg)	Added TiO_2 mass per surface area (mg cm^{-2})
1	1.75±0.30	1.75	0.68
2	3.46±0.18	1.73	1.35
3	5.33±0.12	1.78	2.08

The photocatalytic activity for the produced membranes was proved through MB removal in batch systems for coated and bare membranes. MB removal due to photolysis in absence of membranes was also evaluated. TiO_2 coating considerably enhanced MB removal compared to bare membranes (Table 5.2). Photocatalytic membranes improved the %MB removal between 2.5 and 3 times under UV light compared to the bare membrane, confirming its photocatalytic activity.

Table 5.2 %MB removal under UV light (8h) in batch system.

Sample	% MB Removal
Photolysis	12%
Bare	19%
1x	52%
2x	48%
3x	57%
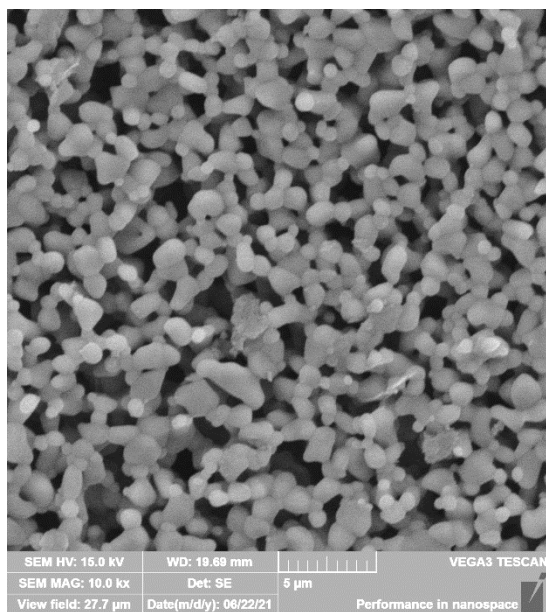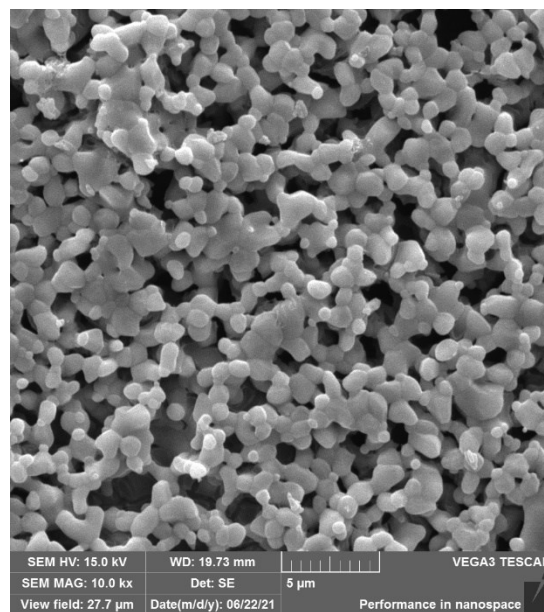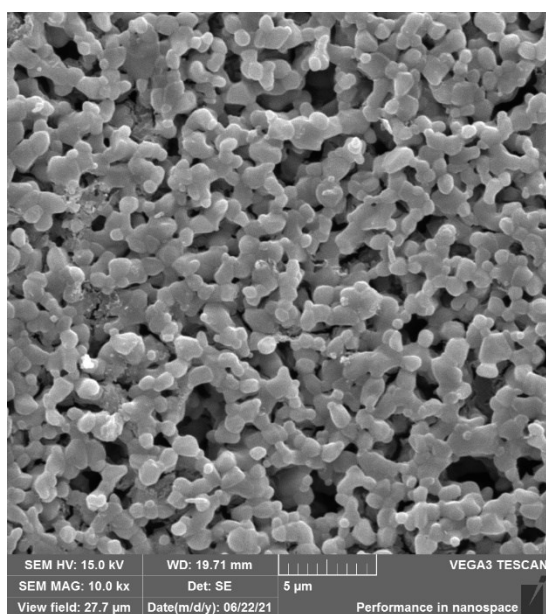
Figure 5.6 SEM images of membrane surfaces (10 kx magnification). (a) bare, (b) 1x, (c) 2x and (d) 3x coated membranes.

Increasing TiO$_2$ thickness increases the area available for chemical reactions while hindering the species diffusion through the porous matrix as well as the electron/hole transport. In addition, increasing TiO$_2$ films could increase the light attenuation through it. Based on it,

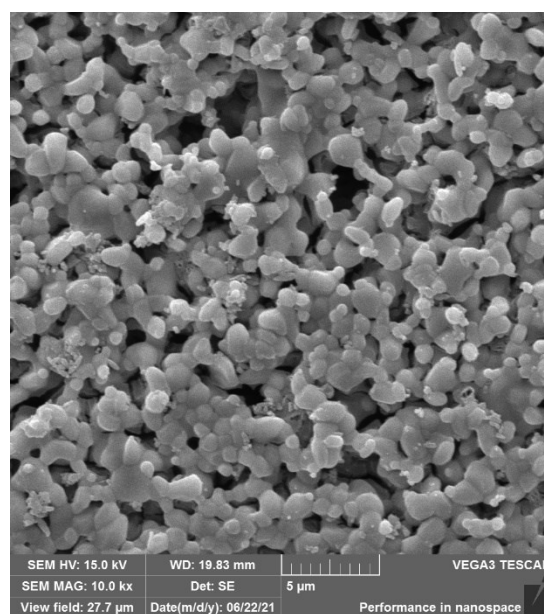an correlation to define optimal TiO_2 layer thickness has been proposed for immobilized photocatalytic reaction systems [34]. Nevertheless, for the tested conditions, slight changes in %MB removal seem not to be related to coating layers. The better photocatalytic performance was obtained for the 3x layer membranes. The same trend was observed for TiO_2-coated membranes produced by magnetron sputtering, as reported in Chapter 4 [22], where increasing TiO_2 coating thickness from 50 to 400 nm slightly improved photocatalytic activity.

5.3.3   Water flux

Coating layers did not significantly modify water permeance compared to the bare membranes (Fig. 5.7), which is an outstanding positive result. In turn,, water permeance losses due between 24 and 92% have been reported in the literature due to flux resistances added by TiO_2 photocatalytic coating layers [23].   Slight alterations observed in the flux during permeation experiments may be attributed to inherent differences in membrane morphology that may occur for porous materials even for materials produced in the same batch.
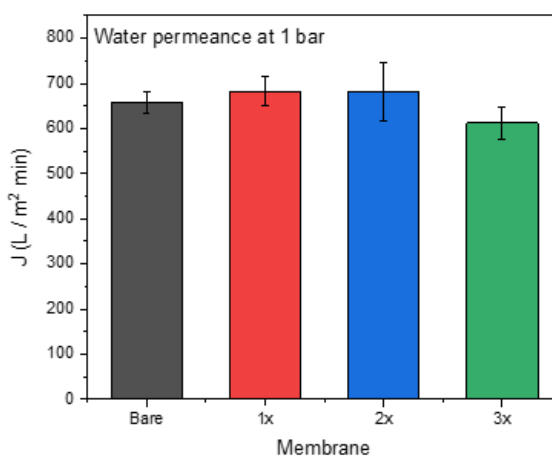
Figure 5.7 Water permeate flux at 1 bar for bare, and 1x, 2x, and 3x TiO_2 coated membranes.

5.3.4   Light-induced antifouling properties during the permeation of acetaminophen

Anti-fouling capability under UV light during permeation was for acetaminophen (1 mg L^{-1}) dissolved in an aqueous solution using bare and 3x coated membranes. Acetaminophen (molecular diameter of 0.285 nm) [35] was chosen as a model pharmaceutical compound.

Although the membranes produced possess a large average pore size (0.42 µm, as measured for the A45P7 membranes – Section 3.3.1) that precludes the considerable retention of acetaminophen, the compound is partially retained on the membrane, decreasing the permeate flux (Fig. 5.8a). The presence of UV or TiO_2 coating layer alone did not change the flux drop rate compared to the bare membrane (Fig. 5.8a). On the other hand, UV light reduced flux drop rate (Fig. 5.8a) and improved the permeate flux (and thus permeate volume) for the coated membrane (Fig. 5.8b). After 90 min filtration, a 2.4-fold increase on permeate volume for the PM under UV was obtained compared to the PM in the absence of light: around 1300 mL permeate volume was obtained for the 3x membrane ($A = 0.785$ cm^2), while only 545 mL permeate volume was obtained for the same membrane under dark conditions. Similar volume (~520 mL) was obtained for the bare membrane under UV, while only 347 mL were permeated using the bare membrane in the dark. When the traditional microfiltration using bare membrane in absence of light, the photocatalytic process resulted in a 3.7-fold increase in permeate volume for the same filtration period. The difference for bare membrane may be associated with light-induced hydrophilicity and photolysis in some instances.

Filtration experiments with alternate Dark/UV irradiation periods were performed (Fig. 5.8c). UV irradiation periods were able to slightly increase permeate flux in the first moment, followed by a flux drop rate similar to the filtration under constant UV irradiation. During dark periods, higher flux drop rates were observed. Flux drop under UV can be attributed to (i) fouling deposition inside membrane pores and (ii) faster deposition rate than the degradation reaction on the irradiated membrane surface. [36]. Thus, optimized membrane pores sizes and operation parameters, such as higher light power, could allow further process efficiency improvements.

Finally, filtration under UV irradiation increased the reversible fouling ratio, improving flux recovery after surface physical cleaning (Fig 5.8d). Although the change in the acetaminophen concentration was not possible to be measured using UV-vis spectrophotometry, the formation of intermediary compounds was confirmed by the surface color modification after permeation using photocatalytic membranes under UV. Fig. 5.9 shows TiO_2 coated membranes after the filtration of acetaminophen in the dark (left side) and under UV light (right side). After irradiation overnight, the greyish surface became white again, although slightly yellowish.
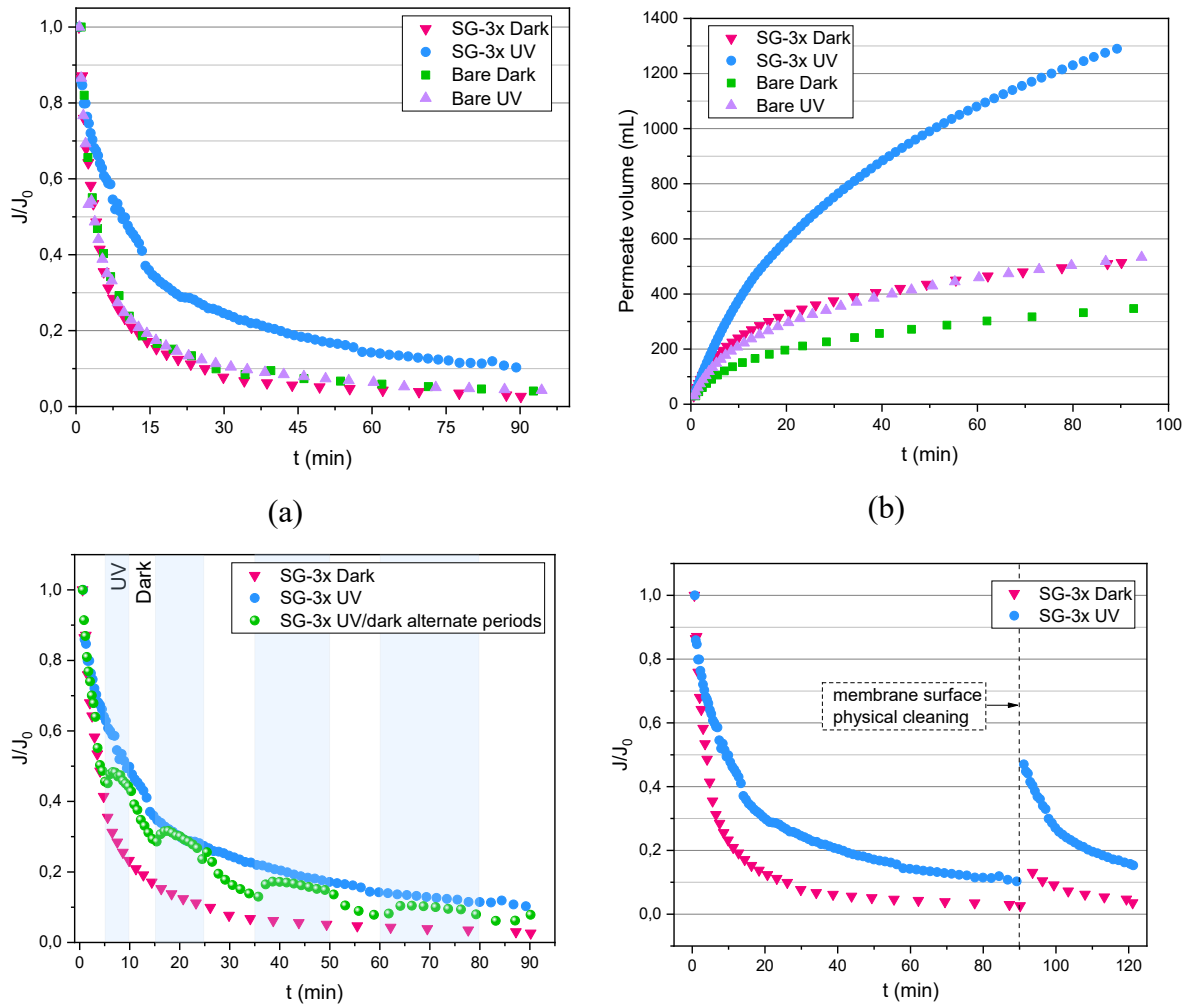
Figure 5.8 Light-induced antifouling properties during acetaminophen permeation: (a) relative flux and (b) permeate volume over filtration experiments for bare and PM membranes, under UV and in dark conditions; (c) relative flux for PM membrane in darkness, under UV and alternate UV/dark periods; (d) Flux recovery after physical cleaning for filtration under UV or dark.

Figure 5.9. PM membranes after filtration of acetaminophen, in dark conditions (white) and under UV (gray).

5.3.5 Oily wastewater filtration

Permeate flux over oily wastewater (250 ppm) filtration experiments for bare, 1x, 2x and 3x coating layered membranes were not modified by the coating layers (Fig. 5.10a). In turn, flux dropped faster as higher oil concentration was used (Fig. 5.10b), as expected due to the faster formation of fouling. UV light seems to have only slightly improved membrane flux for 50 and 100 ppm, considering that slight variations in flux for different membranes are also expected. Nevertheless, irrespective of membrane type (Bare, 1x, 2x, and 3x) and oil concentration, TOC removal between 77 and 87% was obtained. Additionally, wastewater appearance was considerably improved and translucid permeate was obtained (Fig. 5.11).

Flux was also not recovered after 24 h UV exposure. Surface SEM surface images of a fouled membrane (Fig. 5.12a) show a high level of fouling on the membrane surface, even after UV exposure. Although good photocatalytic activity has been proved (Table 5.2), oily wastewater is known by suffering serious fouling issues [37]. In the case of the photocatalytic surface, it is believed that the dense and thick oil layer hinders the photocatalytic surface activation by the UV source. High power lamps have been used to achieve a better photocatalytic response. Nevertheless, oily wastewater treatment by photocatalysis and mainly by photocatalytic membranes are still limited and need to be better understood. Membrane with specific features could improve PMs performance for oily wastewater. Investigation on this topic is still limited and, given its potential, further research on this topic is necessary.

On the other hand, as could be expected considering the membrane selectivity and large pore sizes, thick fouling was also formed inside membrane pores, as seen by the SEM image of the near-surface membrane cross-section (Fig. 5.12b). Photocatalysis is a surface reaction where the surface needs to be properly irradiated. In this case, it may not degrade compounds inside the membrane pores in dark conditions. Photocatalytic membrane performance for oily wastewater using the dip-coating strategy presented in this work needs to then be further tested for membranes with narrower surface pore sizes and higher power lamps. Finally, the produced membranes presented high permeability and could be used in polishing steps as pre-treatment for ultrafiltration processes.
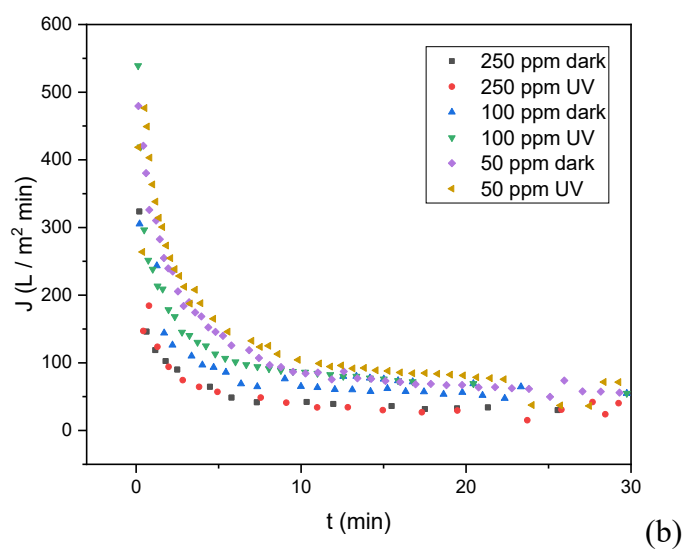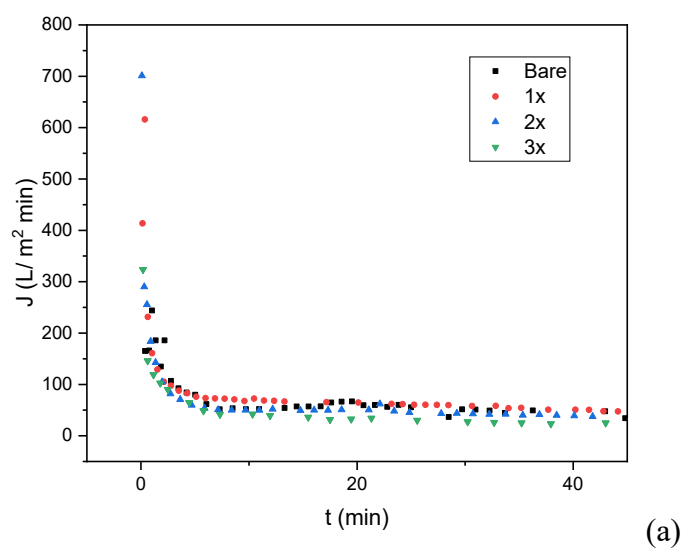
Figure 5.10 Permeate flux over the time for (a) 250 ppm oily wastewater filtration for bare, and 1x, 2x and 3x coated membranes in dark conditions and (b) 50, 100, and 250 ppm filtration experiments under UV and dark conditions using a 3x coated membrane.

Figure 5.11 Visual comparison between oily wastewater feed (250 ppm) and permeate.
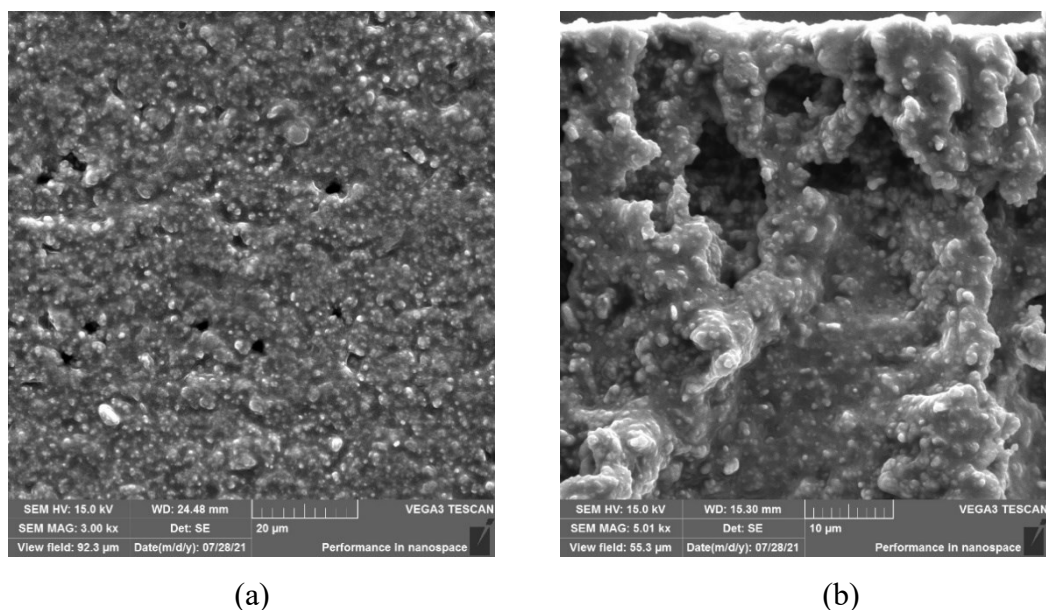
Figure 5.12 SEM images of the fouled membrane after filtration of lubricating oil filtration and after 24 h under UV exposure: (a) surface) and (b) cross-section.

5.3.6 Fouling and antifouling mechanisms

The fitting of experimental data to Hermia's models was performed for bare and 3x coated membranes, under UV and in dark conditions (Fig. 5.13). Intermediary fouling mechanisms (n=1) showed excellent fit for bare membranes under UV (Fig. 5.13a) and in dark conditions (Fig. 5.13b) and for 3x coated membrane under UV (Fig. 5.13c). In turn, a good fit for n=1 was also found for coated membrane in dark conditions (Fig. 5.13d), although the data fitting showed a similar fit for the pore constriction mechanisms, i.e., standard fouling (n = 3/2), which may be attributed to any surface heterogeneity. Both mechanisms indicate that membrane pores are not completely blocked by a single foulant molecule though.

Given the good fit of all experiments (Fig. 5.13e-f), intermediary fouling (n= 1) was used to compare the plugging constant, Kn (L^{-1}), for the four experiments (Table 5.3). For the same fouling mechanism, the plugging constant gives information regarding fouling severity. The photocatalytic membrane was able to reduce the plugging constant by over 74% for the filtration under UV light compared to the bare membrane in dark conditions, and by over 68% compared to the bare membrane for filtration under UV light. The slight decrease in the constant values for the PM in the dark or bare membrane under UV may be attributed to TiO_2

hydrophilicity and photolysis, respectively. Finally, it should be noted that, interestingly, the photocatalytic antifouling effect on the membrane surface did not alter the fouling mechanism or membrane fitting to Hermia's law during the filtration under UV (Fig. 5.13e), but reduced fouling by only reducing foulant loading on the membrane surface. This result differs from those found for catalytic membranes using an ozone-membrane hybrid system, where ozone homogeneous and heterogenous reactions separately contributed to modifying the fouling-antifouling dynamics [31].

Table 5.3 Plugging constants, Kn (L^{-1}) related to intermediary fouling (n=1) for bare and coated membranes, under UV and in dark conditions

Filtration experiment	Kn (n=1) [L^{-1}]
Bare (dark)	0.816
Bare (UV)	0.657
TiO$_2$ coated (dark)	0.538
TiO$_2$ coated (UV)	0.210

5.4 CONCLUSIONS

Photocatalytic membranes were produced by sol-gel dip-coating without modifying surface porosity. TiO$_2$ was homogenously spread onto the membrane surface without forming a new separate layer. In addition, repeating the coating process up to 3 times had only a slight effect on membrane properties.

Acetaminophen filtration (1 mg L^{-1}) using a photocatalytic membrane under UV light resulted in a 2.4 and 3.7-fold increase in the permeate volume when compared to the coated and uncoated membranes, respectively, in dark conditions. Intermediaries of acetaminophen degradation were visually observed on the membrane surface after the filtration process and further photocatalytic degraded by a light-induced cleaning step after filtration. Furthermore, fouling mechanisms modeling demonstrated that photocatalytic reactions on membrane surface did not change the fouling mechanism, but reduced the plugging constant, reducing the fouling formation rate.
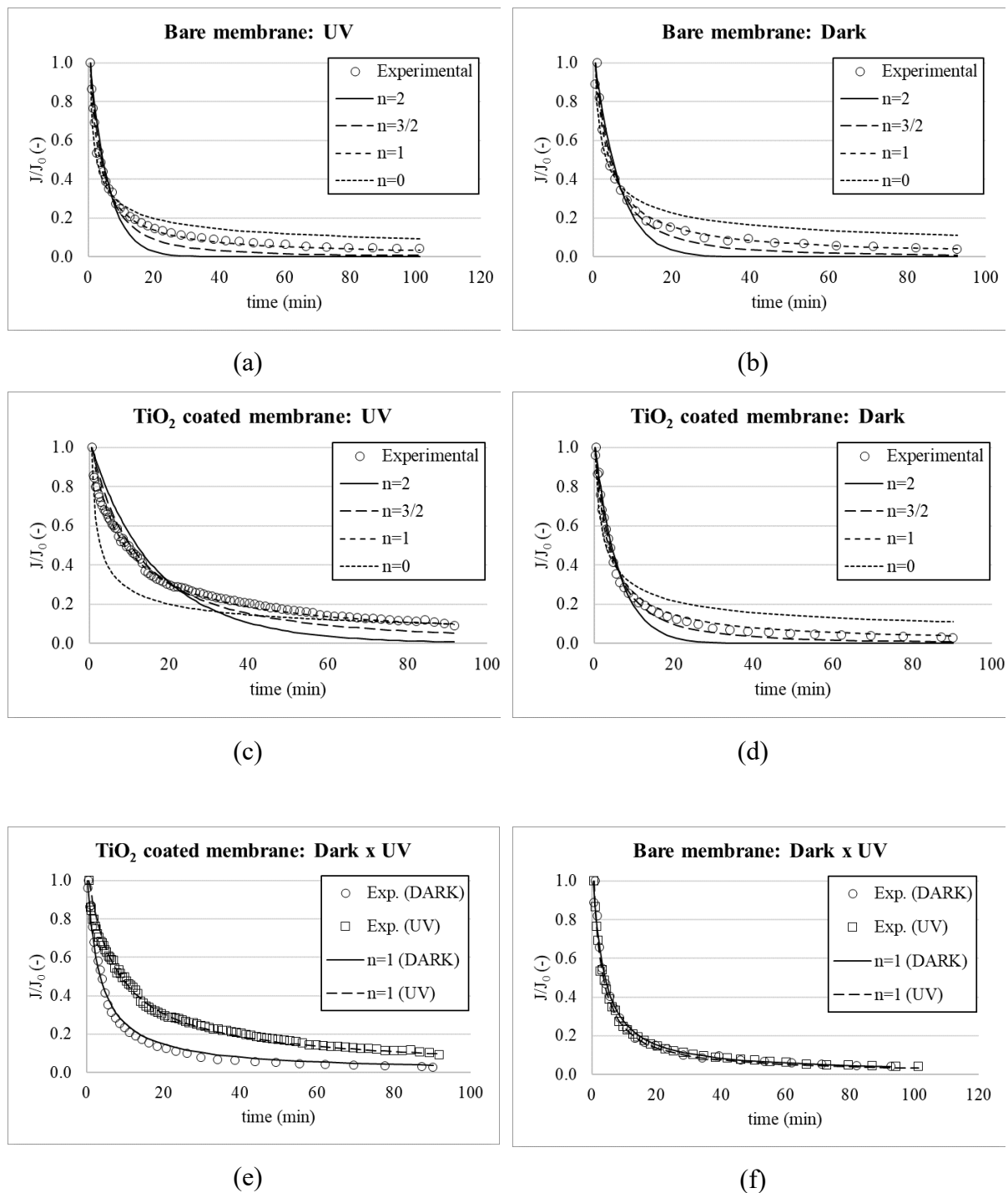
Figure 5.13 Fitting data to Hermia's model for experimental data of permeation of acetaminophen for (a) bare membrane in the dark, (b) 3x coated membrane in the dark, and (c) 3x TiO_2 coated membrane under UV; and (d) a comparison for coated membrane under UV for the fitting model using n=1.

These results demonstrated the excellent suitability of the suggested sol-gel dip-coating process to improve membrane filtration performance, using a simple process and enabling PMs to be produced without losing the original morphology of the membrane surface.

Finally, filtration of lubricating oil emulsions (50 – 250 ppm) resulted in up to 87% TOC removal at 1 bar. Membranes were not able to completely degrade fouling though. This result is attributed to the thick fouling layer on the membrane surface as well as fouling deposition inside the membrane pores. Thus, further research is necessary to produce a photocatalytic membrane with improved performance for oily wastewater.

5.5   REFERENCES

[1]   C. F. Couto, L.C. Lange, M.C. S. Amaral, A critical review on membrane separation processes applied to remove pharmaceutically active compounds from water and wastewater, J. Water Process Eng. 26 (2018) 156–175. https://doi.org/10.1016/j.jwpe.2018.10.010.

[2]   P.S. Goh, K.C. Wong, A.F. Ismail, Membrane technology: A versatile tool for saline wastewater treatment and resource recovery, Desalination. 521 (2022) 115377. https://doi.org/10.1016/j.desal.2021.115377.

[3]   E. Kavitha, E. Poonguzhali, D. Nanditha, A. Kapoor, G. Arthanareeswaran, S. Prabhakar, Current status and future prospects of membrane separation processes for value recovery from wastewater, Chemosphere. 291 (2022) 132690. https://doi.org/10.1016/j.chemosphere.2021.132690.

[4]   H.J. Tanudjaja, C.A. Hejase, V. V. Tarabara, A.G. Fane, J.W. Chew, Membrane-based separation for oily wastewater: A practical perspective, Water Res. 156 (2019) 347–365. https://doi.org/10.1016/j.watres.2019.03.021.

[5]   M.B. Asif, Z. Zhang, Ceramic membrane technology for water and wastewater treatment: A critical review of performance, full-scale applications, membrane fouling and prospects, Chem. Eng. J. 418 (2021) 129481. https://doi.org/10.1016/j.cej.2021.129481.

[6]   C. Li, W. Sun, Z. Lu, X. Ao, S. Li, Ceramic nanocomposite membranes and membrane fouling: A review, Water Res. 175 (2020) 115674. https://doi.org/10.1016/j.watres.2020.115674.

[7]   Q. Gu, T.C.A. Ng, Y. Bao, H.Y. Ng, S.C. Tan, J. Wang, Developing better ceramic membranes for water and wastewater Treatment: Where microstructure integrates with chemistry and functionalities, Chem. Eng. J. 428 (2021) 130456. https://doi.org/10.1016/j.cej.2021.130456.

[8]F. Sun, H.T. Ren, T.T. Li, S.Y. Huang, Y. Zhang, C.W. Lou, J.H. Lin, Bioinspired design of underwater superoleophobic Poly(N-isopropylacrylamide)/ polyacrylonitrile/TiO_2 nanofibrous membranes for highly efficient oil/water separation and photocatalysis, Environ. Res. 186 (2020) 109494. https://doi.org/10.1016/j.envres.2020.109494.

[9]X. Ma, Z. Yang, Z. Yao, H. Guo, Z. Xu, C.Y. Tang, Tuning roughness features of thin-film composite polyamide membranes for simultaneously enhanced permeability, selectivity and anti-fouling performance, J. Colloid Interface Sci. 540 (2019) 382–388. https://doi.org/10.1016/j.jcis.2019.01.033.

[10]G. Scaratti, A. De Noni Júnior, H.J. José, R. de Fatima Peralta Muniz Moreira, 1,4-Dioxane removal from water and membrane fouling elimination using CuO-coated ceramic membrane coupled with ozone, Environ. Sci. Pollut. Res. 27 (2020) 22144–22154. https://doi.org/10.1007/s11356-019-07497-6.

[11]   X. Pang, S. Xue, T. Zhou, Q. Xu, W. Lei, 2D/2D nanohybrid of Ti_3C_2 MXene/WO3 photocatalytic membranes for efficient water purification, Ceram. Int. 48 (2022) 3659–3668. https://doi.org/10.1016/j.ceramint.2021.10.147.

[12]   N. Rosman, W. Norharyati Wan Salleh, N. Aqilah Mohd Razali, S.Z. Nurain Ahmad, N. Hafiza Ismail, F. Aziz, Z. Harun, A. Fauzi Ismail, N. Yusof, Ibuprofen removal through photocatalytic filtration using antifouling PVDF- $ZnO/Ag_2CO_3/Ag_2O$ nanocomposite membrane, Mater. Today Proc. 42 (2019) 69–74. https://doi.org/10.1016/j.matpr.2020.09.476.

[13]   S. Mozia, Photocatalytic membrane reactors (PMRs) in water and wastewater treatment. A review, Sep. Purif. Technol. 73 (2010) 71–91. https://doi.org/10.1016/j.seppur.2010.03.021.

[14]   X. Wang, S. Li, P. Chen, F. Li, X. Hu, T. Hua, Photocatalytic and antifouling properties of TiO_2-based photocatalytic membranes, Mater. Today Chem. 23 (2022) 100650. https://doi.org/10.1016/j.mtchem.2021.100650.

[15]   N.P. Simonenko, V.A. Nikolaev, E.P. Simonenko, N.B. Generalova, V.G. Sevastyanov, N.T. Kuznetsov, Preparation of nanostructured titania thin films by sol–gel technology, Russ. J. Inorg. Chem. 61 (2016) 1505–1511. https://doi.org/10.1134/S0036023616120184.

[16]   I. Cacciotti, A. Bianco, G. Pezzotti, G. Gusmano, Synthesis, thermal behaviour and luminescence properties of rare earth-doped titania nanofibers, Chem. Eng. J. 166 (2011) 751–764. https://doi.org/https://doi.org/10.1016/j.cej.2010.07.008.

[17]   H. Zhang, J. Zhang, J. Luo, Y. Wan, A novel paradigm of photocatalytic cleaning for membrane fouling removal, J. Memb. Sci. 641 (2022) 119859. https://doi.org/10.1016/j.memsci.2021.119859.

[18]   S.A. Gokulakrishnan, G. Arthanareeswaran, Z. László, G. Veréb, S. Kertész, J. Kweon, Recent development of photocatalytic nanomaterials in mixed matrix membrane for emerging pollutants and fouling control, membrane cleaning process, Chemosphere. 281 (2021). https://doi.org/10.1016/j.chemosphere.2021.130891

[19]   C. Li, Z. Lu, X. Ao, W. Sun, X. Huang, Degradation kinetics and removal efficiencies of pharmaceuticals by photocatalytic ceramic membranes using ultraviolet light-emitting diodes, Chem. Eng. J. 427 (2022) 130828. https://doi.org/10.1016/j.cej.2021.130828

[20]   S. Huang, R.H.A. Ras, X. Tian, Antifouling membranes for oily wastewater treatment: Interplay between wetting and membrane fouling, Curr. Opin. Colloid Interface Sci. 36 (2018) 90–109. https://doi.org/10.1016/j.cocis.2018.02.002.

[21]   J. Xue, M. Xu, J. Gao, Y. Zong, M. Wang, S. Ma, Multifunctional porphyrinic Zr-MOF composite membrane for high-performance oil-in-water separation and organic dye adsorption/photocatalysis, Colloids Surfaces A Physicochem. Eng. Asp. 628 (2021) 127288. https://doi.org/10.1016/j.colsurfa.2021.127288.

[22] L.L. Coelho, M. Grao, M. Wilhelm, M. Ratova, P. Kelly, R.F.P.M. Moreira, Photocatalytic microfiltration membranes produced by magnetron sputtering with self-cleaning capabilities, Thin Solid Films. (2022).

[23]   S. Deepracha, L. Atfane, A. Ayral, M. Ogawa, Simple and efficient method for functionalizing photocatalytic ceramic membranes and assessment of its applicability for wastewater treatment in up-scalable membrane reactors, Sep. Purif. Technol. 262 (2021). https://doi.org/10.1016/j.seppur.2021.118307.

[24]   F.E. Bortot Coelho, D. Deemter, V.M. Candelario, V. Boffa, S. Malato, G. Magnacca, Development of a photocatalytic zirconia-titania ultrafiltration membrane with anti-fouling and self-cleaning properties, J. Environ. Chem. Eng. 9 (2021) 106671. https://doi.org/10.1016/j.jece.2021.106671.

[25]   S. Leong, A. Razmjou, K. Wang, K. Hapgood, X. Zhang, H. Wang, TiO_2 based photocatalytic membranes: A review, 472 (2014) 167–184. https://doi.org/http://dx.doi.org/10.1016/j.memsci.2014.08.016.

[26]   G. Žerjav, G. Scandura, C. Garlisi, G. Palmisano, A. Pintar, Sputtered vs. sol-gel TiO_2-doped films: Characterization and assessment of aqueous bisphenol A oxidation under UV and visible light radiation, Catal. Today. 357 (2020) 380–391. https://doi.org/10.1016/j.cattod.2019.09.027.

[27]   S. M. Simon, G. George, S. M S, P. V P, T. A. Jose, P. Vasudevan, A.C. Saritha, P.R. Biju, C. Joseph, N. V. Unnikrishnan, Recent advancements in multifunctional applications of sol-gel derived polymer incorporated TiO_2-ZrO_2 composite coatings: A comprehensive review, Appl. Surf. Sci. Adv. 6 (2021) 100173. https://doi.org/10.1016/j.apsadv.2021.100173.

[28]   X. Chen, Y. Hu, Z. Xie, H. Wang, Current Trends and Future Developments on (Bio)Membranes., in: Curr. Trends Futur. Dev. Membr., Elsevier Inc., 2018: pp. 71–96. https://doi.org/https://doi.org/10.1016/B978-0-12-813549-5.00003-7.

[29] L.L. Coelho, M. Di Luccio, D. Hotza, R. de Fátima Peralta Muniz Moreira, A.C. Moreira, C.P. Fernandes, K. Rezwan, M. Wilhelm, Tailoring asymmetric Al_2O_3 membranes by

combining tape casting and phase inversion, J. Memb. Sci. 623 (2021) 119056.
https://doi.org/10.1016/j.memsci.2021.119056.

[30]   R. S. Cardoso, S.M. de Amorim, G. Scaratti, C.D. Moura-Nickel, R.P.M. Moreira, G. Li Puma, R. de F.P.M. Moreira, Structural, optical and photocatalytic properties of erbium (Er^{3+}) and yttrium (Y^{3+}) doped TiO_2 thin films with remarkable self-cleaning super-hydrophilic properties, RSC Adv. 10 (2020) 17247–17254. https://doi.org/10.1039/d0ra02242j.

[31]   L.L. Coelho, G. Scaratti, A.M. Hissanaga, B.F. Oechsler, H.J. José, R. de F.P.M. Moreira, Modeling and fouling control in a hybrid membrane process using CuO-catalytic membrane coupled to ozone, J. Environ. Chem. Eng. 9 (2021). https://doi.org/https://doi.org/10.1016/j.jece.2021.106138.

[32]   J. Hermia, Blocking Filtration: Application to Non-Newtonian Fluids in Mathematical models and design methods in solid-liquid separation., 1982.

[33]   Y. Zhang, H. Tan, C. Wang, B. Li, H. Yang, H. Hou, C. Xiao, TiO_2-coated glass hollow fiber membranes: preparation and application for photocatalytic methylene blue removal, J. Eur. Ceram. Soc. 42 (2022) 2496–2504. https://doi.org/10.1016/j.jeurceramsoc.2021.12.075.

[34]N. Padoin, C. Soares, An explicit correlation for optimal TiO_2 film thickness in immobilized photocatalytic reaction systems, Chem. Eng. J. 310 (2017) 381–388. https://doi.org/10.1016/j.cej.2016.06.013.

[35]A. Azaïs, J. Mendret, E. Petit, S. Brosillon, Evidence of solute-solute interactions and cake enhanced concentration polarization during removal of pharmaceuticals from urban wastewater by nanofiltration, Water Res. 104 (2016) 156–167. https://doi.org/10.1016/j.watres.2016.08.014.

[36]   W. Zhang, L. Ding, J. Luo, M.Y. Jaffrin, B. Tang, Membrane fouling in photocatalytic membrane reactors (PMRs) for water and wastewater treatment: A critical review, Chem. Eng. J. 302 (2016) 446–458. https://doi.org/10.1016/j.cej.2016.05.071

[37]   M. Padaki, R.S. Murali, M.S. Abdullah, N. Misdan, A. Moslehyani, M.A. Kassim, N. Hilal, A.F. Ismail, Membrane technology enhancement in oil – water separation. A review, Des. 357 (2015) 197–207. https://doi.org/10.1016/j.desal.2014.11.023

6 CONCLUSIONS AND PERSPECTIVES

6.1   CONCLUSIONS

Photocatalytic ceramic membranes with antifouling capabilities were produced and well characterized. Phase inversion tape casting was successfully used to produce asymmetric microfiltration alumina membranes with high outstanding permeability and seems to be a promising alternative route to produce asymmetric ceramic membranes with one single sintering step. Higher alumina loadings led to higher flexural strength and lower flux as membrane morphology was modified. Surface pore sizes were not modified by changing the slurry composition though. Intrinsic permeability simulation from Micro-CT proved the presence of finger-like pores and higher flux resistances near the membrane surfaces due to the skin layers, and mainly on the bottom side. Co-casting strategy using graphite slurry allowed membranes to be produced without the dense bottom layers, although further adjustments to the slurry co-casting procedure need to be investigated. Membranes produced from a slurry containing 50/6.2 and 45/7 alumina/PES wt% are considered to have the best set of properties in terms of flexural strength and permeability. They were used to produce TiO_2 coated membranes by magnetron sputtering and sol-gel dip-coating, respectively.

Both TiO_2 coating techniques produced photocatalytic active anatase coatings. Membrane selectivity could be easily adjusted by tailoring coating thickness, and thus surface pore sizes when magnetron sputtering was used as the TiO_2 deposition method. The dense TiO_2 layers formed on the membrane surface led to a high flux decrease, though. In turn, the sol-gel dip-coating investigated in this work resulted in TiO_2 deposition on the membrane surface without forming a new separate layer nor modifying the membrane surface morphology. It can be beneficial to add photocatalytic features in membranes with suitable original pore sizes. Nevertheless, both membranes resulted in antifouling capabilities. While membranes coated with 400 nm TiO_2 layers with magnetron sputtering were able to remove up to 86% MB and fully recover its flux after UV irradiation overnight, membranes produced by sol-gel dip-coating improved membrane flux under UV irradiation. A 3.7-fold permeate volume enhancement was observed during the permeation of acetaminophen for 90 min for a TiO_2 sol-gel coated membrane compared to the bare membrane in dark conditions. Fouling modeling proved that the plugging constant was decreased while fouling mechanisms were not modified.

Produced photocatalytic membranes were not able to provide antifouling performance for oily wastewater filtration though. This fact results in fouling deposition inside the membrane pores and to the thick fouling layer on the membrane surface. In both cases, the photocatalyst is not able to be activated by the light source. Thus, further research is necessary to produce a photocatalytic membrane with improved performance for oily wastewater.

6.2 SUGGESTIONS FOR FUTURE WORK

- Produce membranes by phase inversion with smaller pore size, which could be obtained using alumina with smaller particle diameter and adjusting polymer, solvent, and additives concentrations in polymer solution;

- Optimize the co-casting strategy to produce membranes without the dense bottom layer;

- Investigate the functionalization of membranes with the techniques presented here using membranes with smaller pore sizes;

- Produce photocatalytic membranes for the treatment of oily effluents using coating layers of graphene oxide and graphitic carbon nitride with enhanced interlayer spacing;

- Further investigate the modeling of the antifouling mechanisms of photocatalytic membranes.